THE UNIVERSITY OF HULL

Computer simulations of doping, device structures and fabrication processes in semiconductors

being a Thesis submitted for the Degree of

Doctor of Philosophy (PhD)

in the University of Hull

by

Randeep Kumar Gug BSc

January 1999

Dedicated to Mum and Dad

Acknowledgments

I would like to start by thanking my parents, who taught me the value of education and hard work. To them I am forever in debt.

I would also like to thank my supervisor Winston Hagston, whose love for physics is inspirational. I thank him for his patience and guidance and feel that it was an honour to have been supervised by him.

Working in the Theory group at Hull, was a great pleasure, and I wish to thank all my friends within the group. In particular, I give a big thanks to Tom Stirner who has never been too busy for my questions.

Finally I would like to mention all the good friends which I have made during my stay in Hull, my time in Hull would have been much less enjoyable without them.

Contents

Chapter 1

Introduction

With the development of electronics from the large to the small, so the ideas and the intuitive guesses made in the former, classical physics case, have been replaced by the entirely different world of quantum mechanics. The progression from the continuous macroscopic to the discrete microscopic has revolutionized solid state physics, and with the development of new growth techniques such as molecular beam epitaxy (MBE) and metal organic vapour phase epitaxy (MOVPE) the possibility of atomic engineering has been realised. This precise form of 'growth to order' has greatly advanced the progression of materials such as quantum wells (QW), multi quantum wells (MQW) and superlattices (SL). Through the utilisation of the afore mentioned structures it has become commonplace to design new devices, which use the fundamental underlying physics in their operation.

1.1 Low Dimensional Structures (LDS)

In a bulk material, although quantum mechanics can be used to describe atomic properties, new and novel properties are found when the electrons are confined dimensionally. When the latter occurs in one dimension only (say, along the z direction) we still have a continuum of possibilities for motion in the x and y directions. A large collection of carriers confined in this way give rise to a two dimensional gas (2DEG). Similarly if we have confinement in two dimensions (y and z,say) with free motion only in the x direction then we have a one dimensional electron gas (1DEG), and so on to zero dimensions. This type of confinement is achieved by growing LDS using the above mentioned growth techniques. The associated technology permits the growth of semiconductor heterostructures monolayer, by monolayer. thus enabling precise structures to be grown.

In this thesis, we will be concerned with the 2DEG, i.e where the carrier is confined in one direction only. A structure which achieves this type of confinement is a QW, this being produced using one of the advanced growth techniques mentioned earlier. A series of QW's (i.e a multiquantum well, MQW, structure) can be produced by systematic growth of semiconductor layers (see Fig (1.1a)). Since each adjacent layer is composed of a different material having distinct band edges, we find the band profile shown in Fig (1.1b) could be formed, i.e a region where the band edges are lower in energy than in the neighbouring layers. The latter shows an abrupt change in the potential at the interface between material A and B, with the consequence that an electron (or hole) finds itself confined within the region of lower potential. In a semiconductor heterostructure such as GaAs/$\mathrm{Al}_x\mathrm{Ga}_{1-x}\mathrm{As}$, there is a difference in the depths of the QW's in the valence band and conduction band. The difference in the band gap is called the total offset $O_{tot} = E_g^B - E_g^A$. A fraction ξ of O_{tot} lies in the valence band (i.e the valence band offset O_{VB}), and the rest in the conduction band O_{CB}. Thus,

$$O_{VB} = \xi \times O_{tot} \qquad \text{and}$$

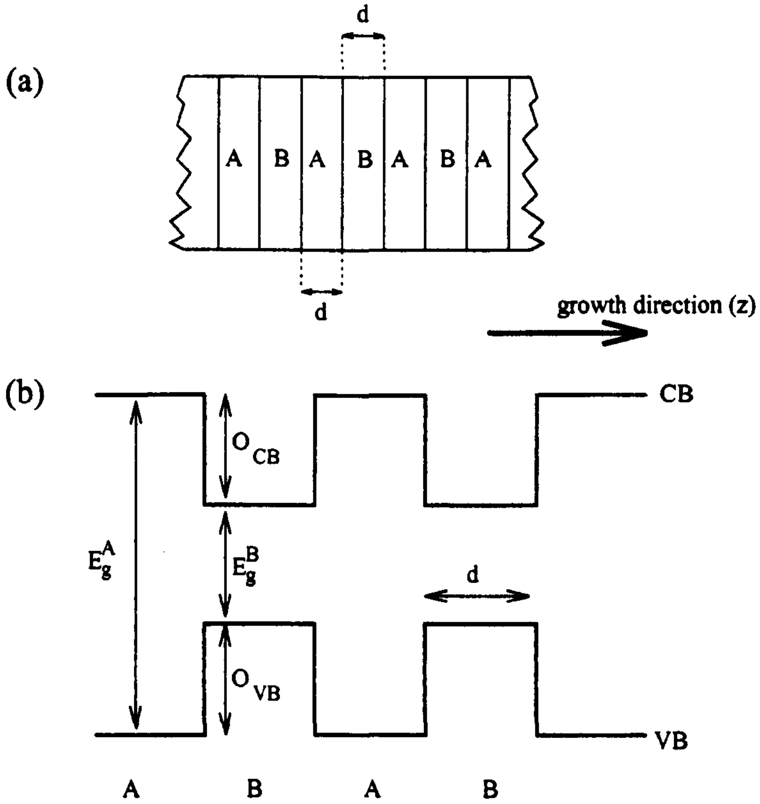

Figure 1.1: (a)Schematic diagram showing a typical sandwich structure, with layer thickness d∼nm;(b) band edge diagram for a typical type I sandwich structure.

$$O_{CB} = (1 - \xi) \times O_{tot}.$$

ξ is determined experimentally for each particular heterostructure. It's value is well known for certain structures, e.g CdTe/$Cd_{1-x}Mn_xTe$ [7] and GaAs/$Al_xGa_{1-x}As$ [8].

To confine a carrier in one dimension, it is not necessary to use a semiconductor heterostructure. Another possible way of confining a carrier is to use a doped semiconductor. Using such a doped structure it is possible to create a parabolic potential well from a region of ionized donors. This parabolic potential acts to confine the carrier in much the same way as the QW in semiconductor heterostructures.

If the well formed by either process for the electron and the hole are spatially above one another this is called a type I material; however if they are spatially separated then we have a type II material.

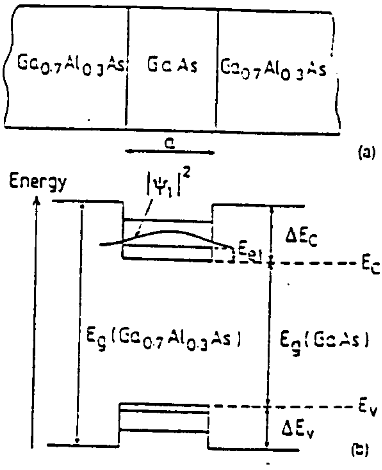

Figure 1.2: a)The growth sequence of GaAs and $Ga_{1-x}Al_xAs$ alloys forming a QW where here x = 30%. b) The band structure for the QW.

1.2 QW,MQW and SL's

Fig (1.2a) shows the growth sequence of a typical III-V heterostructure, so called because of the grouping of its constituent elements within the periodic table. The QW is formed by sandwiching a region of GaAs between barrier regions formed from GaAs $Ga_{1-x}Al_xAs$ [1], as shown in Fig (1.2b). Solution of the associated time independent Schrödinger equation yields the eigen energies and the one particle wavefunctions for the system. These wavefunctions (or to be more precise, envelope functions) consist of two spatially distinct parts. The first is the wavefunction for the particle in the QW (ψ_W), and the second is the wavefunction for the particle in the barrier (ψ_B).Application of the matching conditions for ψ_W and ψ_B and their derivatives across the interface enable the one particle Schrödinger equation to be solved [2]

The finite probability of finding the carrier in the barrier region is important with the penetration of the wavefunction into the barrier giving rise to the possibility of quantum mechanical tunneling. Fig (1.2b) shows a QW structure with discrete energy levels arising from the confinement of the carrier wavefunction. If the number of QW is increased, but with the barrier width being such that there is no overlap between the wavefunctions in adjacent wells we would have a MQW system. This system consists of a series of identical isolated QW's with all the energy levels of the different QW's being degenerate, see Fig (1.3a).

If the barriers widths are reduced so that the wavefunctions of neighbouring wells overlap then the degeneracy is removed and minibands are formed. This is known as a SL with the wavefunctions of the resulting miniband extending over the whole structure [3] see Fig (1.3b).

---

[1] where x is the concentration of Al

[2] In terms of effective mass theory, the effective mass of the particle in the barrier is different from that of the particle in the well. A popular form of the interface matching condition for the derivative of the wavefunction is the 'Bastard' condition [1].

$$\frac{1}{m_1}\frac{d\psi_1}{dz}\bigg|_{z=0-} = \frac{1}{m_2}\frac{d\psi_2}{dz}\bigg|_{z=0+}$$

where m_1 and ψ_1 are the effective mass and the wavefunction in the barrier, and m_2 and ψ_2 are the effective mass and the wavefunction in the well.

[3] This is very similar to the way in which allowed and forbidden bands are created in bulk material and is described well by energy band theory.

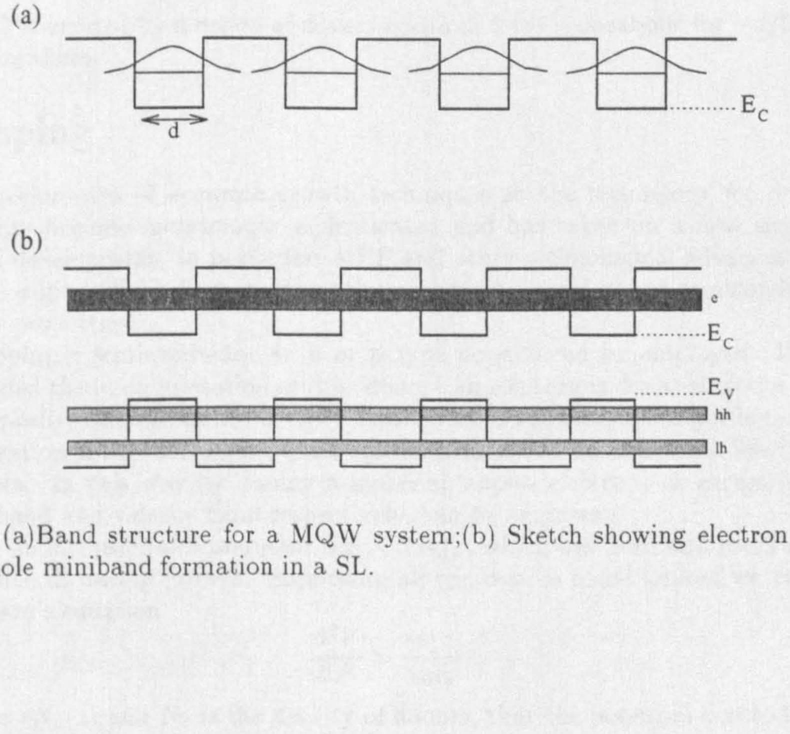

Figure 1.3: (a)Band structure for a MQW system;(b) Sketch showing electron, light hole and heavy hole miniband formation in a SL.

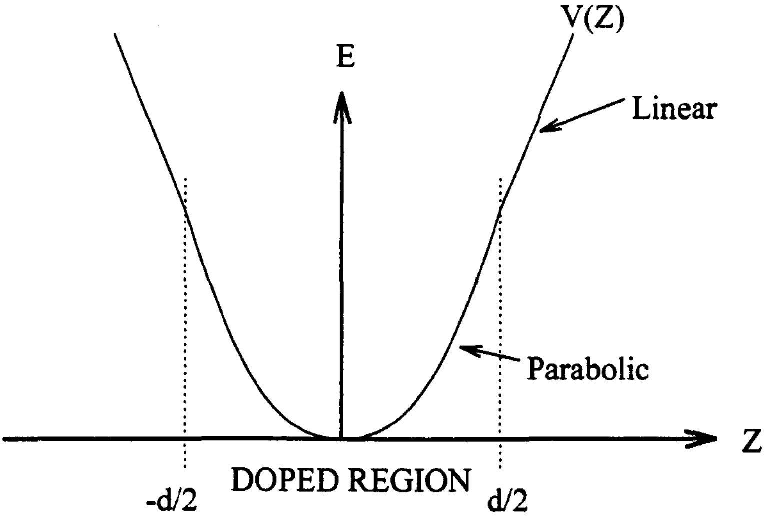

Figure 1.4: QW created by a region of donors width d; $V(z)$ is parabolic for $-d/2 \leq z \leq d/2$ and linear elsewhere.

1.3 Doping

With the development of accurate growth techniques so the technology for doping semiconductors has become increasingly sophisticated and has taken on a new significance in research and development. In particular MBE and other technological advances have made it possible to dope individual monolayers thus producing novel doped semiconductors with exciting new properties.

When doping a semiconductor an n or p type dopant can be employed. If an n-type dopant is added then , on ionisation of this 'donor', an electron is donated to the conduction band and a positive charge centre is left . Conversely if the semiconductor is p-type doped then on ionisation of the 'acceptors', holes are donated to the valence band, leaving negative charge centers. In this way by doping a material, excess electrons or excess holes in the conduction band and valence band respectively, can be engineered.

Consider an intrinsic semiconductor (i.e. CdTe), , which has been uniformly n-doped, in a slab of width d, during growth. Supposing all the donors to be ionised we can show by solving Poisson's equation

$$\frac{\partial^2 V}{\partial z^2} = \frac{e\rho(z)}{\epsilon_0 \epsilon_r}$$

where $\rho(z) = eN_d(z)$ and N_d is the density of donors, that the potential due to the positive charge associated with the donors is parabolic over the doped region and linear outside this region, as in Fig (1.4).

Thus by doping a semiconductor we can create QW type regions. However if electrons are actually trapped in this region, then their presence will modify this potential (self-consistent effects). As a result of controlled MBE growth we can if so desired, dope a single monolayer only. This is known as delta doping (in reality of course, diffusion of the dopants will occur, nonetheless, as a first approximation, if diffusion is limited in extent, this can be ignored).

By utilising MBE, new types of structures can be grown in a given semiconductor. Thus by either delta doping or employing a constant dopant density in a given region of a semiconductor; a "new periodicity" can be introduced into the structure. In particular if a given semiconductor is doped first with acceptors, and then with donors in repeated planes, layers of negative (n) and positive (p) space-charge in the conductor, often separated by an intrinsic (i) or undoped layer can be formed [4]. These are called n-i-p-i superlattices.

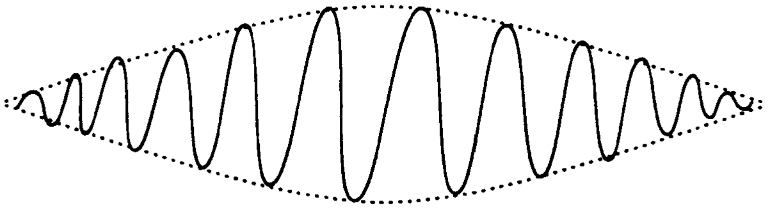

Figure 1.5: Solution to the one particle Schrödinger equation, where the solid line is the true solution $\Psi = U(\underline{r}, m)\chi(\underline{r}, m)$ and the dotted line the envelope function which appears in the envelope function approximation $\Psi = \chi(\underline{r}, m^*)$.

1.4 One-particle energy and wavefunction calculations

In this section we are concerned with describing the method used to calculate one-particle wavefunctions and energy levels. Prior to describing the "shooting" technique which is employed for this purpose, we outline an approximation called the envelope function approximation.

1.4.1 Envelope function approximation

Using the time independent Schrödinger equation

$$H\psi = E\psi \tag{1.1}$$

we can solve for the one particle eigen energies and wavefunctions in the QW. The wavefunction consists of both a rapidly oscillating Bloch function U and a slowly varying envelope function χ and is written as

$$\Psi = U(\underline{r}, m)\chi(\underline{r}, m)$$

In the envelope function approximation [1] we neglect the rapidly varying Bloch function component of the wavefunction [1, 2, 3] and assume that the wavefunction consists of only a slowly varying envelope function,see Fig (1.5). Elimination of U from the description leads to an expression for the Hamiltonian in which the rapidly varying one-electron potential is replaced by a slowly varying potential $V(z)$ and the mass m of the particle is replaced by an effective mass m^* specific to the appropriate semiconductor. We now find that

$$\Psi = \chi(\underline{r}, m^*)$$

Where Ψ now satisfies the effective Schrödinger equation given in equation (1.2) below.

1.4.2 Shooting technique

The shooting technique is employed to calculate the eigenstates and energies by solving the time independent Schrödinger equation. The Hamiltonian is given by

$$H = -\frac{\hbar^2}{2m^*}\frac{d^2}{dz^2} + V(z)$$

and the Schrödinger equation can be written as

$$-\frac{\hbar^2}{2m^*}\frac{d^2\psi}{dz^2} + [V(z) - E]\,\psi = 0 \quad . \tag{1.2}$$

The solution to the above equation must satisfy the boundary conditions $\psi(z) \Rightarrow 0$ as $z \Rightarrow \pm\infty$, we solve the equation numerically using a finite difference method. Thus the second order derivative of the wavefunction $\frac{d^2\psi}{dz^2}$ is replaced by a finite difference i.e.

$$\frac{d^2\psi}{dz^2} \approx \frac{f(z+2\delta z)+f(z-2\delta z)-f(z)}{(2\delta z)^2} \tag{1.3}$$

Using equation (1.3) we can rewrite the Schrödinger equation as[4]

$$\psi(z+\delta z) = \left(2(\delta z)^2\frac{m^*}{\hbar^2}(V(z)-E)+2\right)\psi(z)-\psi(z-\delta z) \quad . \tag{1.4}$$

This implies that if the wavefunction is known at z and $z-\delta z$ then for any arbitrary energy E the value at $z+\delta z$ can be found. Thus using two known values of the wavefunction a third can be predicted. Using this new point $\psi(z+\delta z)$, together with $\psi(z)$ and by making the transformation $z+\delta z \Rightarrow z$, a fourth point $\psi(z+2\delta z)$ can be calculated and so on. Hence the whole wavefunction can be deduced for any particular energy. The solution, which represents the stationary state of interest, has a wavefunction that obeys the standard boundary conditions i.e. $\psi \Rightarrow 0$ as $z \Rightarrow \pm\infty$.

The initial two values of the wavefunction needed to start the iteration process can be determined, by either symmetry arguments (if $V(z)$ is symmetric) or by physical arguments(if V(z) is arbitrary). The former determination of $\psi(z-\delta z)$ and $\psi(z)$ utilises the fact that the eigenstates must have either even or odd parity. If, for example we chose the latter, then its wavefunction must have a node at the center of the well $\psi(0)=0$. Hence an arbitrarily small decrease along the z axis yields $\psi(z-\delta z)$; its magnitude is irrelevant since eigenvalues of a linear differential equation, such as the Schrödinger equation are not affected by a scaling factor. If the state has even parity then $\psi(-\delta z)=\psi(+\delta z)$ and substitution of this condition into equation (1.4) gives an equation for $\psi(z\pm\delta z)$ in terms of $\psi(0)$. The latter can be assigned an arbitrary value for the reason described earlier. Hence with $\psi(0)$ and $\psi(z\pm\delta z)$ known the iteration process can begin.

For an arbitrary value of the potential V(z) the determination of $\psi(z-\delta z)$ and $\psi(z)$ invokes physical arguments. In effect ψ is assigned a value of zero at some distance L into the barrier region and a value of unity in the second step. Thus

$$\psi(z=-L)=0 \tag{1.5}$$

$$\psi(z=-L+\delta z)=1 \tag{1.6}$$

The condition in equation (1.5) arises from the known exponential decay of $\psi(z)$ in the barrier region.

In summary, starting with a known potential $V(z)$, the initial conditions of equations (1.5) and (1.6) and the iterative loop of equation (1.4), the value of the wavefunction at $z=+\infty$, ψ_∞, say, can be calculated for a chosen energy E, i.e. ψ_∞ is a function of energy E. Hence solutions are sought to the equation

$$\psi_\infty(E)=0$$

---

[4] Since δz is arbitrary the transformation $2\delta z \Rightarrow \delta z$ can be made.

1.5 Exciton binding energy calculations

This section outlines briefly the variational approach used to calculate the exciton binding energy E_b as developed in [5, 6].

This approach involves solving the time independent Schrödinger equation given in equation (1.1), for the Hamiltonian $\mathcal{H}$

$$\mathcal{H} = \mathcal{H}_e + \mathcal{H}_h + \mathcal{H}_\perp + \mathcal{H}_c$$

where:

$\mathcal{H}_e$	is the hamiltonian describing the electron;
$\mathcal{H}_h$	is the hamiltonian describing the hole;
$\mathcal{H}_\perp$	describes the kinetic energy of the relative motion of the electron and hole;
$\mathcal{H}_c$	is the hamiltonian describing the coulombic interaction between the elctron and the hole.

Using the framework of the envelope function approximation a trial wavefunction was employed (Ψ). The trial wavefunction consists of a product of the one particle electron envelope function (ψ_e), the one particle hole envelope function (ψ_h) together with the envelop function describing the relative motion of the electron and hole (ψ_{e-h}), i.e

$$\Psi = \psi_e \psi_h \psi_{e-h}. \tag{1.7}$$

The ψ_e and ψ_h (which are solutions to $\mathcal{H}_e$ and $\mathcal{H}_h$ respectively), and the corresponding energies are obtained using the shooting technique discussed earlier.

For a 1S excitonic orbit ψ_{e-h} is chosen to have the functional form

$$\psi_{e-h} = \exp\left(\frac{-r'}{\lambda}\right) \quad ,$$

where

$$r'^2 = (x_e - x_h)^2 + (y_e - y_h)^2 + (1 - \beta^2)(z_e - z_h)^2.$$

with λ and β variational parameters.

The parameter β determines the dimensionality of the exciton orbit, i.e the orbit of the exciton can be assumed to spherical (3-D), when $\beta = 0$, or planar (2-D), when $\beta = 1$, or any orbit of a dimensionality which is between these extremes. Therefore β has the range $0 \leq \beta \leq 1$.

The total energy of the system is given by:

$$E = E_e + E_h - E_b \quad ,$$

where E_e and E_h are the electron and hole one particle energies, i.e

$$E_e = \frac{< \psi_e | \mathcal{H}_e | \psi_e >}{< \psi_e | \psi_e >}$$

and correspondingly for the hole. The exciton binding energy E_b is given by

$$E_b = \frac{\hbar^2}{2\mu} \frac{\int |\psi_e|^2 |\psi_h|^2 |\frac{\partial \psi_{e-h}}{\partial z_e}|^2 \ d\tau}{\int |\psi_e|^2 |\psi_h|^2 |\psi_{e-h}|^2 \ d\tau} - \frac{\int |\psi_e|^2 |\psi_h|^2 (\psi_{e-h} (\mathcal{H}_\perp + \mathcal{H}_c) \psi_{e-h}) \ d\tau}{\int |\psi_e|^2 |\psi_h|^2 |\psi_{e-h}|^2 \ d\tau} \tag{1.8}$$

The variational method described involves minimising the total energy E by maximising the exciton binding energy E_b (given in equation (1.8)).

1.6 Radiative Transition Probabilities

Of particular interest in spectroscopic measurements are the values of the radiative transition probabilities (R), which determine the emission and absorption intensities. It can be shown that R is proportional to

$$R \propto | < \Psi | \Psi > |^2$$

where Ψ is the exciton wavefunction.

Bibliography

[1] G.Bastard,Wave Mechanics Applied to Semiconductor Hetrostructures (Halsted Press,New York,1988).

[2] N.W.Ashcroft and N.D.Mermin,Solid State Physics,(CBS Publishing,Philadelphia,1976).

[3] C.Kittel,Introduction to Solid State Physics,(John Wiley & Sons Inc. New Yory,1956).

[4] E.A.Johnson,Advanced Low-Dimensional Structures, to be published.

[5] C.P. Hilton, W.E. Hagston, J.E. Nicholls, J.Phys.A:Math Gen. **25**,2395 (1992).

[6] P. Hilton, J. Goodwin, P. Harrison, and W.E. Hagston J.Phys.A:Math Gen. **25**,5365 (1992).

[7] S.R. Jackson, J.E. Nicholls, W.E. Hagston, T.J. Gregory, P. Harrison, B. Lunn and D.E. Ashenford. Superlatt. and Microstruct. **12**,447 (1992).

[8] T. Hiroshima and K. Nishi. J.Appl.Phys. **62**,3360 (1987).

Chapter 2

Tuning of surface electric field via a quantum well-like structure for the purpose of controlling catalytic activity.

2.1 Introduction

There has been much interest devoted to the study of engineering semiconductor heterostructures to produce novel devices. [1, 2] The method of engineering varies greatly, ranging from the doping [3] of these structures, through to the utilisation of strain produced in their growth by sophisticated growth techniques such as molecular beam epitaxy (MBE), or metal-organic chemical vapour deposition (MOCVD). [4] In the present chapter, some of the structures that are modelled have sharply defined interfaces, similar to the structures grown by the methods of MBE and MOCVD. However as shown later, it is not necessary, for the applications we will be concerned with, to have such well defined interfaces. Instead any technique which introduces some form of potential well (of what ever shape), which can confine and separate the charge carriers from the ionized donors can be used. This means that one need not employ commercially expensive growth techniques to obtain the desired effects, namely that of large surface fields.

The latter can be very useful and lead to novel applications, one such being the use of a semiconductor heterostructure to control a catalytic reaction taking place on its surface. The rate of a chemical reaction is an important variable, which it can be advantageous to control. One method of achieving this is to use a catalyst. The latter is a substance which increases the rate of the reaction, without itself undergoing any permanent change. Given that the catalytic activity of metals for example, [5, 6, 7], can be associated with both electronic and geometric factors, it is clear that these properties can be strongly influenced by the electronic structure of the surface and near surface regions of the support on which the catalyst is placed. Electro-positive or electro-negative promoters, strong metal-support interaction (SMSI) and the use of alloys to create surface ensembles, are all methods which are employed in attempts to influence the electronic state of the catalyst sites. None of the approaches mentioned have been able to demonstrate a clear link between catalytic activity and the electronic structure of active sites. Possible reasons for this include comparisons involving catalysts which differ very considerably in their electronic structure or catalysts that have been inherently inhomogeneous[1]. In this chapter we illustrate how doping of

---

[1] SMSI catalysts or alloys subject to surface segregation.

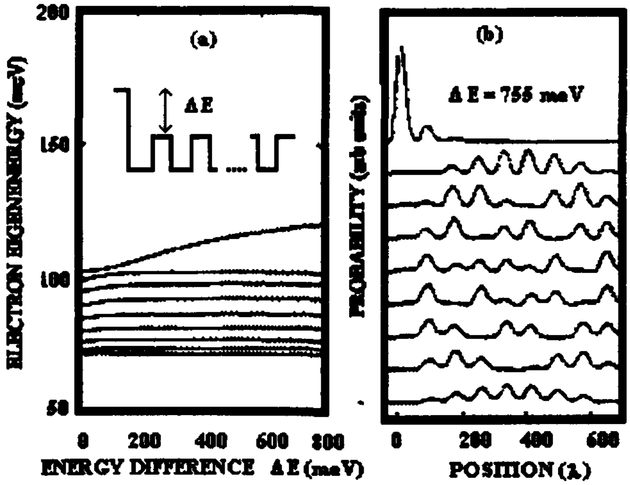

Figure 2.1: (a)potential profile of a nine-well superlattice,where the barrier width and the well widths are 40Å. (b) Square electron envelope function for $\Delta E = 755$meV,shown in order of eigen energy. The origin of the horizontal axis is at the left corner of the left most well.

a heterostructure, such as CdTe/$Cd_{1-x}Mn_xTe$, can lead to severe band-bending at the surface which gives rise to large internal electric fields. Since the surface electric field can be precisely controlled, by varying certain parameters associated with the quantum well (QW) structure lying beneath the surface, one could then influence, in a controlled manner, either the electronic structure of the catalyst or the adatom mobility at the surface, and hence the rate of the chemical reaction.

One method of achieving a high surface electric field would be to attempt to localise an electronic state at the surface of the heterostructure. Such localised surface states are called Tamm states [8, 9, 10, 11], and give rise to many novel effects [12, 13]. They can be engineered, readily, for example, in superlattices where the localised state lies at the top of the associated miniband (see Fig (2.1)) [14, 8]. As ΔE increases the highest energy state begins to 'peel off' from the miniband and simultaneously its wavefunction starts to localise at the interface. However the other wavefunctions stay delocalised and the width of the miniband remains essentially constant. Unfortunately our calculations show that the localisation of the wavefunction at the surface is very sensitive to the degree of perfection of the potential profile, and disperses rapidly away from the surface as the disorder and/or interface roughness increases. Consequently, although it is possible in principle to produce large fields by localizing an electronic state at the surface, in reality, this would be difficult to achieve in a commercially viable way. A much simpler, and more reliable way, is to grow a single QW close to it [15].

Fig. (2.2) is a schematic energy level diagram showing how localised electrons at the surface of the heterostructure can create a surface electric field. It shows a single QW close to a terminating surface barrier (having an associated work function) in which the surface to QW distance is called the cap layer [15]. There is a highly doped region about 20 Å wide (placed at various points in the structure) containing a donor dopant density, chosen for the purpose of illustration, to be approximately 4×10^{18} impurities/cm^3. The basic idea is that, in general, the donors become ionised, releasing electrons which are then confined within the QW. Again, for the purpose of illustration, it is assumed that each donor releases 1 electron to the system. Thus a region of ionised donors is created with the electrons from these same donors being confined in the QW. Both features change the potential profile of

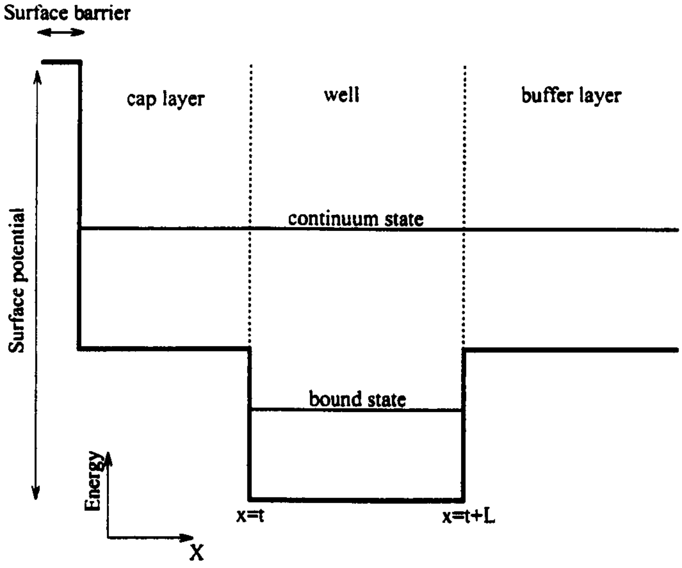

Figure 2.2: Band diagram of a single quantum well of depth V with a thick buffer layer, a well width L, a capping barrier layer of finite size (cap width t), the donors placed at Γ_d and a high potential at the surface at x=0.

the system, giving rise to a new profile.

The contributions of the ionised donors and the confined electrons to the net potential can be determined by solving Poisson's equation, i.e. in order to calculate the heterostructure potential we must superpose onto the original square QW potential the potential due to the ionised donors and the Hartree and exchange potentials due to the electrons (note, following 'tradition' in MBE growth we have considered a 'rectangular' quantum well. However, since we solve the Schrödinger equation numerically , the problem could just as readily be dealt with as if the 'well' was not rectangular. Equally, the essential results described below would be little affected by such a 'non-rectangular' well, since the latter is used mainly as a 'container' for the electrons, thus permitting the positive charge from the ionised donors to be separated in real space from the negative charge of the 'confined' electrons). To evaluate the Hartree potential for the electrons, we must find a self-consistent solution to both Poisson's equation and the one-particle Schrödinger equation [10]. The former equation is given by

$$\frac{\partial^2 \phi}{\partial x^2} = \frac{\rho}{\epsilon_0 \epsilon_r} \quad , \tag{2.1}$$

and can be used to find the resulting potential from both the constantly doped donor region and for the electrons. In the former case the density ρ is given by the charge density of the dopant distribution, whereas in the latter ρ is the probability density of the electrons. Thus for N electrons we would have to solve the following modified form of Poisson's equation

$$\frac{\partial^2 \phi}{\partial x^2} = \frac{eN|\psi|^2}{\epsilon_0 \epsilon_r} \quad , \tag{2.2}$$

self-consistently with the Schrödinger equation. (This follows from the assumption that the in-plane QW structure is 'flat', and hence that the in-plane motion of a given miniband structure can be represented by a plane wave with varying wave vector for the different electrons. Clearly, if there is 'roughness' along the 'QW plane', the calculations would become slightly more complicated, but the essential physics would remain unchanged.) Once the new potential profile has been calculated in this manner, the electric field, which is the gradient of the potential, can be found at any point.

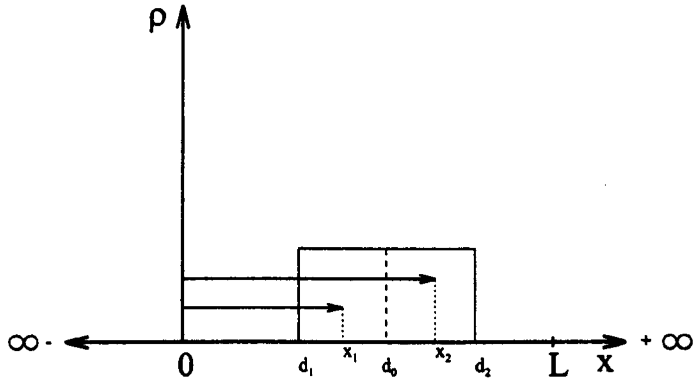

Figure 2.3: A diagram to illustrate the method of integration across the donor region,for a system of length L.

2.2 Theory

As described above, in order to obtain the potential and thus the electric field, the Poisson and Schrödinger equations must be solved self-consistently. For the constantly doped (ionised) donor region, the solution of the Poisson equation could be calculated analytically, as follows. Suppose ϕ is the resulting potential and ρ is the charge density. Given that the potential must have a turning point, the boundary conditions are given by:

$$\frac{\partial \phi}{\partial x} = 0 \qquad \text{at} \quad x = d_0 \qquad \text{with } d_0 \text{ to be determined}$$

and

$$\phi = 0 \qquad \text{at} \quad x = 0 \quad \text{or} \quad x = L \qquad \text{(this simply defines the zero of potential),}$$

Also the potential ϕ and its derivatives are continuous across the boundaries of the donor region at d_1 and d_2 (see Fig (2.3).

Starting from Poisson's equation we have (for the region between $d_1$and d_2)

$$\frac{\partial^2 \phi}{\partial x^2} = \frac{\rho}{\epsilon_0 \epsilon_r} = C \quad . \tag{2.3}$$

Integrating from x_1 to d_0 we get

$$\int_{x_1}^{d_0} \frac{\partial^2 \phi}{\partial x^2} = C \int_{x_1}^{d_0} dx$$

$$\left(\frac{\partial \phi}{\partial x}\right)_{d_0} - \left(\frac{\partial \phi}{\partial x}\right)_{x_1} = C(d_0 - x_1) \quad ,$$

i.e.

$$\left(\frac{\partial \phi}{\partial x}\right)_{x_1} = C(x_1 - d_0) \quad . \tag{2.4}$$

If we integrate equation (2.4) from d_1 to $x_1^{'}$ (where $x_1^{'}$ lies between d_1 and d_0) we have

$$\phi(x_1^{'}) - \phi(d_1) = \frac{C}{2}\left[(x_1^{'} - d_0)^2 - (d_1 - d_0)^2\right] \quad ,$$

i.e.

$$\phi(x_1^{'}) = \frac{C}{2}\left[(x_1^{'} - d_0)^2 - (d_1 - d_0)^2\right] + \phi(d_1) \tag{2.5}$$

$$\text{therefore} \qquad \phi(d_0) = -\frac{C}{2}(d_1 - d_0)^2 + \phi(d_1) \quad . \tag{2.6}$$

If we now integrate Poisson's equation from d_0 to x_2 (where x_2 lies between d_0 and d_2) we get:

$$\left(\frac{\partial\phi}{\partial x}\right)_{x_2} = C(x_2 - d_0) \tag{2.7}$$

and integrating equation (2.7) from x_2' to d_2 we get

$$\phi(x_2') = \frac{C}{2}\left[(x_2' - d_0)^2 - (d_2 - d_0)^2\right] + \phi(d_2) \tag{2.8}$$

$$\text{therefore} \qquad \phi(d_0) = -\frac{C}{2}(d_2 - d_0)^2 + \phi(d_2) \quad . \tag{2.9}$$

Outside the region d_1 to d_2 Poisson's equation reads

$$\frac{\partial^2\phi}{\partial x^2} = 0 \quad ,$$

Integrating over the region $0 \leq x \leq d_1$ gives

$$\frac{\partial\phi}{\partial x} = C_1$$

$$\text{from which we obtain} \qquad \phi = C_1 x + C_2 \quad .$$

Since at $x = 0$ $\phi = 0$ then

$$C_2 = 0 \quad ,$$

$$\text{therefore} \qquad \phi = C_1 x$$

From equation (2.4) we know that at $x = d_1$

$$\frac{\partial\phi}{\partial x} = C(d_1 - d_0) \quad ,$$

The equality of the derivative across boundary at d_1 gives therefore

$$C_1 = C(d_1 - d_0) \quad .$$

Similarly integrating for $d_2 \leq x \leq L$ we obtain

$$\phi = C_1' x + C_2' \quad .$$

Now for $d_2 \leq x \leq L$ we know that at $x = L$ $\phi = 0$, consequently

$$C_2' = -C_1' L$$

$$\text{thus giving} \qquad \phi = C_1'(x - L) \quad .$$

Similarly from equation (2.7), we know that at $x = d_2$

$$\frac{\partial\phi}{\partial x} = C(d_2 - d_0)$$

The equality of the derivative across boundary at d_2 gives

$$C_1' = C(d_2 - d_0)$$

Thus for $0 \leq x \leq d_1$

$$\phi = C(d_1 - d_0)x \quad , \tag{2.10}$$

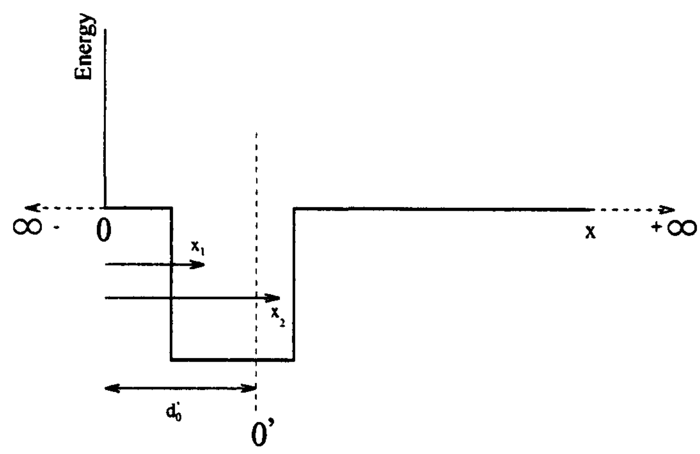

Figure 2.4: A diagram to illustrate the method of integration for the electrons.

and for $d_2 \leq x \leq L$

$$\phi = C(d_2 - d_0)(x - L) \quad . \tag{2.11}$$

Since ϕ is continuous across d_0 we can equate equation (2.9) and equation (2.6) to obtain (via equations 2.10 and 2.11)

$$d_0 = d_2 - \frac{(d_2^2 - d_1^2)}{2L} \quad . \tag{2.12}$$

Thus for $d_1 \leq x \leq d_0$

$$\phi(x) = \frac{C}{2}\left[(x - d_0)^2 - (d_1 - d_0)^2\right] + C(d_1 - d_0)d_1 \quad , \tag{2.13}$$

and for $d_0 \leq x \leq d_2$

$$\phi(x) = \frac{C}{2}\left[(x - d_0)^2 - (d_2 - d_0)^2\right] + C(d_2 - d_0)(d_2 - L) \quad , \tag{2.14}$$

where d_0 is given by equation (2.12).

Now for a varying charge density, in which the charge carriers are N electrons all described by a given wavefunction Ψ, the same technique as for the constant charge region is employed, when calculating the Hartree potential. The difference is that instead of a constant charge density ρ, the probability charge distribution $e|\Psi|^2$ is used. Thus in this case $\rho = eN|\Psi|^2$ (see equation (2.3)). To obtain the potential from Poisson's equation, involves evaluating an indeterminate integral, hence an analytical solution is not possible in this situation. Consequently the Poisson and Schrödinger equations were solved self consistently using the technique described below: Placing

$$\frac{Ne}{\epsilon_0 \epsilon_r} = C \quad ,$$

and noting the boundary conditions (see Fig (2.4):

$$\frac{\partial \phi}{\partial x} = 0 \quad \text{at} \quad x = d_0'$$

$$\phi = 0 \quad \text{at} \quad x = -\infty \quad \text{and} \quad x = +\infty \quad ,$$

gives, on integrating Poisson's equation from x_1 to d_0'

$$-\left(\frac{\partial \phi}{\partial x}\right)_{x_1} = C\int_{x_1}^{d_0'} |\Psi|^2 dx = g(x_1, d_0') \qquad \text{(say)} \quad . \tag{2.15}$$

Similarly integrating equation (2.15) from $-\infty$ to x_1' gives

$$\phi(x_1') = -\int_{-\infty}^{x_1'} g(x_1, d_0')dx_1 \quad . \tag{2.16}$$

$$\text{therefore} \quad \phi(d_0') = -\int_{-\infty}^{d_0'} g(x_1, d_0')dx_1 \quad . \tag{2.17}$$

On integrating Poisson's equation from d_0' to x_2 we obtain, in an obvious notation,

$$\left(\frac{\partial\phi}{\partial x}\right)_{x_2} = f(x_2, d_0') \quad \text{say} \quad , \tag{2.18}$$

whilst integrating equation (2.18) from x_2' to ∞ gives

$$\phi(x_2') = -\int_{x_2'}^{\infty} f(x_2, d_0')dx_2 \quad . \tag{2.19}$$

$$\text{therefore} \quad \phi(d_0') = -\int_{d_0'}^{\infty} f(x_2, d_0')dx_2 \quad . \tag{2.20}$$

Hence from equation (2.17) and (2.20) we obtain the identity

$$\int_{-\infty}^{d_0'} g(x_1, d_0')dx_1 = \int_{d_0'}^{\infty} f(x_2, d_0')dx_2 \quad . \tag{2.21}$$

Equation (2.21) enables us to determine, numerically the value of d_0'.

As well as the Hartree potential due to the confined electrons, there is also an exchange correlation potential $V_{XC}(x)$. This can be calculated using the local density approximation of the density functional formalism [16]. This yields a contribution of

$$V_{XC}(x) \approx V_X(x) \approx \frac{0.916e^2}{2\epsilon}\left(\frac{3n(x)}{4\pi}\right)^{\frac{1}{3}}$$

where $n(x)$ is the probability charge distribution $e|\Psi|^2$ multiplied by the number of charge carriers N.

The approximation holds only when the density of carriers is high. It breaks down at low densities. Consequently it can be incorporated into calculations only when the density of carriers is sufficiently high (typically $1 \times 10^{18}/\text{cm}^3$).

To solve the problem self-consistently requires employing a technique in which the difference between consecutive solutions is small. If the difference is large then the solutions will not converge. This means that, for calculational purposes the density of donors must be added incrementally, and the system solved self-consistently each time until the full donor density was attained. Fig (2.5) shows a flow chart showing all the computational steps in obtaining the self-consistent solution.

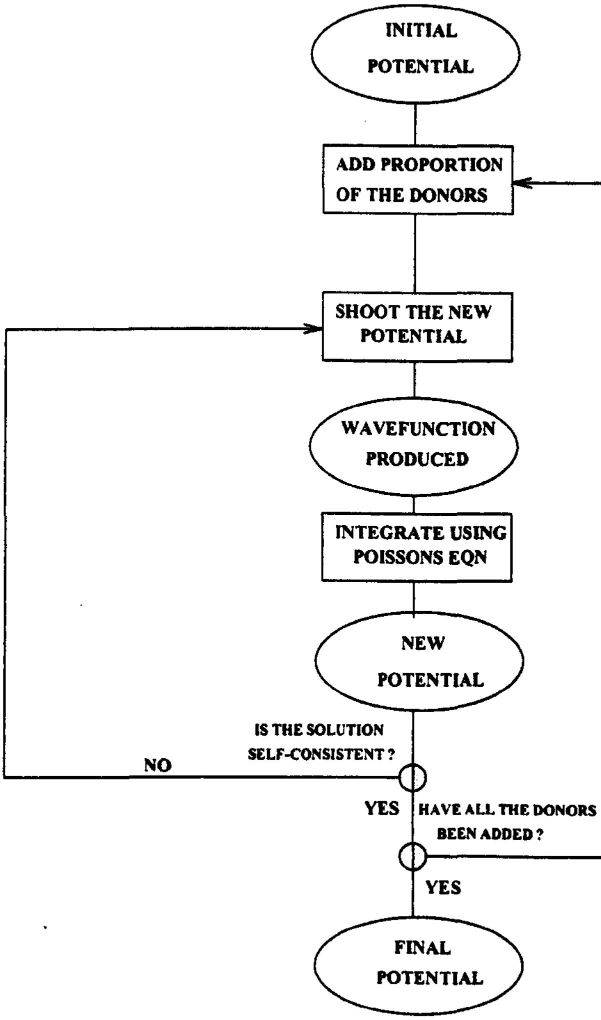

Figure 2.5: A flow chart showing the computational steps in obtaining the self-consistent solution.

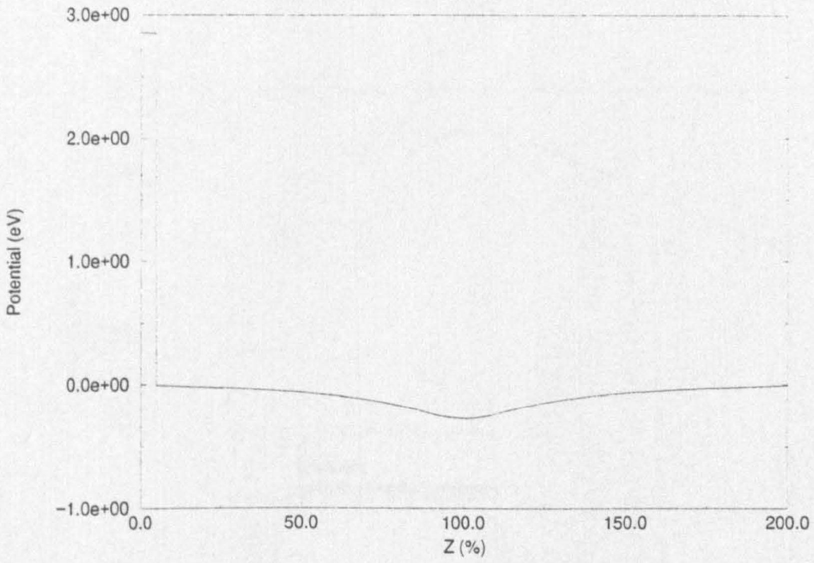

Figure 2.6: Band diagram of the conduction band edge with a terminating surface barrier, when donors are placed at Γ_d=100 Å.

2.3 Results

The calculations show that a wide range of surface electric fields can be expected ranging from high negative values to high positive ones. As might be expected, the electric fields can be controlled by varying several parameters, all of which can be adjusted via the growth stage. These parameters include the QW width, the donor position and the donor concentration. In the calculations, the total length of the whole system was kept fixed, with the wave function vanishing at the boundaries of the system.

In addition to the system involving a QW, a test system without such a QW was also modelled. This system is comprised of a flat band edge (with a terminating surface barrier) into which donor ions are introduced over a given region. We consider first such a system. Fig. (2.6) shows the resultant 'V' shaped potential well formed when bulk material is doped over a finite region with a constant donor density. This 'V' shaped potential is due to potential contributions given by the electrons and ions and was evaluated on the assumption that each donor has a single electron with the latter being confined in the 'potential well' created by the ionized donors. The surface electric field is given by the gradient of this potential at the surface.

Fig. (2.7) shows the contribution made by each term to the overall energy. For the situation when the donors are placed at the centre of the system (i.e. Γ_d=100 Å, where the system is defined as the surface layer, and the flat band) the exchange and correlation terms play little part in determining the surface field. If the donors were situated closer to the surface the exchange and correlation terms would play a much larger part in determining the overall energy, and hence the surface field. For the case of the surface barrier shown in Fig. (2.6) the surface field is negative. Fig. (2.8) shows the surface electric field as we move the donors through the system. As expected the surface electric field tends to zero as the donors are moved further from the surface. The reason is that the exchange and correlation term due to the electrons (which sit in the 'V' shaped well produced by the donors) is negligible and the coulombic and ionic terms cancel.

In the previous calculations a 3 eV barrier height was used since this is typical of the work function of a surface layer. Increasing the barrier height reduces the contribution of the

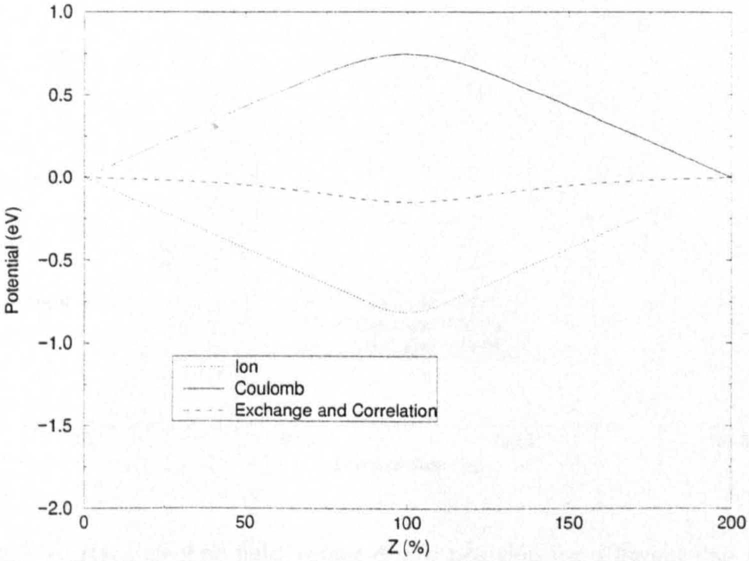

Figure 2.7: Potential energy diagram showing the contribution made by each term to the overall energy.

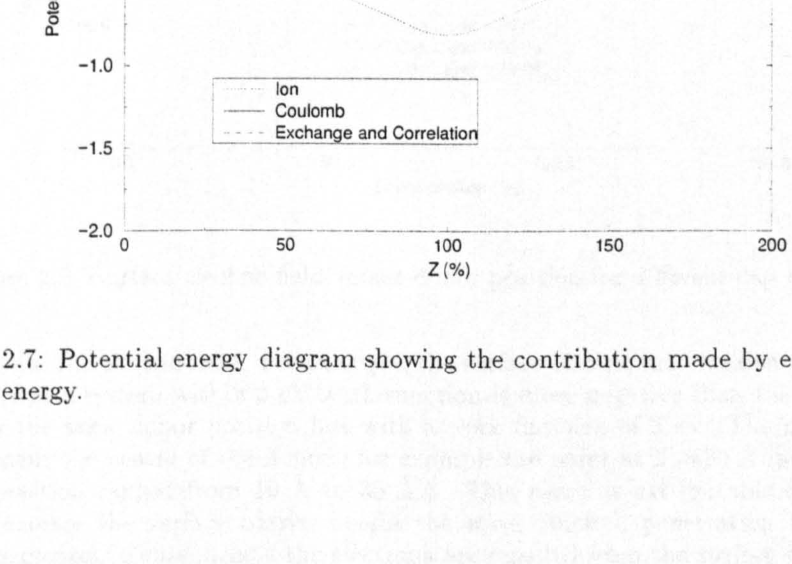

Figure 2.8: Change in surface electric field with movement of donor position, for a flat band.

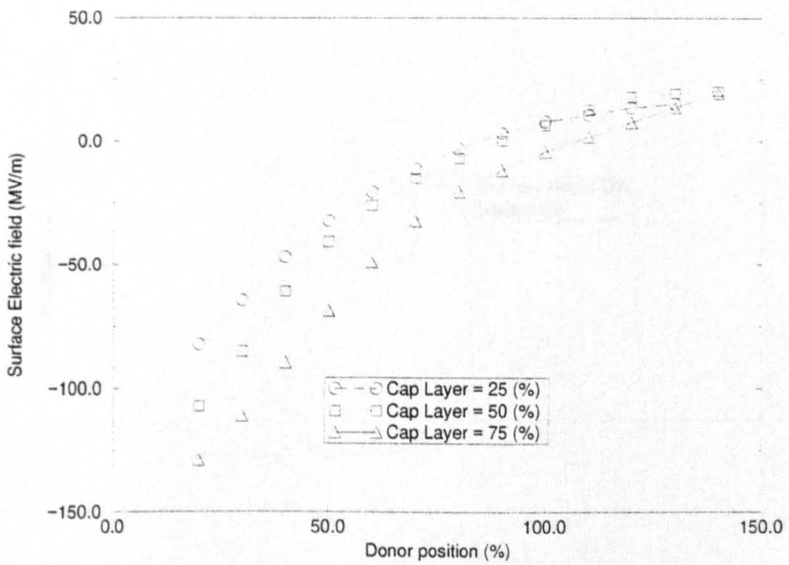

Figure 2.9: Surface electric field versus donor position for different cap layer widths.

electrons to the electric field. For example, the surface electric field for donors positioned at Γ_d=20 Å in a system with a 6 eV work function is more negative than the surface electric field for the same donor position but with a work function of 3 eV (The points are taken to represent the centre of the donors, for example the point at Γ_d=20 Å indicates that the donor position ranged from 10 Å to 30 Å.). This result is attributable to the fact that as we increase the surface barrier height the wave function penetration into the barrier region decreases. Consequently the electrons are repelled from the surface region and their contribution to the surface electric field decreases. Note that as we increase the barrier height, the wave function penetrates the barrier less, and the density of electrons within the barrier region decreases significantly. Consequently the approximation used for calculation of the exchange correlation term is of decreasing validity in this region. [16]

We now turn to the situation where a QW is present in the structure. One possible variable is the thickness of the cap layer. Typically we chose a 50 Å cap layer. However the effect of varying the length of the cap layer is shown in Fig. (2.9). Each curve represents in Fig. (2.9) the surface electric field as the constant donor region (of width 20 Å, and the donor density $4 \times 10^{24}/\mathrm{m}^3$) is moved through the structure with the QW width kept fixed at 50 Å. Considering the curve with a cap layer of 50 Å we can see that as we move the donors through the structure we go from a very large negative electric field (~ -100 MV/m) to a point where the surface electric field is zero, and as we move the donor position further away from the surface we obtain a very large positive electric field ($\sim$ 20 MV/m). This illustrates the sensitivity of the surface electric field to the donor position, and how by simply changing the donor position, we can alter the sign of the electric field from negative to positive. Fig. (2.9) also shows the effect of different cap layer thicknesses. It can be seen that as we bring the QW closer to the surface (by reducing the cap layer) we increase the effect of the electrons on the surface electric field thus making the electric field more positive. Thus for a cap layer thickness of 25 Å we have a more positive electric field than that for a cap layer thickness of 50 Å. However, when the donors are positioned at large distances from the surface, the electric fields for all the cap layers are similar. This effect is a result of the electrons being confined to the 'V' shaped donor potential well rather than the QW. Fig. (2.10) shows a potential profile of a typical system, before and after the addition

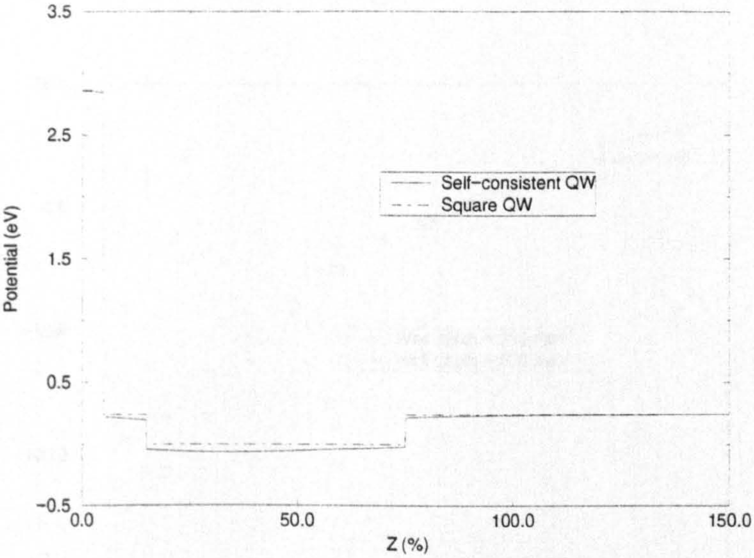

Figure 2.10: Band diagram of the conduction band edge for a square QW without any donor region and a self-consistent QW potential where the donors are placed at Γ_d=30 Å.

of the donors. It can be seen that the addition of donors leads to a 'band-bending' effect which in turn gives rise to the very large surface electric fields.

Fig (2.11) shows the effect of varying QW potential depths on the surface electric field. It shows that if we increase the depth of the QW the electrons have a greater effect on the surface electric field.

The QW width was another possible variable, Fig. (2.12) shows the effects of changing the QW width on the surface electric field. Again there is only a significant difference when the donors are placed further from the surface, the trend seems to be that for this region the wider the QW the more negative the surface electric field, thus this suggests that the wider the QW the fewer the number of electrons that contribute to the surface electric field.

As well as doping a heterostructure with donors, it is also possible to dope with acceptors. The same theoretical technique is applicable as for the donor case. Fig. (2.13) shows a comparison between the dopant position and the surface electric field, for both donors and acceptors. It can be seen that the acceptors produce positive electric fields whose magnitudes are larger than those associated with the donors. This results from the higher effective mass of the holes which leads to them being more confined in real space than the electrons associated with the donors.

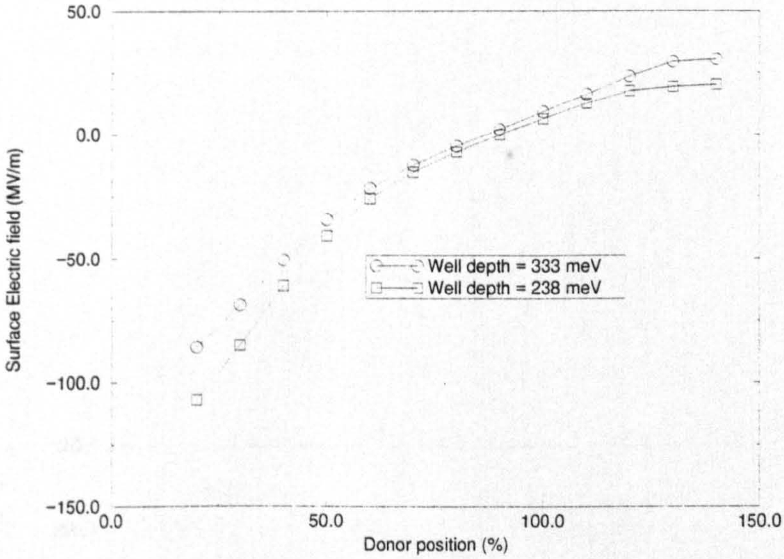

Figure 2.11: Change in surface electric field with movement of donor position, for differing QW potential depths.

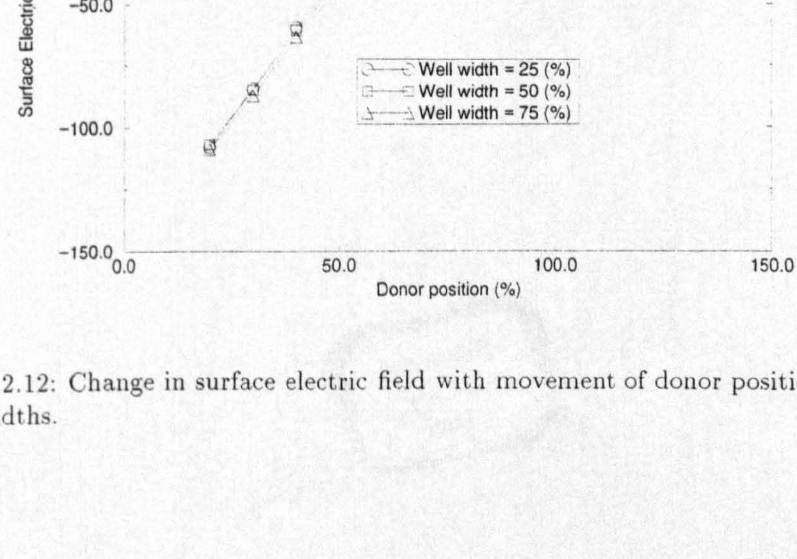

Figure 2.12: Change in surface electric field with movement of donor position, for differing QW widths.

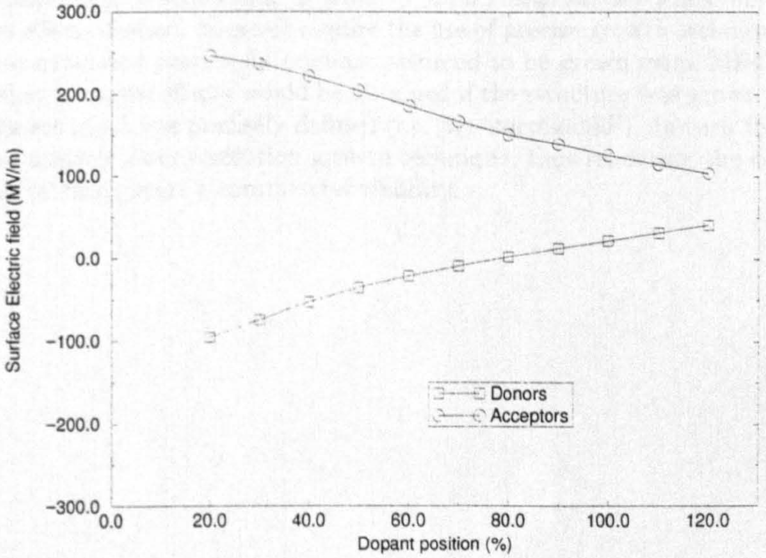

Figure 2.13: Change in surface electric field with movement of donor position, for donors and acceptors, when applied to a system of length 130 Å.

2.4 Conclusion

In this section we have modelled the effects of a QW, together with a highly doped region, on the magnitude of the surface electric field. By varying growth parameters (such as QW width, position of the doped region, position of the QW relative to the surface etc.) it has been demonstrated that the magnitude of the surface electric field can be tuned through very large ranges of positive and negative values. This effect could be of extreme importance for the control of a catalytic reaction, where such large surface fields could be used to influence the mobility of atoms/ions and also the electronic structure of the active sites. Currently we have no technique whereby we can locate a catalytically active phase in a controllable and unambiguous electronic environment, thereby modulating the normally binding correlations between electronic character and geometric structure. However as we have demonstrated in this chapter, the use of semiconductor heterostructures to control the electronic structure is clearly possible, since the electronic structure of the semiconductor materials themselves is relatively well understood. In this manner the hope is to achieve novel catalytic activity and control in a wider range of catalytic processes.

It is important to stress that in order to obtain large surface fields, and hence to achieve the novel effects desired, does not require the use of precise growth techniques. Although the structures examined previously are ones assumed to be grown using MBE, it can be shown readily that the same effects would be obtained if the structure was grown with a QW whose interfaces are much less precisely defined (i.e. are 'corrugated'). In turn this means that one could use a much lower resolution growth technique, thus rendering the control of catalytic processes by this means a commercial viability.

Bibliography

[1] C.Weisbuch and B.Vinter, Quantum Semiconductor structures (Boston, Academic Press, 1991).

[2] W. E. Hagston, S. J. Weston, M. O'Neill, T. Stirner, P. Harrison, J. H. C. Hogg, D. E. Ashenford and B. Lunn. J.Vac.Sci.Technol.B.**12**,1146 (1994).

[3] E. F. Schubert. Optical and Quantum electronics. **22**,S 141 (1990).

[4] M. Leroux, N. Grandjean, C. Deparis, J. Massies, C. Lopez, R. Mayoral and F. Meseguer. Jpn.J.Appl.Phys.**34**,3437 (1995).

[5] G. Collier, D. J. Hunt, S. D. Jackson, R. B. Moyes, I. A. Pickering, P. B. Welles, A. F. Simpson and R. Whyman. J.Catal.**80**,154,(1983).

[6] D. J. Hunt, S. D. Jackson, R. B. Moyes, P. B. Welles and R. Whyman. J.Catal.**86**,333,(1984).

[7] S. D. Jackson, R. B. Moyes, P. B. Wells and R. Whyman. J.Catal **86**,342 (1984).

[8] H. Ohno, E. E. Mendez, J. A. Brum, F. Agullo-Rueda, L. L. Chang and L. Esaki. Phys Rev.Lett.**64**,2555 (1990).

[9] S. Fafard. Phys Rev B.**46**,4659 (1992).

[10] R. H. Yu. Phys Rev B.**47**,1379 (1993).

[11] S. Fafard. Phys Rev B.**50**,1961 (1994).

[12] R. H. Yu. Appl.Phys.Lett.**65**,1531 (1994).

[13] M. Zaluzny. Appl.Phys.Lett.**60**,1486 (1992).

[14] F. Agullo-Rueda. Phys Rev B.**42**,1470 (1990).

[15] S. Fafard, R. Fortin and A. P. Roth. Phys Rev B.**45**,1376 9 (1992).

[16] P. Ruden and H. Döhler. Phys Rev B.**27**,3538 (1983).

Chapter 3

A melting model for pulsed laser processing of Silicon thin films

3.1 Introduction

The growth of interest in polycrystalline Silicon thin film transistors (poly-Si TFTs) over the past decade has been due to the commercial development of active matrix-addressed flat panel liquid crystal displays (AMLCDs). The current technology is such that AMLCDs use amorphous Silicon thin film transistors (a-Si TFTs). Although these devices work adequately, they are limited from being developed to form Integrated drive circuits on the active matrix plate owing to the low electron field effect mobility. This mobility problem could be overcome by the use of poly-Si TFTs since these have a superior field effect mobility (over 100 times that of a-Si)[1] [2].

There are a variety of ways of forming thin film poly-Si. These include direct deposition of the poly-Si onto a substrate as well as conversion from a-Si by either solid-phase crystallization or by laser crystallization. The investigations undertaken are guided by commercial viability. Thus, e.g, although the use of a high temperature technology based on utilising quartz substrates is possible, only low temperature processes are actually considered as a result of economic considerations. This allows the use of inexpensive glass substrates and means that mass production of devices is easily attainable.

The objectives of the present research are to model the heat conduction within a semiconductor arising from an incident laser pulse, with a view to gaining an understanding of the recrystallization process involved in transforming a-Si to poly-Si. Once the processes are understood, the object is to utilise the model to aid the experimental realisation of the formation of thin films of poly-Si from a-Si. Since ultimately the production of poly-Si TFTs on glass are required, thin films of a-Si on glass substrates were modelled[2]. When raising the temperature of the a-Si using a pulsed laser the time scales involved are very small. Typically the temperature of the sample may be raised in a few nanoseconds from ambient to the melting point, if the laser pulse is sufficiently powerful. Over these temperature ranges the thermal conductivity (K) specific heat (c) and density (ρ) are not constant.

It can be seen from Fig (3.1) that for crystalline Silicon (c-Si) the temperature dependency of the thermal conductivity is large and that it would not be correct therefore to assume a constant value for all temperatures. It is also noticeable that there is a quasi-discontinuity in K which occurs on melting, when the material properties change from those of a semiconductor to those of a metal. Such effects are clearly important when trying to

---

[1] a-Si TFTs have a channel mobility no more than $1cm^2/(V.s)$, where as it has been reported that for poly-Si the TFT channel mobility is in the region of $200 - 300cm^2/(V.s)$ [1]

[2] 150nm of a-Si on a 850nm glass substrate and 450nm of a-Si on a $1\mu m$ glass substrate.

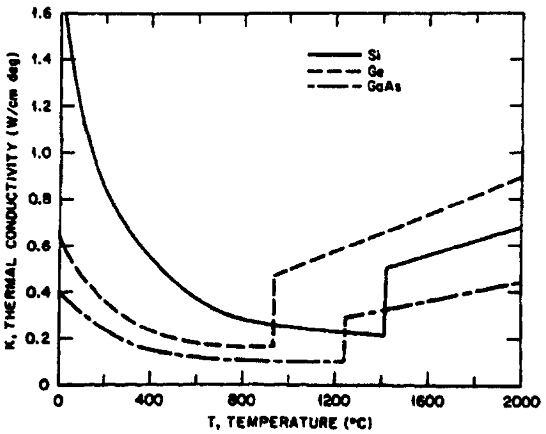

Figure 3.1: Temperature dependency of thermal conductivity for three crystalline semiconductors [3].

Latent heat	*J/g*
crystalline	1800
amorphous	1320
vaporization	16207

Table 3.1: Thermodynamic data for Si [3, 4].

model the heat flow and must therefore be accounted for properly. Besides the temperature dependent properties another important consideration is the incorporation of the latent heat into the problem. When a-Si reaches it's melting point it must overcome the latent heat of fusion before it is transformed into its 'molten' state. However, in the problem under consideration, the transition from solid to liquid occurs in parts of the sample only. Consequently, during the various transition stages the material goes through a 'two-phase mixture referred to as slush or mush' [3] and this must also be allowed for when dealing with its properties.

Table (3.1) shows some thermodynamic data for Si. From this table it can be seen that the latent heats for c-Si and a-Si are different (as a result of their different crystal structures). Thus when a transition from a-Si to c-Si via molten Si occurs, differing amounts of latent heat are involved.

The relevant physical parameters of the glass substrate were assumed to have a negligible temperature dependence. This means that the heat flow problem can be dealt with in a straightforward manner for the substrate. The properties of the latter are very different from those of molten or c-Si. Hence when dealing with the interface (which always occurs at the substrate) an appropriate technique must be employed since many of the physical properties of the materials change abruptly there. Such abrupt changes can give rise (via derivative terms in the differential equation) to the appearance of Dirac-delta functions in the equations. It is essential therefore, to avoid non-physical effects resulting from such mathematically singular terms. A means of achieving this in the numerical simulations is described later.

In general, heat flow in materials irradiated with laser pulses constitutes a three dimensional problem. However for short-pulse irradiation, the thermal diffusion distances are very much smaller than the dimensions of the laser beam. As a result the temperature gradients perpendicular to the surface are many orders of magnitude greater than the gradients parallel to the surface. This means that it is usually a good approximation to treat the heat conduction problem as a one dimensional one [3]. To determine the resulting temperature gradients in the system one has, in general, to solve therefore the following two heat conduction equations,

$$\frac{dQ}{dt} = -K\frac{dT}{dx} \tag{3.1}$$

$$\frac{dT}{dt} = \frac{dQ}{dt}\frac{1}{mc} \tag{3.2}$$

Where Q is the heat transfer, t is the time, T the absolute temperature and m the mass of the element being considered. Unfortunately these two heat conduction equations are general equations which do not include the effect of heating due to the laser pulse. Consequently they must be combined into a single differential equation which includes a heat generation function $P(x,t)$.

$$\rho c\frac{\partial T(x,t)}{\partial t} - \frac{\partial}{\partial x}\left(K\frac{T(x,t)}{\partial x}\right) = P(x,t) \tag{3.3}$$

Clearly this equation is mathematically similar to the equation of continuity with a source term present. The heat generation function is determined by the interaction of the laser radiation with the sample and the subsequent transfer of the energy to the lattice [5]. The incident pulse has certain characteristics which depend on the type of laser employed. Such characteristics can thus be varied by making a different choice of laser. A $XeCl$ eximer laser was used in experimental work in the laboratory [6]. Consequently when modelling the laser pulse the characteristics of such a laser were employed, these characteristics include pulse shape, wavelength, absorption depth, reflectivity and duration of pulse (variable). From the information about the pulse, the amount of energy transfered to the lattice per unit time can be determined and consequently the temperature rise due to this energy can be calculated.

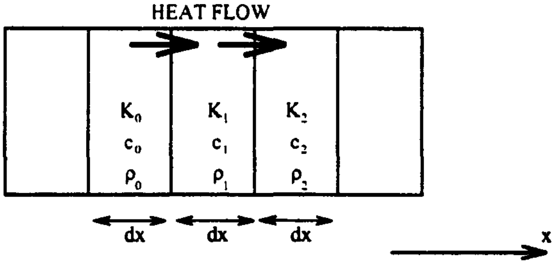

Figure 3.2: Diagrammatic representation of heat flow from adjacent nodes.

3.2 Theory

To obtain the temperature gradients the heat conduction equation (equation (3.3)) was solved using a finite difference technique. To apply the latter, the physical problem is approximated by a set of nodes along the x axis, each node being associated with a small volume of material having prescribed thermal properties. The heat flow between adjacent nodes is then modelled [3]. Fig (3.2) illustrates the heat flow involved. An appropriate choice of the time steps and the increments between the nodes enables an accurate solution to the differential equation to be made. Rewriting equation (3.3) in the form

$$\frac{\partial T(x,t)}{\partial t} = \frac{P(x,t)}{\rho c} + \frac{1}{\rho c}\left[\frac{\partial K(x,t)}{\partial x}\frac{\partial T(x,t)}{\partial x} + K(x,t)\frac{\partial^2 T(x,t)}{\partial x^2}\right]$$

leads to the finite difference equation (c.f. 1.3.2)

$$\begin{aligned}&\left[\frac{T(x,t+\delta t) - T(x,t)}{\delta t}\right] = \\ &B(x,t) + \frac{1}{\rho c}\left\{\frac{[K(x+\delta x,t) - K(x-\delta x,t)][T(x+\delta x,t) - T(x-\delta x,t)]}{(2\delta x)^2}\right\} + \\ &\frac{K(x,t)}{\rho c}\left\{\frac{T(x+\delta x,t) + T(x-\delta x,t) - 2T(x,t)}{(\delta x)^2}\right\}\end{aligned} \tag{3.4}$$

where $B(x,t) = P(x,t)/\rho c$.

The two stationary boundary conditions imposed on these equations are the following

$$\left(\frac{\partial T(x,t)}{\partial x}\right)_{x=0} = 0, \qquad and \qquad T(x,t)_{x\to\infty} = \ constant.$$

The first condition implies that there is no heat loss from the surface, whilst the second reflects the fact that the sample must be thick enough to act as a good heat sink [3]. In numerical calculations, the two boundary conditions are readily implemented, by ensuring that the temperatures of the first two nodes are equivalent, and that the number of nodes is such that the last one remains at room temperature [3].

3.2.1 Heat generation function

The heat generation function $B(x,t)$ is evaluated on the assumption that the laser pulse has a rectangular form which can be divided into small elements.

Fig (3.3) shows the shape of a typical pulse employed in the calculations; using such a pulse means that it can be divided into small time elements of length δt. Consequently at

---

[3] Room temperature is taken to be 300 Kelvin.

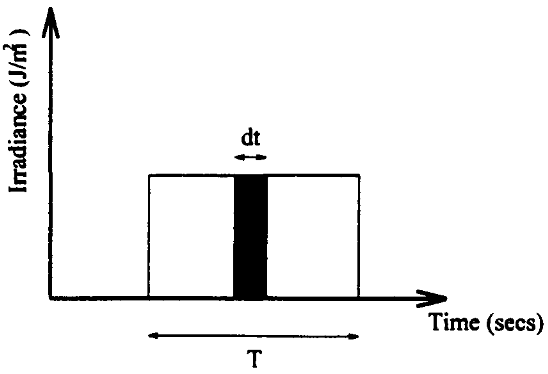

Figure 3.3: Typical pulse shape used in calculations of temperature profiles.

a time δt in the future, only the energy contained in the shaded region is transferred to the lattice.

Using

$$E = mc\Delta T$$

Where E=energy, m is the mass of the element, c is the specific heat capacity and ΔT the temperature rise, then

$$F = \text{Fluence} = \frac{E}{Area} = \frac{mc\Delta T}{Volume}\delta x$$

therefore

$$F = \rho c \Delta T \delta x \tag{3.5}$$

In this manner we can evaluate the temperature rise in an element δx resulting from an element of the pulse of duration δt. This model assumes complete absorption of all the pulse energy; it does not take into account reflectance at the surface. Thus the more general form is

$$\Delta T = (1 - R)\frac{F}{\rho c\,\delta x} \tag{3.6}$$

where R is the reflectance (note $0 \leq R \leq 1$)

3.2.2 Treatment of the interface

Owing to the abrupt nature of the interface, and the rapid variation in the parameters on one side of the interface only, the two nodes at the interface are dealt with separately. The problem arises from a large change in K across the interface associated with the transition from molten Si to the glass substrate. From Fig (3.4) it can be seen that there is a large change in K values on going from the Si to the glass. As mentioned earlier this could cause mathematical difficulties in the evaluation of $\frac{\partial K}{\partial x}$ across this interface. One possible solution would be to increase the value of δx at the interface. This however gives rise to inaccuracies. Another solution is to proceed as follows. We note that initially

$$\frac{\partial K}{\partial x} = \frac{K_{Si,initial} - K_{substrate}}{node} = P \qquad \text{(say)}$$

Once the pulse is applied,

$$\frac{\partial K}{\partial x} = \frac{K_{Si} - K_{substrate}}{node}$$

$$= \frac{K_{Si} - K_{substrate}}{K_{Si,initial} - K_{substrate}} \frac{K_{Si,initial} - K_{substrate}}{node}$$

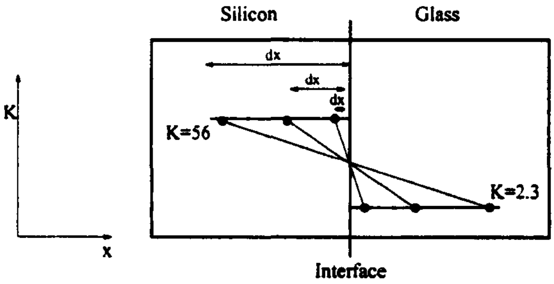

Figure 3.4: Diagram showing the abrupt step in the K values at the interface.

Hence [4]

$$\frac{\partial K}{\partial x} = \frac{K_{Si} - K_{substrate}}{K_{Si,initial} - K_{substrate}} P$$

3.2.3 The mathematical criteria for the validity of the modelling

The criteria that must be satisfied in the modelling, is a mathematical one related to stability. Von Neumann [5] gives a necessary condition, which reads

$$\frac{L}{\delta x_{calc}} \leq \sqrt{0.5}$$

Where δx_{calc} is the node size and L is the diffusion length given by

$$L = \sqrt{\left(\frac{K}{\rho c}\delta t\right)}$$

From this it follows that

$$\frac{K}{\rho c}\delta t \leq \frac{(\delta x)^2}{2}$$

This criteria is fulfilled readily in the calculations, by an appropriate choice of δt and δx. From the present problem the condition is always satisfied provided δt is in the region of 1×10^{-14} seconds and δx_{calc} is 1×10^{-9} metres.

---

[4] A similar problem arises when a phase change occurs. In order to change phase a given node representing, say, a solid semiconductor element, must absorb the latent heat of fusion before it displays the properties of the molten semiconductor. However this is a dynamic process during which the semiconductor node will be in a 'slush' state. When calculating the thermal conductivity this transition from solid to liquid must be smoothed. This can be done by tracking the fraction of the latent heat that the node has received, and evaluating K as follows,

$$K = (1 - x)K_{Si} + xK_{liq,Si}$$

where K_{Si} is the K value prior to the phase change and $K_{liq,Si}$ is the K value of molten Si.

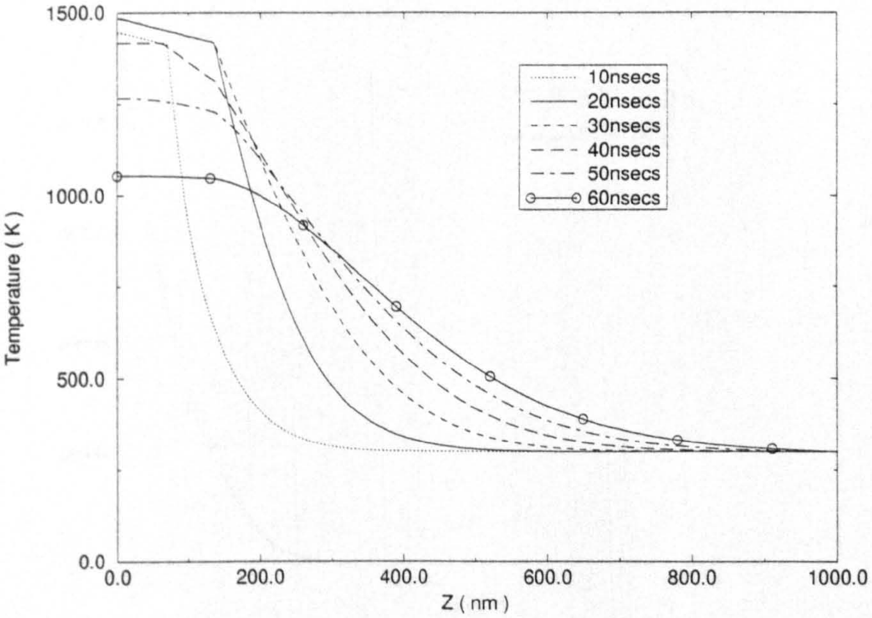

Figure 3.5: Temperature profile for a 2000J/m^2, 30ns pulse incident on a 150nm Si film sat on top of 850nm of glass substrate, at various times during and after the pulse.

3.3 Results and Discussion

The solution of equation (3.4) gives the temperature profiles for a thin film system[5] at any moment in time, as a function of the depth in the sample. A collection of such profiles gives a history of each node from which it can be deduced whether or not it has had the opportunity to recrystallize from the molten phase or has stayed amorphous. As an example, Fig (3.5) shows the history of a 150nm Si film on a 850nm glass substrate during a laser annealing process. It can be seen that for this particular case the whole sample undergoes a phase change. On changing phase, as a result of the very large increase in thermal conductivity of molten Si compared with a-Si, the temperature becomes pinned at just above the melt temperature. The abrupt changes in the temperature profile result from the abrupt changes in the thermal conductivities of adjacent nodes. On cooling, any a-Si that has overcome the latent heat of fusion thus enabling it to melt, recrystallizes into poly-Si which again has a different thermal conductivity. Since poly-Si has a much higher thermal conductivity than a-Si, the system cools more uniformly. Although, in the present example, the whole of the Si film will have recrystallized into poly-Si we have no way of knowing , at the present stage of our understanding, the distribution of grain sizes. However we do know, for example, that at different ends of the sample the cooling rates are not the same. A combination of this knowledge with experimental observations of the grain size distribution will ultimately enable us to formulate a criterion for grain size formation and this is discussed later.

It is interesting to note that the solution of equation (3.4) involves temperature dependent properties, for example the thermal conductivity. Due to this temperature dependency, the resulting temperature profiles are different from the standard curves shown in texts. This is because the latter are obtained by solving the problem with no temperature dependent properties or inclusion of latent heat. In order to form a check on the method the temperature dependency was removed from the model and a low enough laser fluence chosen such that

---

[5] The system is defined as the thin film (150nm,450nm) and the substrate (850nm,1μm).

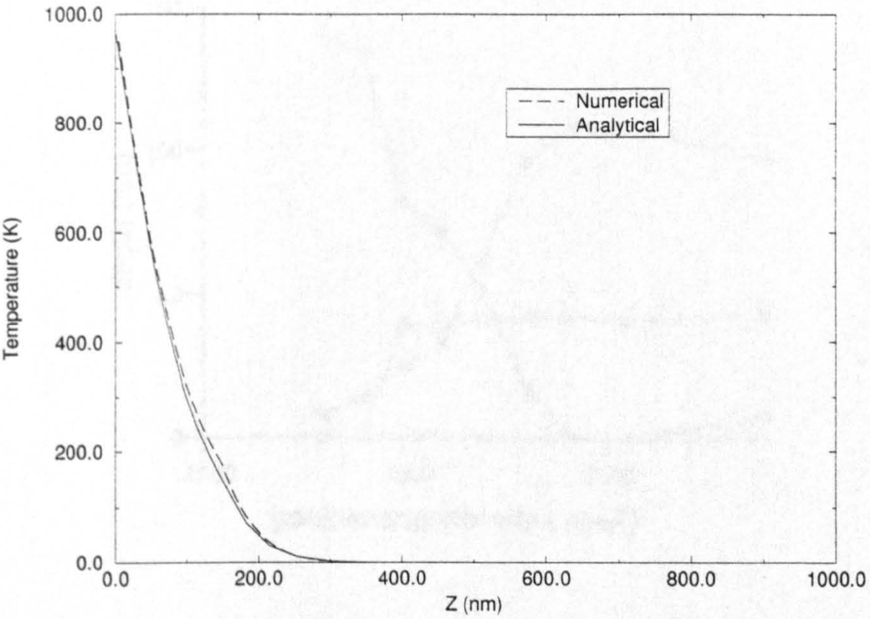

Figure 3.6: Comparison of model used with an analytical solution in which we have no temperature dependent properties.

latent heat would not be involved in the process. From Fig (3.6) we can see that in this simple case, where we have no latent heat or temperature dependent properties, the model used gives results virtually identical with the analytical solution. This gives us confidence that the model can be used for more the complex situations, where latent heats and temperature dependent properties are the norm.

In general, if a thin film of a-Si of thickness 150nm, is considered, then dependent on the parameters of the laser pulse differing amounts of a-Si will be recrystallized. One of the complicating features of the problem is that, it is found experimentally that even nominally similar samples behave differently as regards the amount of a-Si remaining in the film after it has been laser annealed with a 30ns pulse of various fluences. This is due to difficulties in producing two identical a-Si films. Other complicating features are the experimental values of the thermal constants; since two samples of a a-Si film may vary so significantly, the data recorded regarding thermal constants may also vary. Thus the data used in the theoretical calculations, were the most commonly accepted values from the literature [7, 8]. Nonetheless, although there is no absolute certainty about the thermal constants employed, the objectives of the theoretical calculations are still achieved, namely to find general trends which can guide experimental development.

The recrystallization process from the melt will clearly be dependent on the cooling rate of the sample i.e, the meltfront velocity. Since the latter is not uniform across the film, it is not unreasonable to expect the size of grain to be different for these variable cooling rates. It is found experimentally that, e.g with a 2000 J/m^2, 30ns pulse, the surface forms large grain crystals whereas deeper into the sample fine grains occur. Fig (3.7) shows experimental results by Sands et al [9], where the 150nm thin film is annealed at differing fluences, as described earlier. The graph shows the variation with fluence of the thickness of the large grained, fine grained and residual amorphous silicon. It can be seen that there is a saturation value to the amount of large grain silicon produced, and that raising the fluence from 1500 J/m^2 to 2000 J/m^2 does not effect the amount of large grain material. Instead increasing the

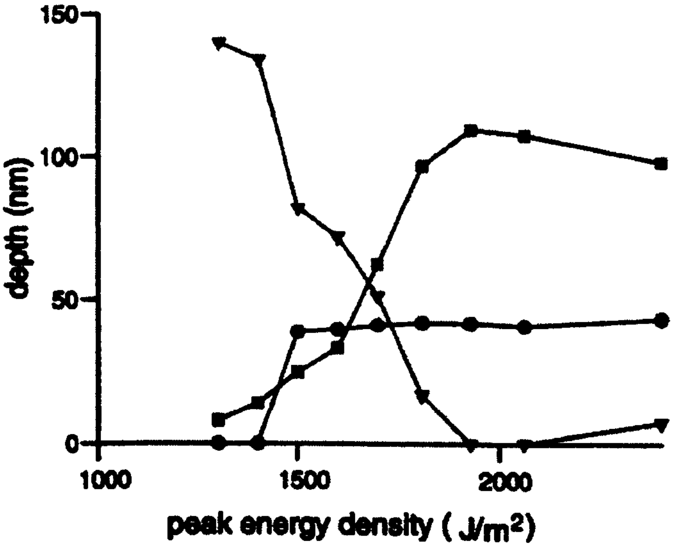

Figure 3.7: The thicknesses, as derived from reflectivity experiments, of the residual amorphous silicon (triangles), fine-grained poly-Si (squares), and large-grained poly-Si (circles) for a 150nm thin film of laser annealed amorphous silicon. Plotted as a function of peak fluence.

fluence in this region increases the amount of fine grain Poly-Si at the expense of amorphous Si. One other interesting feature of the results is the sharp transition from no large grained poly-Si to a saturated value.

Clearly the meltfront velocity plays an important role in determining the dynamics of grain formation and ultimately the grain size. Hence in order to try and explain the experimental observations, one could suggest that when the meltfront velocities lie within cetain limits large grain formation occurs. Clearly for a fluence of 1500 J/m^2 the meltfront velocity is conducive to only fine grain formation, whereas from 1500 J/m^2 to 2000 J/m^2 there are certain regions where the meltfront velocity is such that large grains can form as well. Using this line of argument, it should be possible to produce more large grains by determining which range of velocities give rise to large grained poly-Si and applying a fluence which will give the desired velocities. In an attempt to simplify the problem, we will deal with average meltfront velocities.

A 150nm thin film was modelled and the meltfront position was calculated for a range of fluences. Fig (3.8) shows the meltfront position against time, after the 30ns pulse has finished. The theoretical results show that for fluences exceeding 1600 J/m^2 the meltfront recedes from the film-substrate interface, thus suggesting melting throughout the sample. This is in disagreement with the experimental results which show that at such a fluence, there is still ~50nm of residual amorphous silicon. This anomaly is believed to be due to the lack of accurate data available for the thermal constants of amorphous silicon, and errors in the optical reflectivity measurements used in the experiment. However since it is trends in changes that are of importance, we retain the same set of constants througout all the simulations. In the graph it can be seen that the meltfront position for fluences of 1600 J/m^2 to 2000 J/m^2 are virtually identical. Because of this it follows that their average meltfront velocities are almost identical at a value of 2.5m/s. As the fluence is increased to 3000 J/m^2, 4000 J/m^2 and 5000 J/m^2 the curves change noticeably and the average meltfront velocity increases appreciably to values of 7m/s, 7.5m/s and 8m/s respectively.

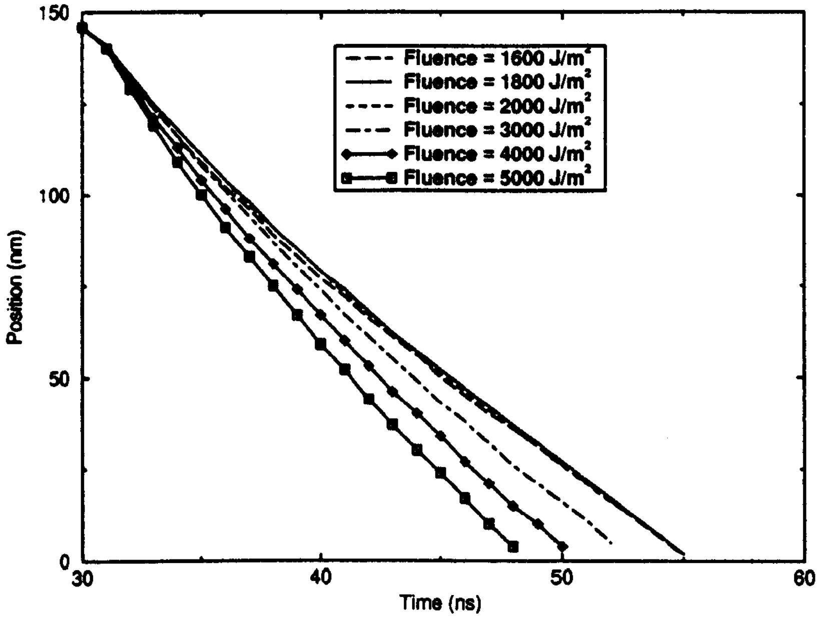

Figure 3.8: Meltfront position, as a function of time, for a 150nm thin film of Si, after the termination of a 30ns laser pulse.

The results are consistent with the experimental results shown in Fig (3.7), in the sense that there is a saturation in the formation of large grained poly-Si between 1500 J/m^2 and 2000 J/m^2 where the average meltfront velocity is the same. Using these results it is possible to predict that large grain formation throughout the thin film will occur at these higher fluences. However due to lack of experimental data at larger fluences it is not possible to test this hypothesis. To examine this possibility further a thicker film was modelled, since experimental data was available for such films. In particular a 450nm sample was considered, the experimental and theoretical results of which are discussed next.

The system considered was thought initially as a result of optical measurements, to be a 400nm thin film of a-Si on a 1μm glass substrate. This system was chosen since experimental results of grain formation over a large fluence range were readily available [10].

Fig (3.9) shows the variation with fluence of the regions of large grain, fine grain and residual amorphous silicon formation. The graph shows trends which are similar to the previous experimental curve in Fig (3.7) in that it displays a threshold fluence below which there is no large grain formation. Similarly there is a saturation in the amount of large grain poly-Si produced for fluences between 1600 J/m^2 and 2000 J/m^2. It can be seen from Fig (3.9), that at higher fluences the large grain poly-Si is the most dominant grain size within the annealed film. It can also be seen that the large grain formation increases linearly for fluences above 2500 J/m^2. Thus by analysis at these large fluences it should be possible to determine a range of average meltfront velocities which will give large grained poly-Si throughout the sample. To this end, using a more accurate experimental technique of TEM the thin film annealed at 9500 J/m^2 was observed. The resulting picture of the sample is shown in Fig (3.10), which shows large grain formation throughout the whole sample. The grey region in Fig (3.10) is the substrate, but large grains are clearly visible throughout the film. Further more the TEM showed that the sample was actually 450nm thick. The latter shows the limitations placed of the optical reflectivity measurements and raises doubt about the parameters obtained in this manner. In particular the values of the

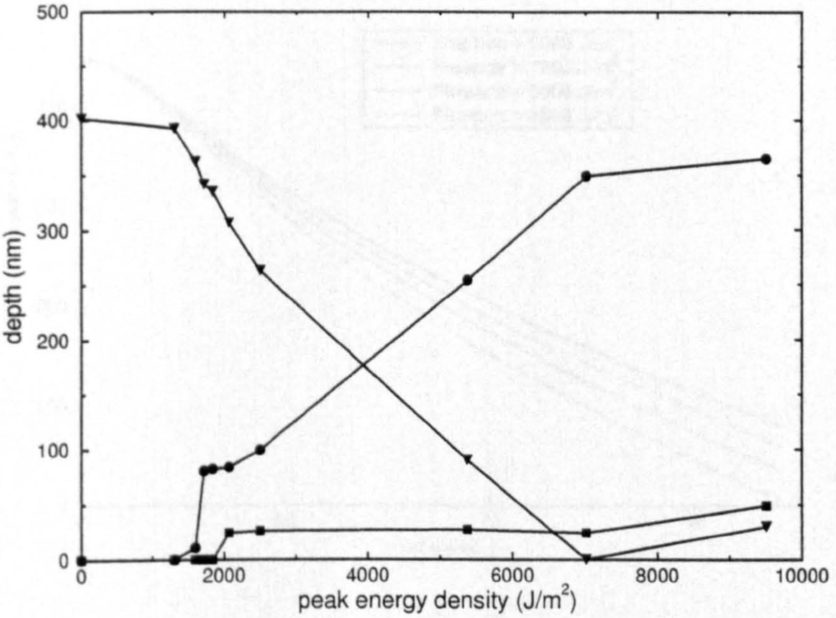

Figure 3.9: The thicknesses regions, as derived from reflectivity experiments, of the residual amorphous silicon (triangles), fine-grained poly-Si (squares), and large-grained poly-Si (circles) for a 450nm thin film of laser annealed amorphous silicon, plotted as a function of peak fluence.

Figure 3.10: TEM picture of a laser annealed 450nm thin film of amorphous silicon, annealed at a laser fluence of 9500 J/m^2.

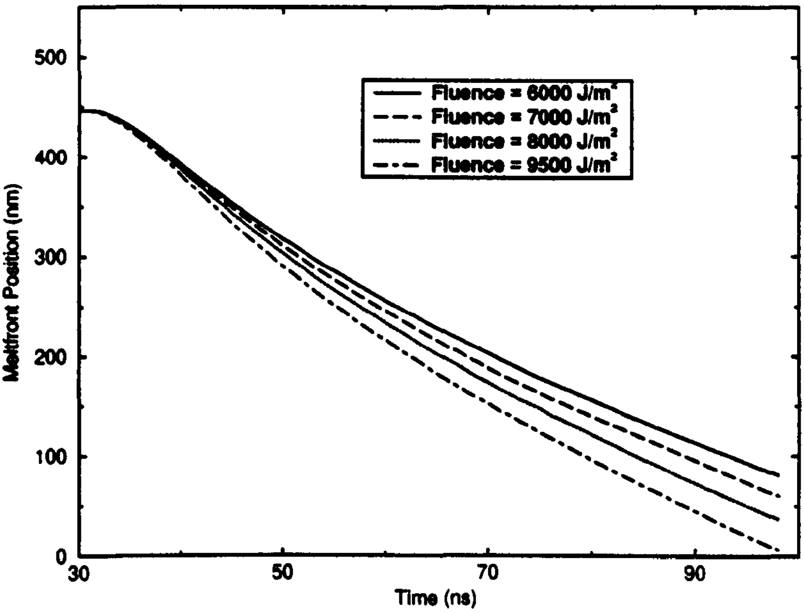

Figure 3.11: Meltfront position, as a function of time, for a 450nm thin film of Si, after the termination of a 30ns laser pulse.

depths for the various 'grains' appearing in Fig (3.9) are on the low side as a result of errors of measurement. Nonetheless the trends observed will still be accurate.

The meltfront position was calculated for a range of fluences from 6000 J/m^2 to 9500 J/m^2 and is shown in Fig (3.11). It can be seen that the meltfront velocity increases with fluence, thus suggesting that the greater the fluence applied to a sample of a-Si the faster the meltfront recedes away from the interface on cooling. The average meltfront velocities are found to be 6m/s and 7.5m/s for the 6000 J/m^2 and 9500 J/m^2 respectively. Since we have seen clearly from TEM measurements that a 9500 J/m^2 fluence will anneal the whole film, thus producing large grain poly-Si throughout the sample, we can conclude that an average meltfront velocity of 7.5m/s is necessary in order to produce such large grains. Using this as our guide, it is clear why large grains were not observed throughout the 150nm thin film, since no fluence had been applied which resulted in a meltfront velocity of this value in this region. The calculations show that if a laser pulse of fluence 4000 J/m^2 was incident on the sample then the average meltfront velocity would equal 7.5m/s, thus giving large grains throughout. As of yet this has not been verified experimentally.

3.4 Conclusion

The principle objective of the present work was to model a thin film system whose properties were temperature dependent. In this manner it was possible to understand the dominant features conrolling the size of grain formed. From the results it can be concluded that the size of grains formed is controlled by the meltfront velocity of the thin film, In turn, the latter is determined by the pulse fluence used in the annealing process. It has been shown that increasing the fluence of the pulse, increases the meltfront velocity, and consequently increases the amount of large grain poly-Si formed in the sample. By comparison with experiment, it has been shown that an average meltfront velocity of 7.5m/s appears to be a necessary condition for producing large grain crystals throughout the sample. On this basis we can predict that if a 150nm thin film of a-Si was anneallled at 4000 J/m^2, then large grains would be formed throughout the film. Due to the complexity of the problem, it is only possible to construct semi-empirical rules for large grain formation on the basis of a theoretical analysis of the heat conduction problem. Nonetheless a combination of more detailed experimental results together with the theoretical analysis should enable a more refined set of rules to be formulated which can determine criterion of both fine grain and large grain formation. Presently this is unattainable due to the lack of reliable experimental data.

The ultimate aim is to develop a reliable criterion for the laser annealling of thin film Si, so that large grains are formed throughout the sample. Once this has been achieved it can be used in the industry for the commercial development of AMLCDs and high mobility TFTs.

Bibliography

[1] H. Watanabe, H. Miki, S. Sugai, K. Kawasaki and T. Kioka. Jpn. J. Appl.Phys. **33**,4491-4498 (1994).

[2] S. D. Brotherton. Semicond. Sci. Technol. **10**,721-738 (1995).

[3] R.F.Wood and J.E.Jellison, "Melting model for pulsed laser processing", Pulsed laser processing of semiconductors. R.F.Wood, R.T.Young and C.W.White (New York Academic Press, 1984).

[4] S. Nakamura and T. Hibiya. International Journal of Thermophysics, **6**, 1061 (1992).

[5] R. K. Singh and J. Viatella. JOM, 20 (1992).

[6] D. Sands, G. Williams, P. H. Key, S. D. Brotherton and J. D. McCulloch, to be published.

[7] INSPEC 1988, Properties of Silicon, EMIS data review series, 2nd edn (London).

[8] INSPEC 1989, Properties of Amorphous Silicon, EMIS data review series, 2nd edn (London).

[9] D. Sands, G. Williams and P.H. Key, Semicond.Sci.Technol. **12**,750 (1997).

[10] J. D. Hoyland, private communication.

Chapter 4

Optimisation of Stark shifts induced by the Quantum Confined Stark Effect

4.1 Introduction

In recent years, the optical properties of low dimensional structures have been of great interest, and in particular the influence of electric fields on such properties. In bulk semiconductors the application of an electric field and the resultant shift and broadening of the band edge absorption is known as the Franz-Keldysh effect [1, 2]. In low dimensional structures, such as QW's, an electric field can be applied in one of two directions, that is along or perpendicular to the growth direction (z). When the field is applied perpendicular to the growth the electro-absorption effects are similar to those in bulk material, as shown in Fig (4.1) [3].

Fig (4.1) shows that with increasing applied electric field the excitonic peaks undergo broadening to such an extent that they become unresolvable for fields of the order of 48 kV/cm. However, on application of an electric field parallel to the growth direction, the broadening of the excitonic absorption peaks are dramatically reduced and, for rectangular QW's, the peaks shifted to longer wavelengths i.e. a red shift. This is known as the quantum confined stark effect (QCSE),[1] and is shown in Fig (4.2) [3].

The effect of the applied electric field on the band structure is simply to apply a gradient to the band edge, such that the QW in both the CB and the VB are 'tilted'. Fig (4.3) shows the effects of an applied electric field, on a rectangular QW, and how on application of this field, the electrons and holes begin to collect at the opposite ends of the well, with decreased energies. Thus on examination of the interband transition energy for a symmetric QW, (see Fig (4.4) [7]) the energies move to lower values with increasing field strength. It can be seen from Fig (4.4) that the curves are symmetric about the origin (zero field), this is due to the symmetry in the QW, and it has been shown by *Chen* and *Andersson* [7] that this is generally true for all symmetric potentials. Thus for symmetric potentials, in particular QW like structures, application of an electric field will lead to lower interband transition energies and consequently a movement of their excitonic absorption peaks to longer wavelengths. This red shifting effect has led to many new applications, such as high-speed optical modulators [8, 9], optical bistable devices [10] and photo-detectors [11].

---

[1] The Stark effect was first observed over eighty years ago as a splitting in the spectral lines of hydrogen gas with the application of an electric field [4]. The problem of the shift in exciton resonances is equivalent to that of the Stark shift of a confined hydrogen atom, hence the title QCSE [5], the two being formally exact within the effective mass approximation [6].

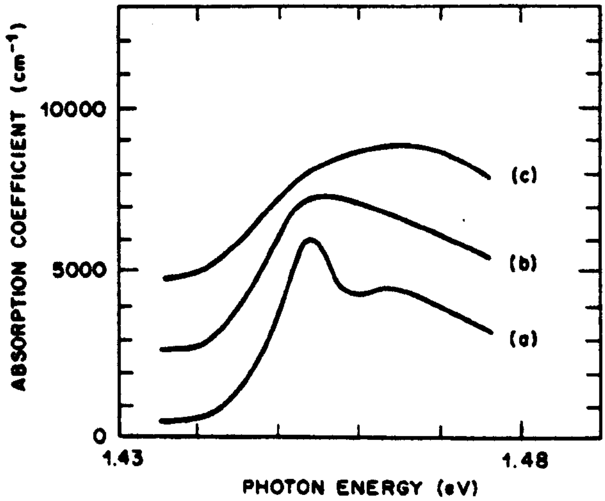

Figure 4.1: Absorption spectra at various electric fields for the perpendicular field case. (a) 0 V/cm, (b) 16 kV/cm, (c) 48 kV/cm.

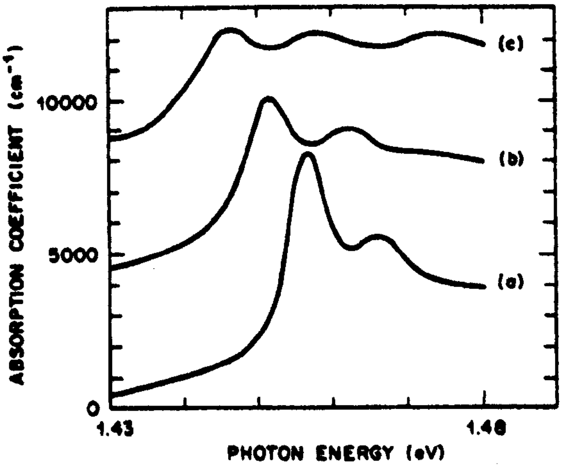

Figure 4.2: Absorption spectra at various electric fields for the parallel field case. (a) ≈ 10 kV/cm, (b) ≈ 47 kV/cm, (c) ≈ 73 kV/cm.

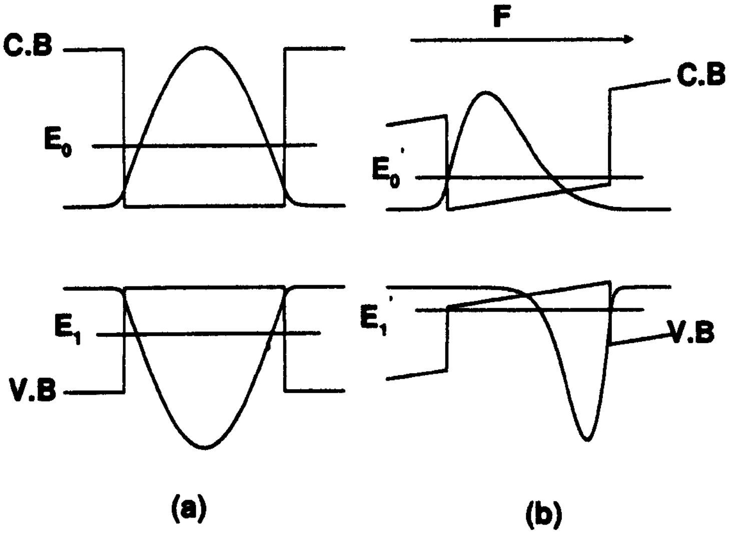

Figure 4.3: A QW system for (a) ϵ=0; (b) $\epsilon \neq$0.

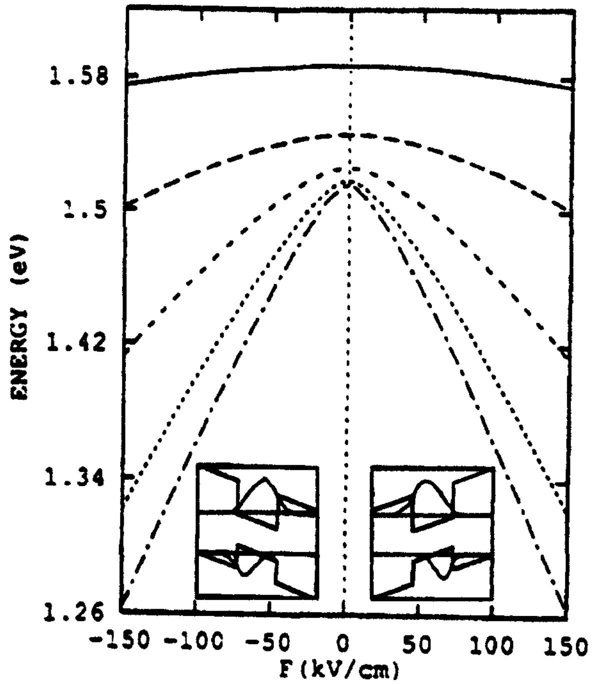

Figure 4.4: Interband transition energy as a function of the applied electric field for a square QW with increasing widths (top to bottom).

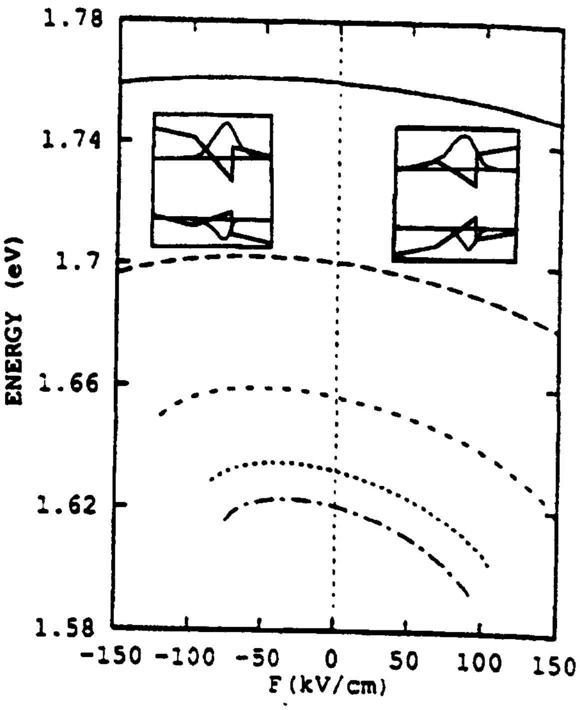

Figure 4.5: Interband transition energy as a function of the applied electric field for an asymmetric triangular well for increasing widths (top to bottom).

The above results are true for symmetric potentials. However if we consider systems which possess asymmetry in the band structure we observe significantly different results. In particular when an electric field is applied to an asymmetric QW (AQW) we find that there is an asymmetry in the interband transition energies with respect to the zero field position.

Fig (4.5) shows the interband transition energy for an asymmetric triangular QW. The curves are clearly not symmetrical about the origin, and on closer examination it can be seen that, at low negative fields a blue shift occurs in the excitonic absorption peak [2]. Thus by engineering the QW in such a manner as to create an asymmetry in the band structure, blue shifted line spectra can be observed for specific values of the electric field. Such systems clearly have attractive possibilities for the realisation of devices based on the 'blue shifted' QCSE, such as self electro-optic effect devices (S.E.E.Ds) [12, 13] and asymmetric Fabry-Perot reflection modulators [14].

Much interest has been shown in engineering QW structures such that their energy shifts in an electric field are maximised. This is generally developed by trial and error methods, and there is little or no mathematical optimisation applied [15, 16]. The object of the present section is to describe the results of a systematic optimisation procedure whereby the QW shape is modified in such a manner that a maximum blue/red shift can be achieved for a given value of the applied electric field. As described below, the QW shape is to be determined using an iterative optimisation technique within the framework of formal quantum theory. Using this technique, the optimum QW shape needed to produce a maximum blue/red shift can be obtained for given field strengths.

The shifting of the line spectra is dependent on many factors, including the material

---

[2] The blue shift in the absorption line spectra is observed for applied fields between 0 kV/cm and -50 kV/cm, beyond these values i.e -100 kV/cm the red shift QCSE is again present.

parameters, [3] and the applied field strength. The two systems to be considered for the purpose of illustration are CdTe/$\mathrm{Cd}_{1-x}\mathrm{Mn}_x\mathrm{Te}$ a II-VI semiconductor, and GaAs/$\mathrm{Al}_x\mathrm{Ga}_{1-x}\mathrm{As}$ which is a III-V semiconductor. However the optimisation technique itself can be applied to any semiconductor heterostructure provided the relevant material parameters are known.

---

[3] Material parameters include values for the band gap of the material $E_g(x)$ as a function of dopant concentration, also the effective masses for the electrons and heavy holes under the effective mass approximation.

4.2 Theory

We will consider first single particle energies - excitonic effects will be included later. The optimization procedure necessitates solving the one particle time independent Schrödinger equation. within the envelope-function approximation, for a system having an arbitrary shaped potential. To do this it is necessary to utilise a numerical method in order to obtain the energy levels and associated wavefunctions. In our calculations we employed the shooting technique [17], since this is a well established method for dealing with this type of problem. In this manner the ground state energies and envelope wavefunctions for the electron and heavy hole are obtained within the effective mass formalism. For the purposes of the calculation the following energy gap [18, 19, 20], effective masses [21, 18] and conduction band to valence band offset ratio [22] for $Cd_{1-x}Mn_xTe$ were used:

$$m_e^* = 0.096m_0.$$

$$m_{hh}^* = 0.53m_0.$$

$$E_g(x) = 1.606 + 1.587x \quad \text{eV}.$$

CB:VB offset ratio is 60:40.

The energy gap [23], effective masses [23, 3] and conduction band to valence band offset ratio [24]. relevant to a $Al_xGa_{1-x}As/GaAs$ heterostructure are:

$$m_e^* = 0.0665 + 0.0835x$$

$$m_{hh}^* = 0.34 + 0.42x$$

$$E_g(x) = \begin{cases} 1.424 + 1.247x \quad \text{eV} & 0 < x < 0.45 \\ 1.424 + 1.247x + 1.147(x - 0.45)^2 \quad \text{eV} & 0.45 < x < 1.0 \end{cases}$$

CB:VB offset ratio is 60:40.

The band structure of the QW system can be optimised using a technique described in Appendix A.1[4]. This technique maximises the quantum confined stark shift of the ground state electron and heavy hole transition energies, by 'shaping' the well region. Once the 'shape' of the well region has been optimised for either a red or blue shift, the one-particle energy shift can be calculated using the result

$$\Delta E_{shift} = (e_1^F + hh_1^F) - (e_1 + hh_1).$$

Where e_1^F, hh_1^F, e_1 and hh_1 are electron and heavy hole one particle energies, with and without the electric field. The oscillator strength, which is proportional to the square of the overlap integral, is then found by evaluating:

$$O.S = \left| \int_{-\infty}^{\infty} \Psi_e^*(z)\Psi_{hh}(z).dz \right|^2$$

---

[4] The full mathematical and computational analysis is outlined in Appendix A.1

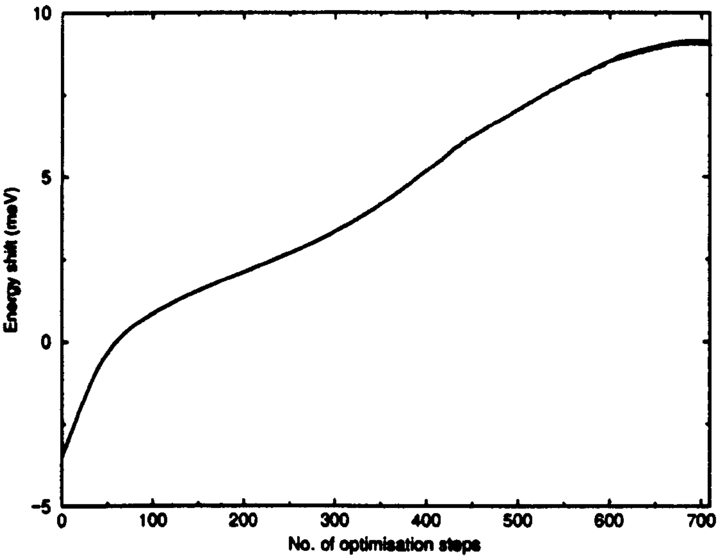

Figure 4.6: energy shift in the interband transition energy after each iterative step in the optimisation, at an applied field of 10 kV/cm for a CdMnTe/CdTe QW.

4.3 Results

Blue shift

4.3.1 CdTe system

The system considered comprised a 150Å $Cd_{0.8}Mn_{0.2}Te$ barrier with a 200Å CdTe well region and a 150Å $Cd_{0.8}Mn_{0.2}Te$ buffer layer. This system was optimised for a range of fields from 10 kV/cm to 40 kV/cm. When a field of 10 kV/cm was applied and the structure optimised, the energy shift altered after each iteration. Initially, since the structure is essentially symmetric, the energy shift is that of a standard QW structure i.e. red shifted. This is evident in Fig (4.6) where a red shift occurs for a low number of iteration steps. However as the optimisation process continues the energy shift of the structure increases and reaches a maxima at approximately 700 steps. Clearly at this point the structure has reached its optimum value for maximising the blue shift. This maximum in the curve occurs due to the physical constraints imposed upon the structure [5].

The optimised well structure, shown in Fig (4.7), produces a blue shift of 9.14 meV, when an electric field of 10 kV/cm is applied. This shift in the transition energy arises from the movement of the electrons once a field is applied. Fig (4.8) shows the shift in the electron and heavy hole positions in an applied field. On application of the latter the overlap between the electron and hole wavefunctions is increased significantly. This suggests that the essential physics of the process is to create a situation where initially, at zero bias, the electron and hole are well separated thus allowing an external field to reduce this separation. This is also seen to be the case for larger fields. For example Fig (4.9) shows the electron and hole wavefunctions for an optimised structure with and without an external field of 20 kV/cm. For this system we find the blue shift is slightly higher, at a value of 10.12 meV. Fig (4.10) shows the potential profile for this new optimised structure. An important point

---

[5] As discussed in the previous section, these constraints are necessary to ensure the barrier height or well height does not surpass that of the initial outer barriers.

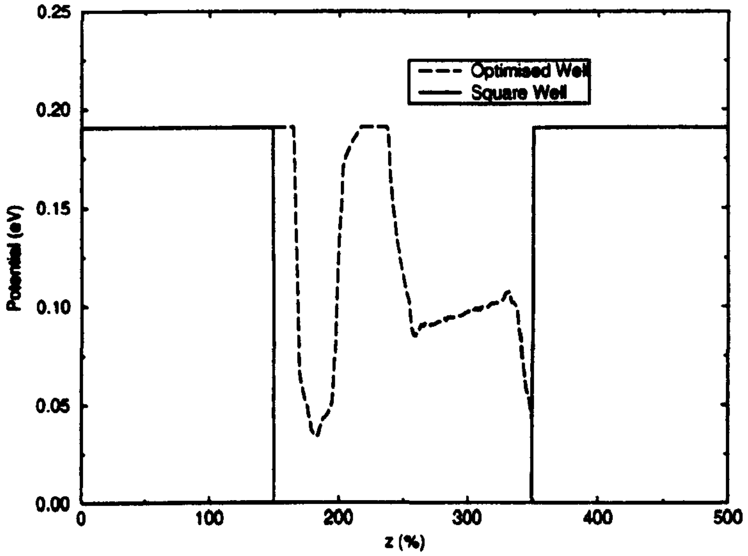

Figure 4.7: Potential profile of an optimised CdMnTe/CdTe QW structure for an applied field of 10 kV/cm.

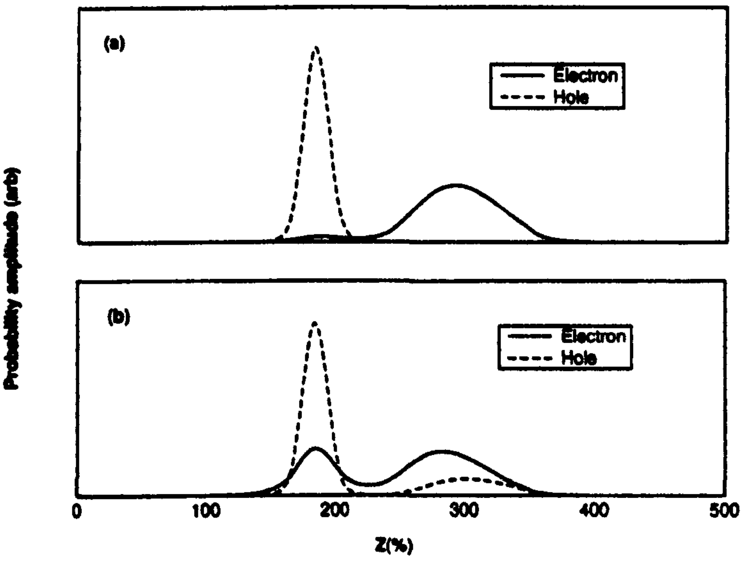

Figure 4.8: (a) Electron and heavy hole envelope wavefunctions for an optimised CdMnTe/CdTe QW without an external field; (b) Electron and heavy hole envelope wavefunctions for an optimised CdMnTe/CdTe QW with an external field of 10 kV/cm.

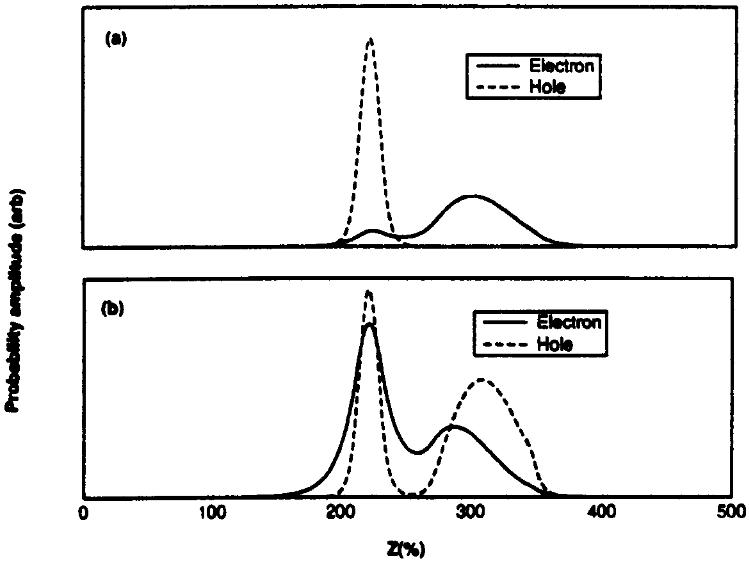

Figure 4.9: (a) Electron and heavy hole envelope wavefunctions for an optimised CdMnTe/CdTe QW without an external field; (b) Electron and heavy hole envelope wavefunctions for an optimised CdMnTe/CdTe QW with an external field of 20 kV/cm.

to note is that the optimised structure is different for different field strengths.

A very interesting effect can be seen to occur in both these optimised structures. It appears as if the left hand barrier has moved into the well region (i.e. the well has narrowed). This suggests that, in order to optimise the blue shift in such a structure, we will need to optimise the well width. If this optimum well width is narrower than the original well width then one side of the barrier will move into the well. The profiles also suggest that the optimum structure will be similar to a DQW where the second shallower well has a graded gap.

The structure can be optimised at different field strengths. Fig (4.11) shows the blue shifts of these optimised QW structures against an external electric field. For each point on the curve the original well has been fully optimised at a particular field, and the value of the maximum blue shift plotted. It is clear that the largest blue shift possible for this particular system is ~ 10 meV and occurs for a field ~ 20 kV/cm. For the QW structure under consideration the largest applied field employed is 35 kV/cm. This is because the hole escapes from the confines of the QW at higher field values. Put differently, for any optimised QW structure, bounded by the original shape of the unperturbed well, the maximum electric field that can be applied is 35 kV/cm, before the hole wavefunction escapes to the continuum. This maximum in the applied field would be increased for cases where the original well was deeper. For such a situation the maximum blue shift possible would also be greater. The depth of the well is governed by the Mn concentration in the barrier regions. Although this is easily increased when modelling such a structure theoretically, very high dopant concentrations of Mn in the barriers are not readily attainable experimentally.

4.3.2 GaAs system

There has been much interest in $Al_xGa_{1-x}As/GaAs$ QW structures, and the properties and technology governing these III-V semiconductor are well known. In particular the possibilities of high dopant concentration of the Al ions leading to deeper wells is readily achievable. For this reason, and also because it permits a comparison with the results of

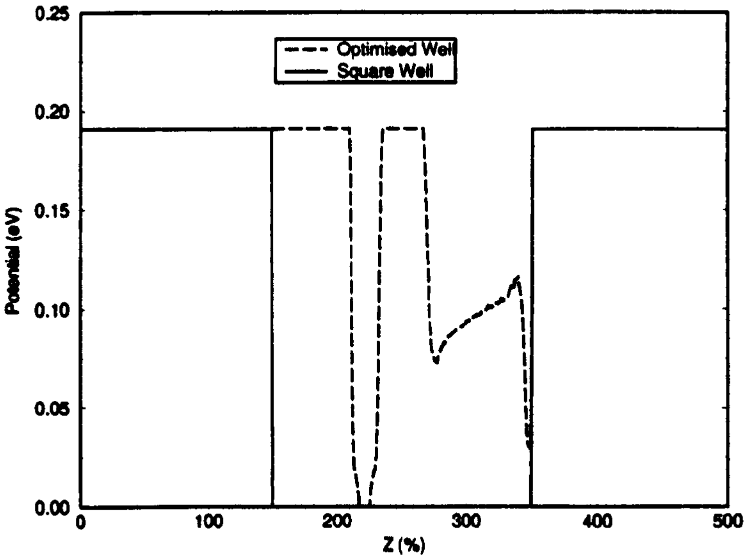

Figure 4.10: Potential profile of an optimised CdMnTe/CdTe QW structure for an applied field of 10 kV/cm.

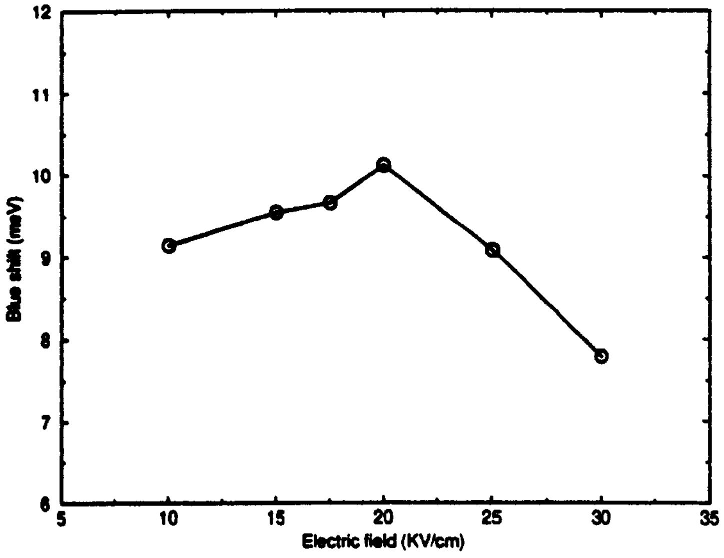

Figure 4.11: Blue shifts as a function of electric field for an optimised CdMnTe/CdTe QW structure at each field value.

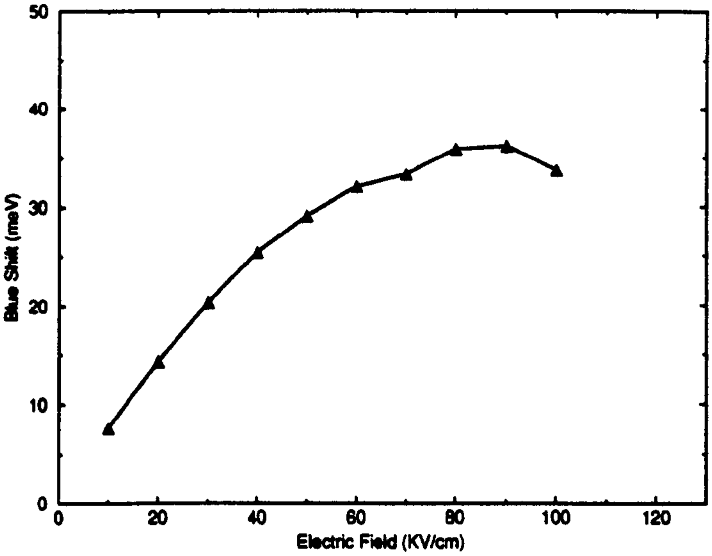

Figure 4.12: Blue shifts as a function of electric field for an optimised AlGaAs/GaAs QW structure at each field value.

other authors, this system was also optimised.

A QW system comparable to that described by *Susa* and *Nakahara* [15] was initially chosen. This comprised a 95Å $Al_{0.73}Ga_{0.27}As$ cap and buffer layers, with a 100Å GaAs well region. This symmetric unperturbed well was optimised for a range of fields. Since the concentration of Al ions in the barriers could be increased appreciably thus increasing the depth of the well, the applied electric fields could range over much greater values compared with those of the previous system. This is shown in Fig (4.12), which shows the maximum blue shifts of the optimised QW structures against an external electric field [6]. Once again there is a maximum in the value of the blue shift that is possible and this occurs at a field strength ~ 90 kV/cm.

The blue shift values for this system are very large when compared with the CdTe system. The shifts range from 7.66 meV at low fields (10 kV/cm) to a maximum of 36.27 meV at high fields (90 kV/cm). On examination of the optimised structure for the 90 kV/cm case (see Fig (4.13)) we see that, unlike the CdTe system, the barrier regions have not moved into the well. This suggests that the present unperturbed QW has not the optimum width initially. To obtain the latter and thus deduce the truly optimised QW structure it is necessary to start with a wider QW structure.

We therefore chose a second QW system in which the initial unperturbed QW comprised 45Å $Al_{0.73}Ga_{0.27}As$ barriers together with a 200Å well region. This structure was then optimised for a range of fields (10 kV/cm - 110 kV/cm). As expected the blue shifts were higher than before, and the barriers were found to move into the well region, thus enabling us to define the optimised QW width.

The maximum blue shift occurs for a field of 90 kV/cm and the resulting structure is shown in Fig (4.14). The movement of the left hand barrier into the well region can be seen clearly, thus confirming that this is the optimum shape of the QW producing the maximum blue shift that is possible. When a field of 90 kV/cm is applied to this structure the transition energy is found to be blue shifted by 43.67 meV. The structures were optimised for electric

---

[6] Each point represents a different QW structure which has been optimised for that particular electric field.

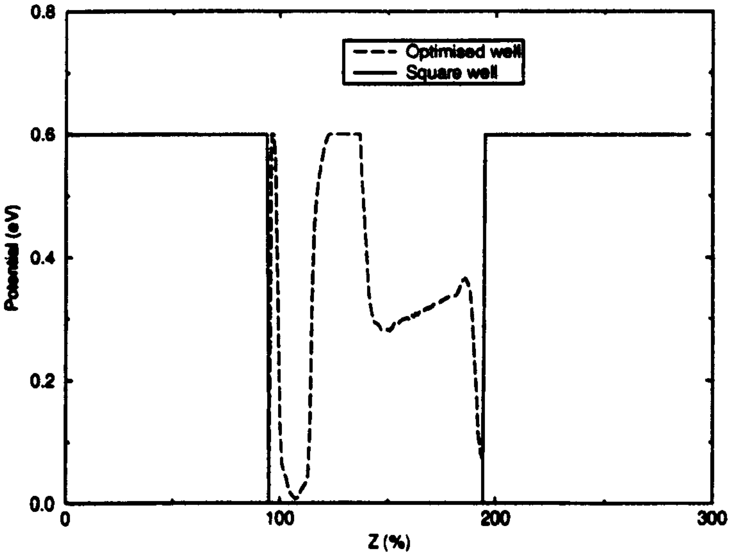

Figure 4.13: Potential profile of an optimised AlGaAs/GaAs QW structure for an applied field of 90 kV/cm (original well width = 100Å)

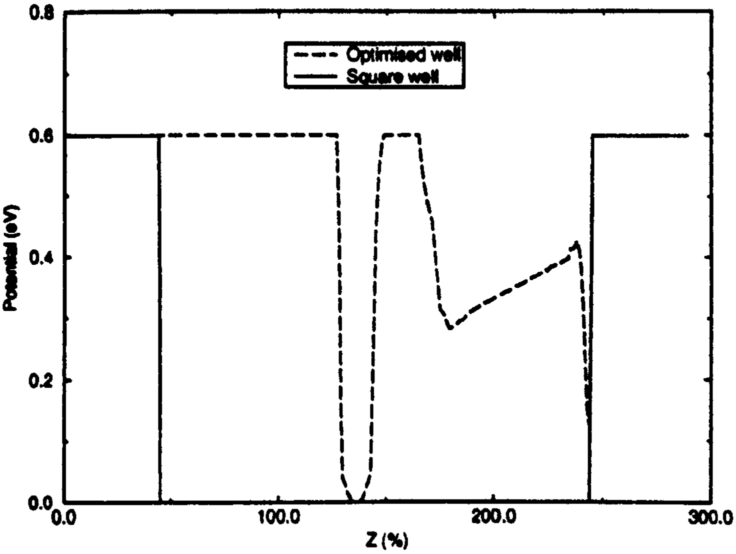

Figure 4.14: Potential profile of an optimised AlGaAs/GaAs QW structure for an applied field of 90 kV/cm (original well width = 200Å)

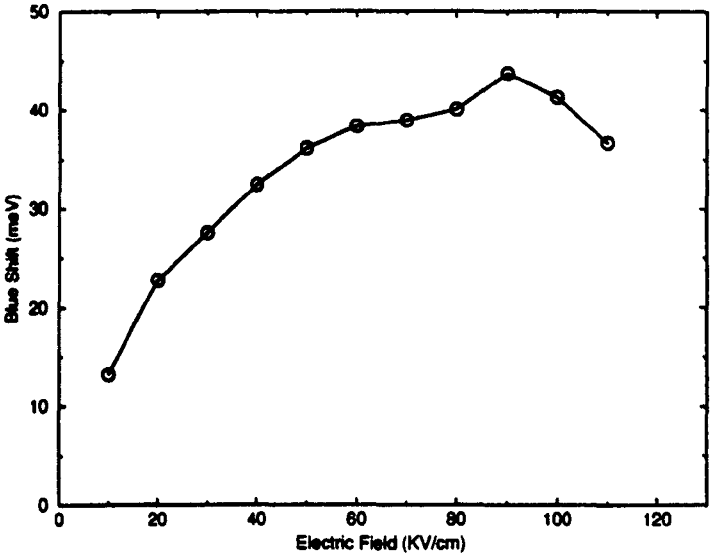

Figure 4.15: Blue shifts as a function of electric field for an optimised (wider) AlGaAs/GaAs QW structure at each field value.

fields applied in particular directions (left to right). If the field direction was reversed the blue shift of the transition energies would not be present. Thus for the optimised structure shown in Fig (4.14) on reversal of the field a red shift of 59.84 meV is obtained.

As noted earlier when the maximised blue shifts for a given external electric field are plotted against this field, as in Fig (4.15), it can be seen that the blue shifts increase to a maximum as the field strength increase, and then decrease again. This again confirms that for a AlGaAs/GaAs QW whose barriers have been fixed, there is an optimum structure with an optimum electric field which gives rise to the maximum blue shift possible for that QW structure. The optimised QW structure, corresponding to the maximum in the blue shift in Fig (4.15), has the form shown in Fig (4.14).

Such a structure, as well as all the others described in this section, are ones that have been mathematically optimised. However the precise technology needed to grow such structures does not presently exist. Technology such as MBE and MOVPE allow very precise control of the growth, and on digitisation of the above optimised structures, these structures could be realized experimentally. Since the structures have been precisely optimised, this digitisation process could, in principle, affect the value of the blue shift significantly. However we have shown that digitisation close to the optimised structure can occur without a significant change in the blue shifts [25]. In order to illustrate this point, as well as drawing attention to some of the subtleties involved, the optimised structure shown in Fig (4.14) was digitised so that, using one of the afore mentioned growth techniques the structure becomes realisable. The structure was first partially digitised by replacing the graded gap region in the second well by a flat potential. One choice for the latter is that it begins at the base of the slope and extends to the barrier region, as shown in Fig (4.16). Such a choice reduces the blue shift significantly from 43.67 meV to 15.19 meV. As this flat potential region is moved to higher energies, the reduction in the blue shift increases to the extent that when it reaches the top of the sloped region (see Fig (4.17)) the blue shift is reduced to 1.54 meV. From these examples it is clear that in order to maintain a large blue shift, the wider QW must have a graded gap even after digitisation, since a flat (i.e. a square well) reduces the blue shift dramatically.

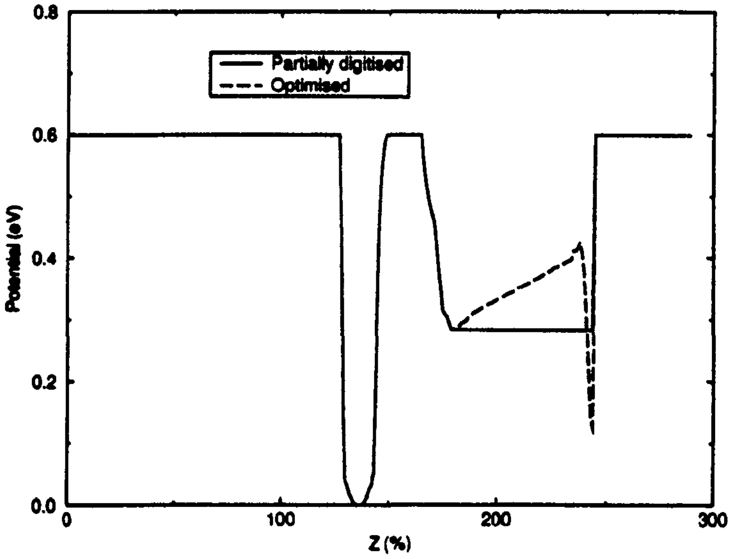

Figure 4.16: Conduction band profile of a partially digitised, optimised $Al_xGa_{1-x}As/GaAs$ AQW structure.

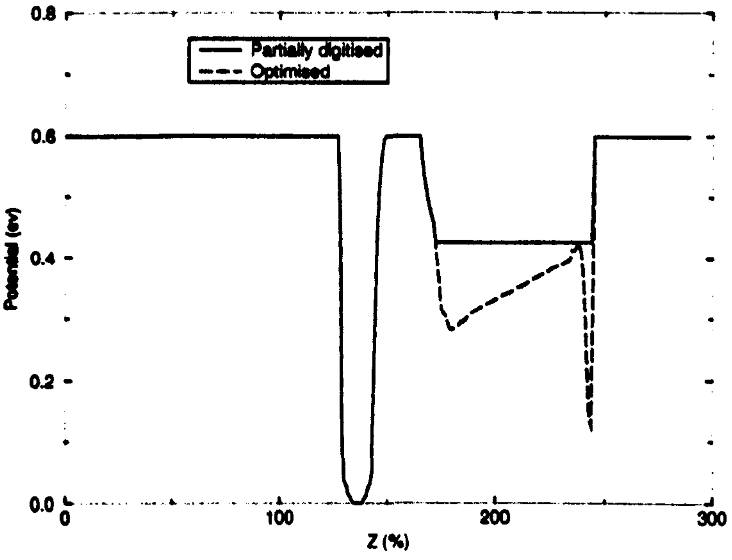

Figure 4.17: Conduction band profile of a partially digitised, optimised $Al_xGa_{1-x}As/GaAs$ AQW structure.

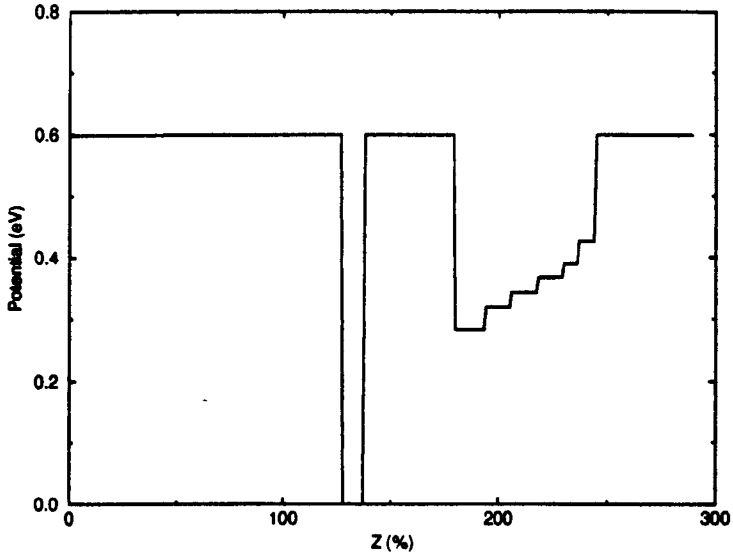

Figure 4.18: Conduction band profile of a digitised three step $Al_xGa_{1-x}As/GaAs$ AQW structure.

When the structure is digitised[7], it can be grown experimentally. Fig (4.18) shows one such digitised structure. Here the first well has been chosen deliberately to be so narrow (~9 Å) that it cannot confine the hole even in the absence of a field. As a result the electron and the hole spend an appreciable time in the graded well region both before, and after, the application of the electric field, and the blue-shift is tiny (~0.32meV). If, however, the digitisation is chosen to be closer to the shape of the optimised structure, then the the resulting blue shift can be increased significantly. To illustrate this Fig (4.19) shows another structure, where the digitisation follows more closely that of the optimised shape. The structure now comprises a narrow 14Å GaAs well, a 28Å stepped layer and a 70Å graded well. Application of a 90kV/cm electric field gives a blue-shift of 30.7meV. Thus the optimised structures can be digitised, and as long as the latter follow closely those of the optimised structure, the blue shifts will still be very large. However, as shown, even a slight variation in the digitised structure can result in a huge variation in the blue shift. This suggests that the chances of obtaining blue shifts that are anywhere near the maximum values possible are small, based on trial and error experimental growth runs.

An important and related consideration for the device engineer, is the overlap of the carrier wavefunctions. The associated oscillator strength is proportional to the square of the overlap integral of the n=1 electron (1e) and the n=1 heavy hole (1hh) envelope wavefunctions. As mentioned earlier a blue shift is attained when the external electric field acts to reduce the separation between electron and hole. Fig (4.20) shows a digitised QW structure which comprises $Al_{0.73}Ga_{0.27}As$ outer barriers, a narrow (20Å) GaAs well, a 17Å thick $Al_{0.73}Ga_{0.27}As$ inner barrier followed by a 78Å graded well (steps for the graded region are: 26Å with x=38%; 12Å with x=43%; 12Å with x=46%; 12Å with x=49%; 8Å with x=52% and 8Å with x=56%.). For this case application of an electric field of 90kV/cm, gives a blue-shift of 13.15meV. It can also be seen that there is a reduction in the spatial separation of the electron and the hole on application of the field. Table (4.1) shows the values of the square of the overlap integral between the 1e and 1hh envelope wavefunctions for a few

---

[7] From the previous argument, all digitised systems considered, will have a graded potential in the wider QW

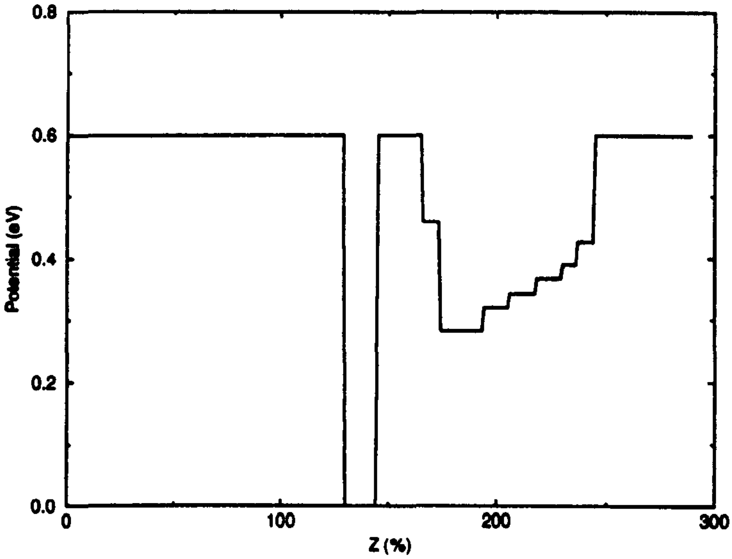

Figure 4.19: Conduction band profile of a accurately digitised, optimised $Al_xGa_{1-x}As$/GaAs AQW structure.

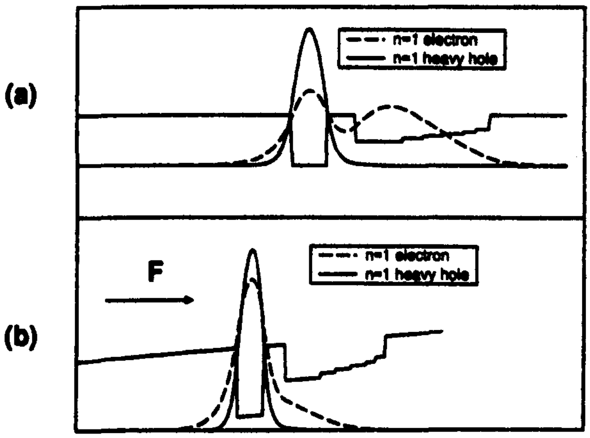

Figure 4.20: (a) CB profile and envelope wavefunctions of a modified three step $Al_xGa_{1-x}As$/GaAs QW with no external field, where the second QW is graded such that the graded steps are given by 26Å, x=38%; 12Å, x=43%; 12Å, x=46%; 12Å x=49%; 8Å, x=52% and 8Å, x=56%.(b) CB profile and envelope wavefunctions for the same modified three step $Al_xGa_{1-x}As$/GaAs QW with an external field of 90kV/cm.

Figure number	Value of square overlap integral (1e and 1hh)		Blue shift (meV)
	Without electric field	With 90kV/cm electric field	
4.18	0.93	0.95	0.32
4.19	0.12	0.83	30.7
4.20	0.41	0.82	13.15

Table 4.1: Table showing the values of the square of the overlap integral between the electron and heavy hole envelope wavefunctions for the systems described, this being proportional to the oscillator strength of these structures.

of the systems described earlier (this being proportional to the oscillator strength of these structures).

These results confirm clearly the connection between blue shifts and increased values of the oscillator strength.

Red shift

Optimisation of the red shift is achieved by solving the same problem outlined in the previous section (see Appendix A.1), only now the inequality is reversed (see equation A.12). The system considered is a $Al_xGa_{1-x}As/GaAs$ QW system, since this allows comparison with results available in the literature. Using the same material parameters as before, the red shift can be maximised for a range of systems.

A red shift in the spectrum occurs on application of an external field to a RQW. This is illustrated for a 200Å GaAs QW with $Al_{0.73}Ga_{0.23}As$ barriers in Fig (4.21) which shows the effect on the 1e and 1hh envelope wavefunctions when a field of 80kV/cm is applied. The corresponding one-particle energy difference is seen to red shift by ~ 61 meV. It is also noticeable that on application of the electric field the wavefunctions separate, as opposed to the blue shift case where the spatial separation is reduced, (i.e the overlap of the wavefunctions is increased).

Taking the 200Å GaAs QW system and optimising the red shift at an external field of 80kV/cm, shows the red shift is maximised by increasing the spatial separation of the electron and the hole. This is shown in Fig (4.22), where it can be seen that the maximum red shift is achieved after approximately 2000 steps. The corresponding optimised structure and associated envelope wavefunctions are shown in Fig (4.23). It is clear from the latter that the optimum structure corresponds to two widely separated QW's i.e an ADQW like structure. For this situation the 1e and 1hh probability distributions are virtually identical both before and after the application of the external electric field i.e the electron and hole are essentially confined in their respective wells. The red shift from such a system with an external field of 80kV/cm is ~153 meV, which is more than twice that of the 200Å RQW and close to the maximum potential drop (i.e 160 meV) across the 200Å 'well' region. Unfortunately this type of system would be of little practical use, due to the negligible overlap of the 1e and 1hh wavefunctions and consequently a very low associated oscillator strength.

To be a device possibility it is essential to increase the overlap of the wavefunctions, thus increasing the oscillator strength. This means a narrower QW system must be chosen as the starting point for the iteration procedure. The new system was chosen so that a comparison with experimental results described in the literature could be made. Initially, as a partial check on the parameter base and offset ratio chosen, we will evaluate first the red shift in the two structures investigated by Morita et al [26] via photo-current spectroscopy. The first

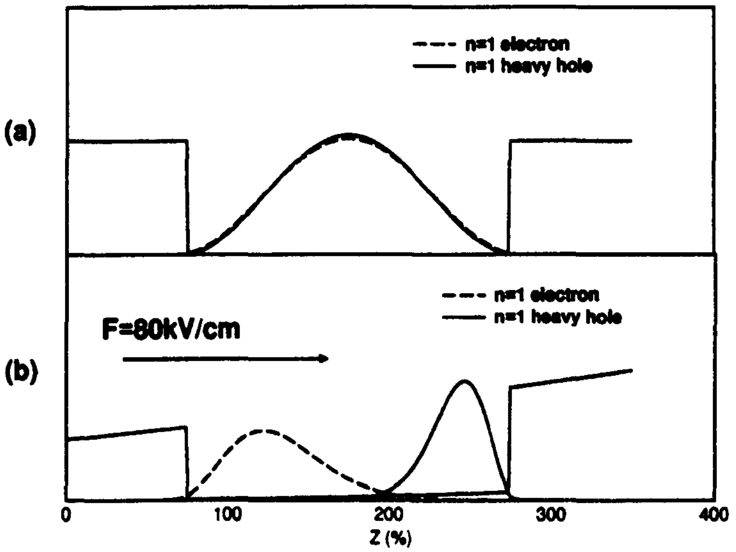

Figure 4.21: Band diagram and envelope wavefunctions for a RQW with (a) 0 V/cm, (b) 80 kV/cm external electric field applied.

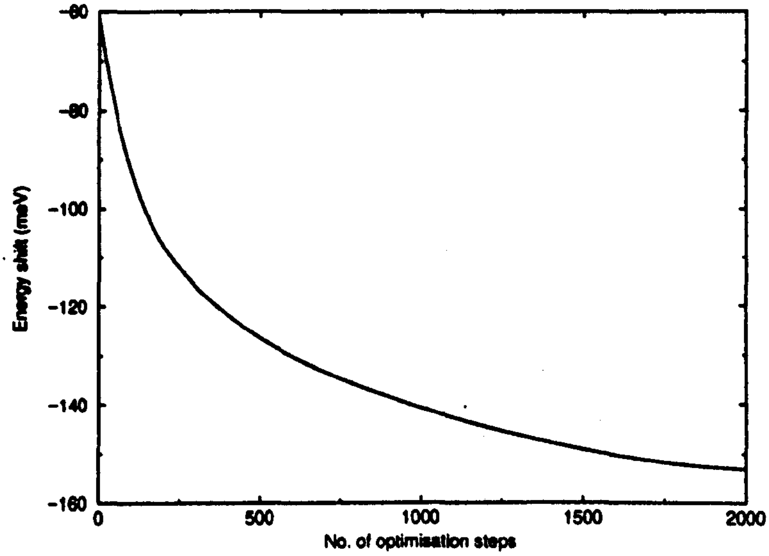

Figure 4.22: Energy shift in the interband transition energy after each iterative step in the optimisation, at an applied field of 80kV/cm for a $Al_xGa_{1-x}As/GaAs$ QW.

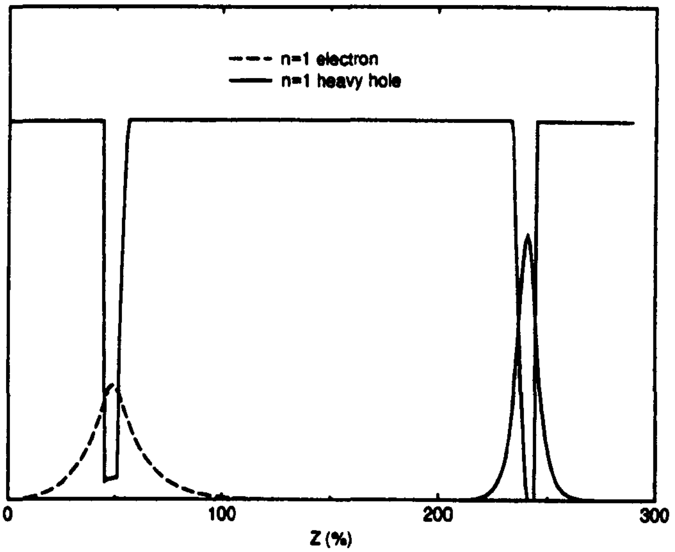

Figure 4.23: Potential profile of an optimised $Al_xGa_{1-x}As/GaAs$ QW structure for an applied field of 80kV/cm.

structure was a 100Å RQW in the $Al_{0.4}Ga_{0.6}As/GaAs$ system. The observed red shift for a field of 100kV/cm was ~18 meV [26]. This is in excellent agreement with our calculated value of 18 meV.

The second structure considered by Morita et al [26] comprised a stepped QW, i.e. the outer barrier of $Al_{0.4}Ga_{0.6}As$ was followed by 30 Å of GaAs after which there was 70 Å of $Al_{0.1}Ga_{0.9}As$ and then the outer barrier of $Al_{0.4}Ga_{0.6}As$ again. For this structure the red shift in the same external field of 100kV/cm was observed to increase significantly to 48 meV [26]. Ignoring excitonic effects we obtained a theoretical value of 48.5 meV for the quantum confined stark shift. This good agreement between the calculated and observed values for the red shift serves to strengthen our confidence in both the parameter and offset ratios we employed. We will consider next applying the optimization-digitization process to the original 100Å RQW of Morita et al [26] described above. The resulting structure is shown in Fig (4.24) and because it is double-quantum well like, will be referred to as an optimised AQW structure. It comprises a $Al_{0.4}Ga_{0.6}As$ barrier followed by a $Al_{0.15}Ga_{0.85}As$ QW of width 16Å, after which there is a 14Å stepped barrier region of $Al_{0.34}Ga_{0.66}As$. This is followed by a 52Å $Al_{0.4}Ga_{0.6}As$ barrier, an 18Å $Al_{0.15}Ga_{0.85}As$ QW and finally a $Al_{0.4}Ga_{0.6}As$ buffer.

The resulting one-electron energy shifts in an external field for the 1e-1hh interband transition (i.e. ignoring excitonic effects) are shown in Fig (4.25). The solid line represents the shift for the optimized AQW, whereas the dashed line represents the 100Å RQW. It can be seen clearly that utilizing the AQW structure leads to an enhanced QCSE for all values of the applied field. The corresponding one electron energy changes of the electron and hole for the AQW structure in a positive field are shown in Fig (4.26). For the optimized AQW structure at a field of 100kV/cm, the one-electron energy shift is 82 meV this being a factor of 4 greater than the shift in the RQW and 30 meV greater than the shift in the simple stepped structure of Morita et al [26].

A related consideration is the overlap of the carrier wavefunctions. Fig (4.27) shows the one electron 1e,1hh (uncorrelated) probability distributions with and without the field for the AQW. From these distributions, it is clear that, prior to the application of a field , the

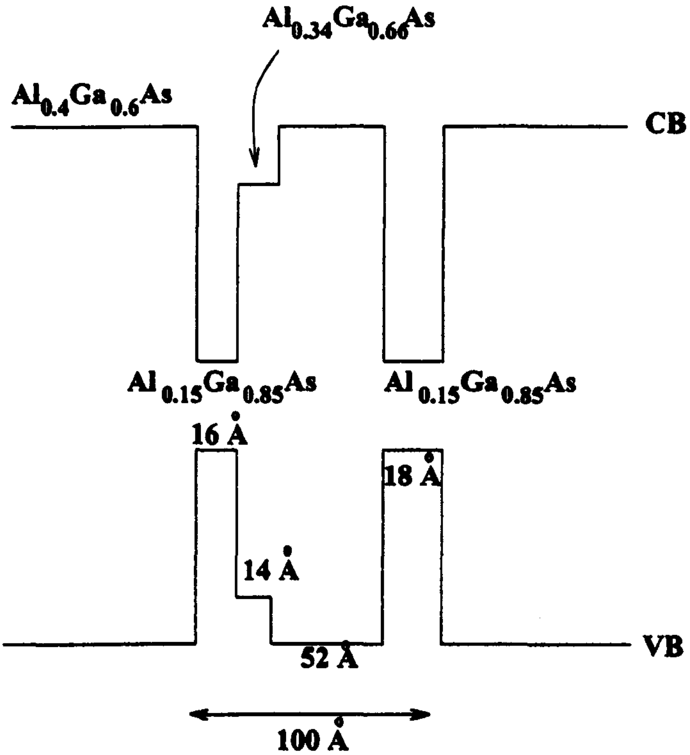

Figure 4.24: Schematic band diagram of an $Al_xGa_{1-x}As$/GaAs asymmetric double quantum well system.

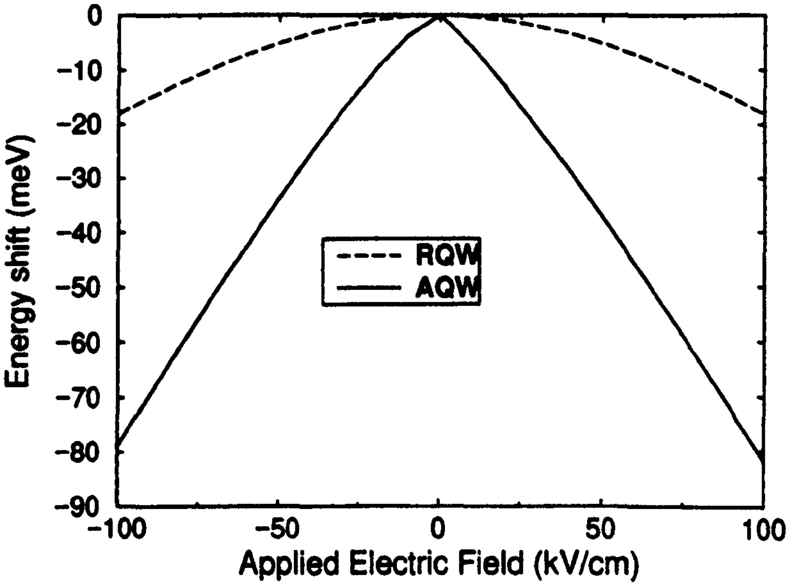

Figure 4.25: Energy shift of the 1e-1hh exciton transition energy, for a range of applied electric fields for the AQW and the RQW system.

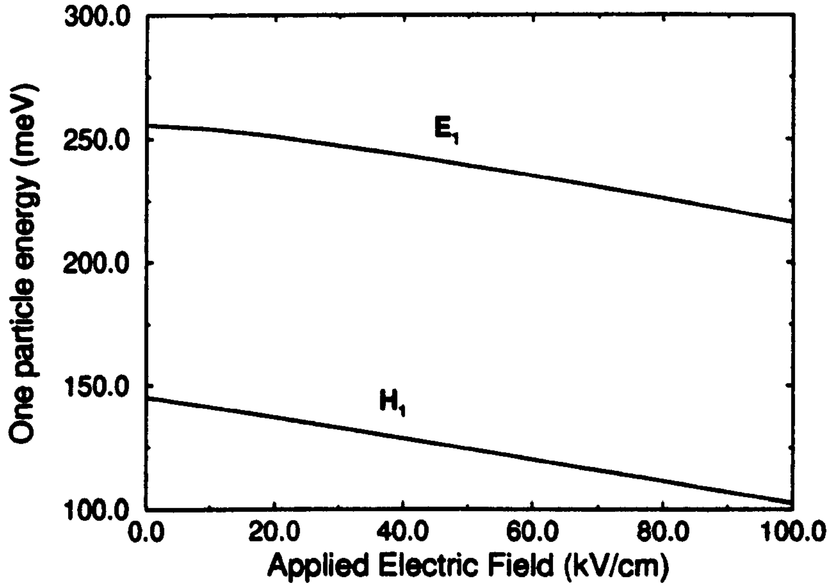

Figure 4.26: One particle energies shifts for the conduction band electron/valence band hole, as a function of the applied field.

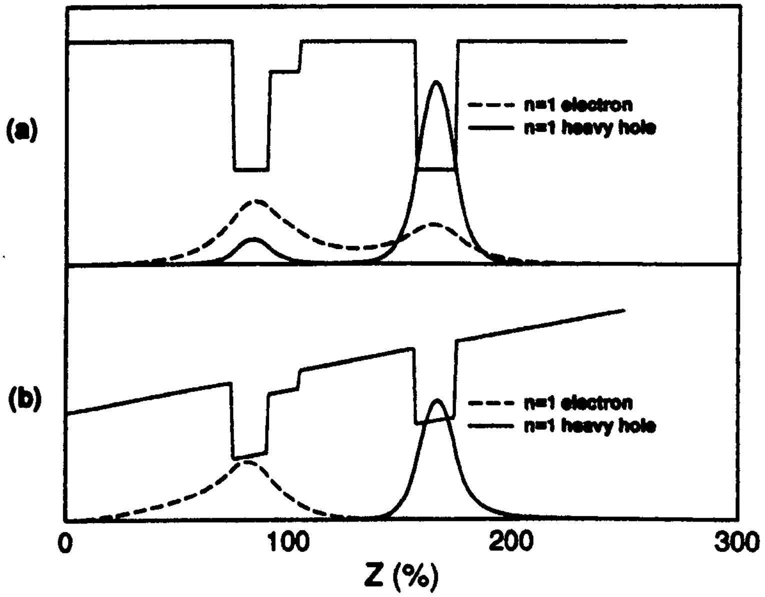

Figure 4.27: (a) Envelope wavefunctions for the AQW without an applied field, (b) Envelope wavefunctions for the AQW with an external field of 100kV/cm applied.

(uncorrelated) 1e and 1hh are not fully localised in either QW, and that on application of a field of 100kV/cm the (uncorrelated) 1e and 1hh are confined in separate QW's, with the overlap of their wavefunctions being reduced significantly. In a RQW the electron and hole are pulled to the opposite ends of the well region on application of an electric field. It is clear therefore that the essential physics contained in the optimization-digitization procedure, is to maximize the spatial distance of separation of the electron and hole for a given value of the external field. It is important to realise therefore (as explicit calculation readily verifies) that the optimized structure required to maximize the red shift varies with the applied field under consideration. This same line of reasoning enables us to understand the influence of excitonic effects, which will be discussed next.

4.3.3 Excitonic effects

The results reported in this chapter have so far been concerned with one electron energy shifts, i.e excitonic effects have been ignored. To incorporate excitonic effects into the calculation, one must employ trial wavefunctions for the relative motion of the electron and hole and invoke the variational principle as a criterion for obtaining the 'best' estimate of the binding energy of the exciton [27, 28, 29] (see Chapter 1). In terms of experimental observation of the QCSE, it is the excitonic energy shifts that are of interest. For this reason the excitonic energy shifts for the structures described above were calculated. For the 200Å $Al_{0.73}Ga_{0.27}As$ RQW , prior to optimisation, excitonic effects reduce the red shift by 3.8 meV on application of a 90kV/cm electric field i.e the red shift decreases from 61 meV to 57.2 meV. Starting from the same 200Å RQW and optimising the structure to produce a maximum blue shift (see Fig (4.14, it is found that excitonic effects reduce the blue shift by ~3 meV on application of a 90kV/cm electric field i.e the blue shift decreases from 43.6 meV to 40.6 meV.

In addition to the energy changes, the formation of an exciton in the type I structures described. also has an effect on the oscillator strength of the 1e-1hh transition. Fig (4.28) shows the change in the square of the overlap integral (which is proportional to the oscillator strength) with the applied electric field in the ADQW and the RQW, either ignoring or including excitonic effects. It is clear from this figure that, in general, the square of the overlap integral for the ADQW is always less than that of the RQW, and that it decreases much more rapidly with the field. However it can also be seen that the trends in the curves are not altered by the inclusion of excitonic effects, i.e the essential physics remains unchanged by their inclusion.

In summary, the calculations show that the inclusion of excitonic effects reduces the stark shift by a few meV only. Since this is an order of magnitude less than the overall shift, such terms can be neglected without introducing any significant error in the end result given by the one-electron energy changes. Similarly although inclusion of excitonic effects does influence the oscillator strength, the essential physics and general trends remain basically unaltered. Thus for simplicity, and without great loss in accuracy the shift in the absorption spectra of such systems can be analysed using one electron energy shifts.

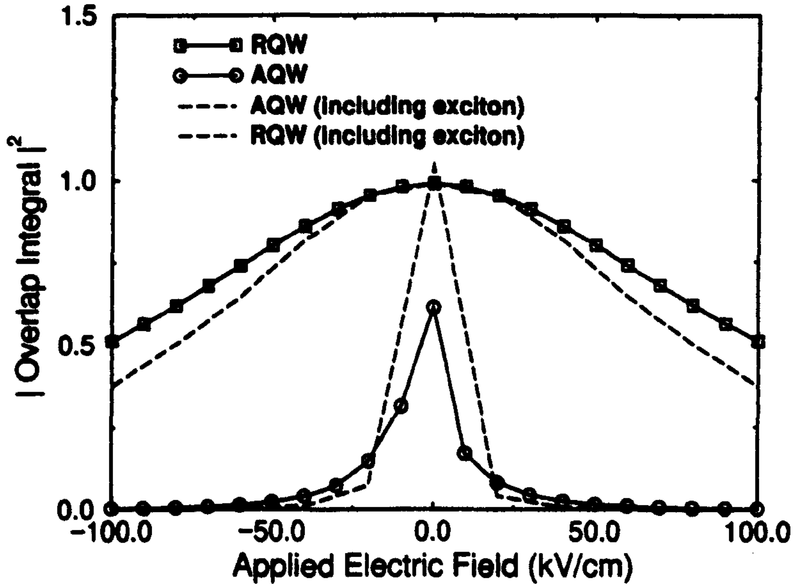

Figure 4.28: Square of the overlap integral for the n=1 electron and the n=1 heavy hole, as a function of applied electric fields for both the AQW and the RQW systems, either including (or excluding) excitonic effects.

4.4 Conclusion

The present results show that by applying an optimisation technique to an initially symmetric QW, an asymmetric QW like structure can be obtained which, under the application of an external electric field, gives rise to appreciable stark shifts in the excitonic absorption peaks. The technique described can optimise a given QW for a chosen value of the electric field, in such a way that the resulting structure gives the maximum possible blue/red shift. In short, the present work shows that the blue/red shift of a given material system (e.g CdMnTe/CdTe or AlGaAs/GaAs) has a maximum value corresponding to some optimised structure, and that the blue/red shift of a given QW shape has a maximum at some particular value of the electric field.

The stark shifts of $Al_{0.73}Ga_{0.27}As$/GaAs QW's have been calculated and maximum stark shifts of ~43 meV (blue) and 153 meV (red) for a nominal 200Å GaAs well have been reported. For the same nominal well width the maximum blue shift observed in a $Cd_{0.8}Mn_{0.2}Te$/CdTe QW was, by comparison, only ~10 meV. With such large shifts these types of structures allow the development of quantum confined stark shifted devices such as S.E.E.Ds, asymmetric modulators and photodetectors . The results show also the need for evaluating theoretically the optimised QW shapes, since digitised structures that are quite close to the optimum shape can have small stark shifts, i.e. the stark shift can be a relatively sensitive function of the QW potential profile.

Bibliography

[1] W. Franz. Z.Naturforch. **13a**,484 (1958).

[2] L. V. Keldysh. Zh.Eksp.Teor.Fiz. **34**,1138 (1958) [Sov.Phys.- **JETP 7**,788 (1958)].

[3] D. A. B. Miller, D. S. Chemla, T. C. Damen, A. C. Gossard, W. Wiegmann, T. H. Wood and C. A. Burrus. Phys.Rev.B., **32**,1043 (1985).

[4] J. Stark, Preuss. Akad. Berlin, **40**,932 (1913).

[5] D. A. B. Miller, D. S. Chemla, T. C. Damen, T. H. Wood T.H, C. A. Burrus, A. C. Gossard and W. Wiegmann. IEEE, **QE-21**,1462 (1985).

[6] D. A. B. Miller, D. S. Chemla, T. C. Damen, A. C. Gossard, W. Wiegmann, T. H. Wood and C. A. Burrus. Phys.Rev.Lett., **53**,2173 (1984).

[7] W. Chen and T. G. Andersson. Semicond.Sci.Technol, **7**,828 (1992).

[8] H. Iwamura, T. Saku and H. Okamoto. Jpn.J.Appl.Phys., **24**,104 (1985).

[9] K. Wakita, Y. Kawamura, Y. Yoshikuri and H. Asahi. Electron.Lett., **21**,338 (1985).

[10] D. A. B. Miller, D. S. Chemla, T. C. Damen, A. C. Gossard, W. Weigmann, T. H. Wood and C. A. Burrus. Appl.Phys.Lett., **45**,13 (1984).

[11] T. H. Wood, C. A. Burrus, A. H. Guanck, J. M. Wiesenfelf, D. A. B. Miller, D. S. Chemla and T. C. Damen. Appl.Phys.Lett. **47**,190 (1985).

[12] D. A. B. Miller. Appl.Phys.Lett., **54**,202 (1989).

[13] K. W. Goossen, E. A. Caridi, T. Y. Chang, J. B. Stark and D. A. B. Miller. Appl,Phys.Lett. **56**,715 (1990).

[14] K. K. Law , R. H. Yan, J. L. Merz and L. A. Coldren. Appl.Phys.Lett., **56**,1886 (1990).

[15] N. Susa and T. Nakahara. Electron.Lett., **28**,941 (1992).

[16] P. Steinmann, B. Barchert and B. Stegmüller. IEEE. Photon.Technol.Lett., **9**,191 (1997).

[17] J.P. Killingbeck, "Microcomputer Algorithms", (Hilger,Bristol,1992).

[18] C. H. Neumann, A. Nöthe and N. O. Lipari. Phys.Rev.B., **37**,922 (1988).

[19] S. K. Chang, A. V. Nurmikko, J. W. Wu, L. A. Kolodziejski and R. L. Gunshar. Phys.Rev.B., **37**,1191 (1988).

[20] A. Twardowski, M. Nawrocki, J. Ginter. Phys.Stat.Sol.(b), **96**,497 (1979).

[21] P. Lawaetz. Phys.Rev.B., **4**,3460 (1971).

[22] D. L. Camhausen, G. A. N. Connel, W. Paul. Phys.Rev.Lett., **26**,184 (1971).

[23] T. Hiroshima and K. Nishi, J.Appl.Phys,**62**,3360 (1987).

[24] D. S. Chemla. D. A. B. Miller, P. W. Smith, A. C. Gossard and W. Wiegmann. J.Quantum Electron., **QE-20**,265 (1984).

[25] R. K. Gug and W. E. Hagston. Appl.Phys.Lett.**73**,1547 (1998).

[26] M. Morita, K. Goto and T.Suzuki, Jpn.J.Appl.Phys. **29**,L1663 (1990).

[27] C.P. Hilton, W.E. Hagston and J.E. Nicholls, J.Phys.A. **25**,2395 (1992).

[28] P. Hilton, T. goodwin., P.Harrison and W.E.Hagston, J.Phys.A., **25**,5365 (1992).

[29] P. Harrison, T. Piorek, W.E. Hagston and T. Stirner, Superlattices and Microstructures, **20**,45 (1996).

Chapter 5

Enhanced tunability in infrared photodetectors through optimisation of the quantum-confined stark effect.

5.1 Introduction

Over the last decade there has been extensive research into the QCSE of low dimensional semiconductors [1, 2, 3, 4]. This interest has stemmed from the optoelectronic device opportunities in structures where shifts of the inter-band excitonic transition lines are large in external electric fields [5, 6, 7, 8, 9, 10, 11]. Another aspect of the strong field dependence of the optical properties. concerns the potential application of a QW as a far infrared photodetector. Ever since the first direct observation of an intersubband transition within the conduction band of a GaAs QW by West and Eglash [12], progress into the realisation of novel devices based on these transitions has continued apace. In fact QW structures based on inter subband absorption have been proposed to replace the conventional HgCdTe photodetector [13, 14, 15]. Amongst the possible semiconductor heterostructures, modulation-doped AlGaAs/GaAs multiquantum wells have been studied experimentally since such systems have very large sharp optical absorption resonances between the ground state and the first excited state [16, 17]. The occurrence of these properties means that applications such as high contrast ratio optical modulators [13, 14] and voltage-controllable non linear optical devices [18, 19] become realisable.

Currently, there is wide interest in the development of sensitive tunable infrared photodetectors. The optical properties of a rectangular quantum well (RQW) have been studied in detail. However the stark shift of the intersubband transition for such a system is small, and hence a RQW is impractical for use as a tunable detector [20, 21]. From the device point of view, it is desirable to have QW structures with a large stark shift under a low driving voltage as well as a high oscillator strength contrast ratio i.e the change in oscillator strength with the field on of the n=1 to n=2 electronic transition. The main area of interest lies in the development of asymmetric coupled QW's (ACQW's) which enhance the stark effect of the intersubband transitions thus allowing tunability to be achieved. By the use of ACQW's. electrons in each well can interact strongly with each other thus leading to a large stark tuning effect. Studies into the enhanced stark shifts of AlGaAs/GaAs ACQW's have been made [13. 14. 15]. and tunability increased substantially over that occurring in a RQW. In the present chapter we consider an $Al_xGa_{1-x}As/GaAs$ QW system and describe the results of an optimisation routine, which starts from a given RQW structure and modifies the band-gap in the 'well' region so as to a maximise the energy shifts (n=1 to n=2 electronic transition) associated with the QCSE for a given electric field strength. Consideration of the most important features for the application of such systems, leads us to design a system that can satisfy the need for good tunability and high oscillator strength contrast ratio. Through comparison with the ACQW system described by Huang et al [13], we show that the optimisation procedure enables the range of tunability for a specific applied electric field range to be increased significantly. Since for certain device applications it is advantageous to have a high contrast ratio for differing electric fields, we examine the question of optimising the contrast ratio. Finally we will consider the effects of doping, and how the latter affects these particular properties of the system.

5.2 Theory

We consider an undoped QW system. To solve the one particle time independent Schrödinger equation for such a system within the effective mass formalism, we employ the shooting technique [22]. Using the latter the ground state energies and envelope wavefunctions for the electron are obtained. For the purposes of the calculation the following energy gap [2] and effective masses [2, 10] for $Al_xGa_{1-x}As$ were used:

$$E_g(x) = \begin{cases} 1.424 + 1.247x \ \text{ eV} & 0 < x < 0.45 \\ 1.424 + 1.247x + 1.147(x - 0.45)^2 \ \text{ eV} & 0.45 < x < 1.0 \end{cases}$$

$$m_e^* = 0.0665 + 0.0835x$$

It was also assumed that the conduction to valence band offset ratio was 60:40.

Since the oscillator strength is proportional to the square of the dipole matrix element for the transition, evaluation of this term shows the change in the oscillator strength. The dipole matrix element for the n=1 to n=2 electron transition, M_{12} is given by:

$$M_{12} = \int_{-\infty}^{\infty} \Psi_2^*(z)\frac{\delta}{\delta z}\Psi_1(z).dz \ ,$$

which can be shown to be equivalent to [23],

$$M_{12} = \int_{-\infty}^{\infty} \Psi_2^*(z)z\Psi_1(z).dz$$

(where we have ignored an energy separation term and some constant factors).

Although the latter form is often employed widely in the literature we will utilize the former expression since it is formally exact. Thus by the use of the shooting technique and the evaluation of the square of the dipole matrix element $|M_{12}|^2$, the eigen energies, envelope wavefunctions and relative change in oscillator strength can be calculated.

The band structure of the QW can be optimised by employing the optimisation technique outlined in Appendix (B). This technique maximises the stark shift of the n=1 to n=2 (1e to 2e) electronic transition, under the application of an external electric field, by altering the QW 'shape'. Once the structure has been optimised for a particular value of the electric field, the quantum confined stark shift can be evaluated using the expression

$$\Delta E_{shift} = (e_2^F - e_1^F) - (e_2 - e_1). \tag{5.1}$$

Where e_2^F, e_1^F, e_2 and e_1 are first excited state electron and ground state electron one particle energies, with and without the electric field.

The above analysis optimises the stark shift (1e-2e transition) in a QW, for a particular electric field. However for a tunable photodetector, the range of electric field involved is of foremost importance. Thus if the field range is from 20kV/cm to 90kV/cm, what we need to know is the structure that gives the maximum energy shift between these fields. For example, one could design a structure whose transition energy, relative to that of a RQW is blue shifted at 90kV/cm but red shifted at 20kV/cm. Utilising our optimisation technique (see Appendix (B)) it is possible, starting from a RQW system, to optimise the blue shift at 90kV/cm. This would yield a particular QW structure. Alternatively we could optimise the red shift at 20kV/cm. This would produce a different structure, thus giving two independent structures. To solve the problem stated, a simultaneous optimisation of energy shifts is made in such a manner that the energy difference between them is maximised. Such an optimisation procedure is described in Appendix (B). Using this technique, it is possible to produce a unique QW structure whose energy shift is maximised for a particular electric field range.

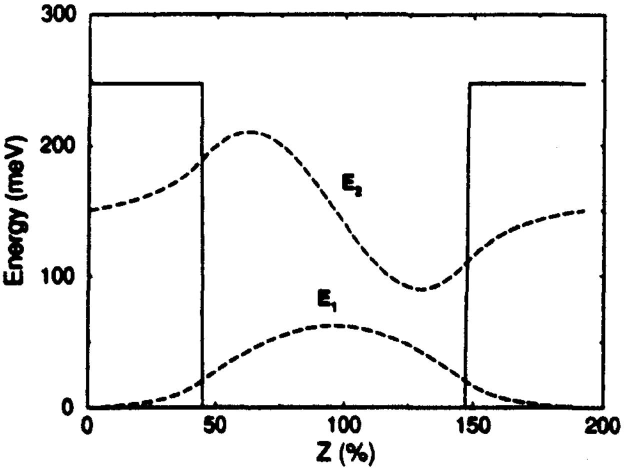

Figure 5.1: Potential profile and n=1, n=2 envelope wavefunctions for a 103Å GaAs RQW, with $Al_{0.33}Ga_{0.67}As$ outer barriers.

5.3 Results

We will illustrate the procedure by considering particular examples. The first system considered comprises a 103Å GaAs well with $Al_{0.33}Ga_{0.67}As$ barrier regions (the reasons for making this choice will become clear later). The energy band structure and the n=1, n=2 envelope wavefunctions for this simple (i.e undoped) RQW are shown in Fig (5.1). On application of a 90kV/cm electric field the wavefunctions are skewed, as shown in Fig (5.2). In order to be a device possibility, the quantum confined stark shift for the n=1 to n=2 electronic transition must be large. However for a RQW, this shift is negligible (~4meV) and thus a simple RQW (even if doped) is of no value for device applications.

The RQW described above was optimised, using the technique described in Appendix (B), so that for an applied electric field of 90kV/cm the blue shift of the 1e-2e intersubband transition was maximised. The optimised structure is shown in Fig (5.3), where it can be seen that the resulting structure is asymmetric and double QW like. This structure gives a blue shift of the 1e-2e transition energy of 63.9 meV when the field is varied from 0kV/cm to 90kV/cm. This same structure gives a 49 meV blue shift for a field range of 20kV/cm to 90kV/cm (a value which will be used later for comparison purposes). Thus by optimising the blue shift of the electronic transition, we have designed a structure which has an 'overall' QW width of 103 Å, i.e the same width as the original RQW, but which has an increased stark shift of almost 60 meV compared with a RQW in the field range 0kV/cm to 90kV/cm. Such a structure, is much more favourable for achieving a tunable photodetector than the original RQW.

The necessity for a large stark shift in structures to be used as tunable photodetectors, has led many researchers to design more elaborate QW's. One such system (which will be used for reference purposes) is that described by Huang et al [13]. These authors considered two structures (see below) but found that the largest stark shifts occurred in a 'high-low coupled quantum well' (HLCQW) which had a tuning range from 7.8 to 10.5μm (i.e an energy shift of 33.8 meV). The HLCQW system comprises two QW's of differing depths. One of these wells is uniformly doped and has a width of 52Å, whilst the other has a width of 21Å. A 30Å $Al_{0.33}Ga_{0.67}As$ inner barrier separates the two wells, with $Al_{0.33}Ga_{0.67}As$ acting as the outer buffer layers (thus the structure has an 'effective' internal width of 103Å between it's outer barriers). By varying the applied electric field between 20kV/cm and 90kV/cm. Huang et al were able to detect a wavelength change of 2.7μm.

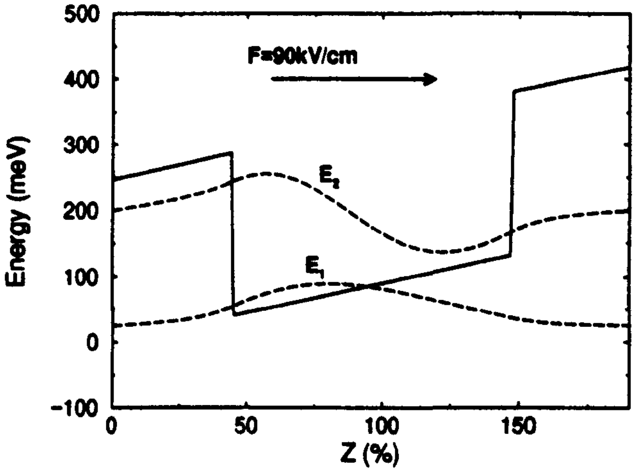

Figure 5.2: Potential profile and n=1, n=2 envelope wavefunctions for a 103Å GaAs RQW, with $Al_{0.33}Ga_{0.67}As$ outer barriers, when an external electric field of 90kV/cm is applied.

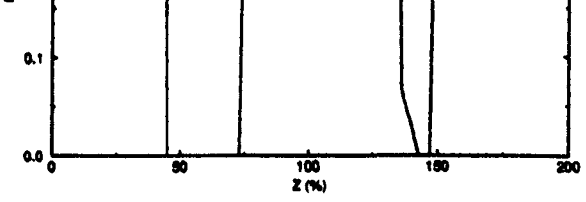

Figure 5.3: Potential profile of an optimised QW structure, optimised for a maximum blue shift of the 1e-2e transition at 90kV/cm.

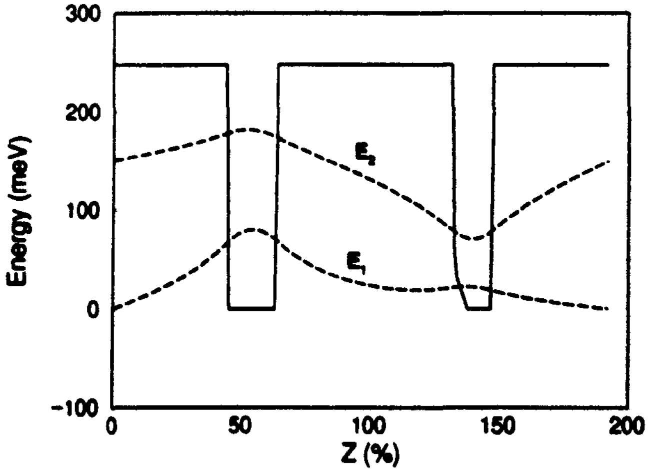

Figure 5.4: Potential profile and n=1, n=2 envelope wavefunctions for an OQW structure (comprising of an 18Å GaAs QW, a 68Å $Al_{0.33}Ga_{0.67}As$ inner barrier followed by a second QW which has a 6Å graded left interface (x=8% to x=0%) and 11Å GaAs), with with $Al_{0.33}Ga_{0.67}As$ outer barriers.

Since the two structures considered by Huang et al, namely the HLCQW and the ACQW (see below) both had an inner region of 103Å, the optimisation procedure for the electric field range 20kV/cm to 90kV/cm was applied to a 103Å GaAs RQW with $Al_{0.33}Ga_{0.67}As$ outer barriers, see Fig (5.1) (and also Appendix (B). Prior to doing this we note that, if we ignore temporarily, the doping of the 52Å well, then our calculations show that the resulting tuning range for the original HLCQW structure of Huang et al is 8 to 10.3μm. This is very close to the values observed by these authors [13] and arises, in essence (as shown by the self-consistent calculations described later), from a partial cancellation of the coulombic potential of the electrons with that arising from the ionised donors in the doped structure. Similar agreement is found for the simple doped ACQW considered by Huang et al where both wells have the same depth. Here, we calculate a tuning range of 8.3 to 10.8 μm for the undoped structure, which is to be compared with the energy range of 8.2 to 11.3μm observed by Huang et al for this same doped structure. Hence in what follows, we will, initially, present results and energy diagrams appropriate to the undoped structure, since this enables the difference between the latter and the optimised QW (OQW) structures described later, to be seen more clearly.

Starting from a 103Å RQW, the results of our calculation for the optimised (undoped) structure, appropriate to a field range of 20 to 90kV/cm, is shown, in the absence of an external electric field, in Fig (5.4) which also displays the ground and first excited state wavefunctions. It can be seen that the resultant structure is double quantum-well like and comprises an 18Å GaAs QW, a 68Å $Al_{0.33}Ga_{0.67}As$ inner barrier followed by a second QW which has a 6Å graded interface on the left (x=8% to x=0%) followed by an 11Å GaAs region together with $Al_{0.33}Ga_{0.67}As$ outer barriers. As is clear from Fig (5.4), at zero field the ground state electron (n=1) spends much more time in the left hand well than it does in the right hand well. The main effect of increasing the field (as can be seen in Fig (5.5)) is to delocalise the ground state electron from the region of the second well.

The optimised structure is very similar to the one shown in Fig (5.3), resulting from optimising the blue shift only, at 90kV/cm. An interesting result is shown in Fig (5.6), which shows the stark shift of the 1e-2e transition at both 20kV/cm and 90kV/cm whilst optimisation is occurring. It can be seen that to optimise the energy range and consequently the tunability between 20kV/cm and 90kV/cm, the stark shift at both fields has an overall

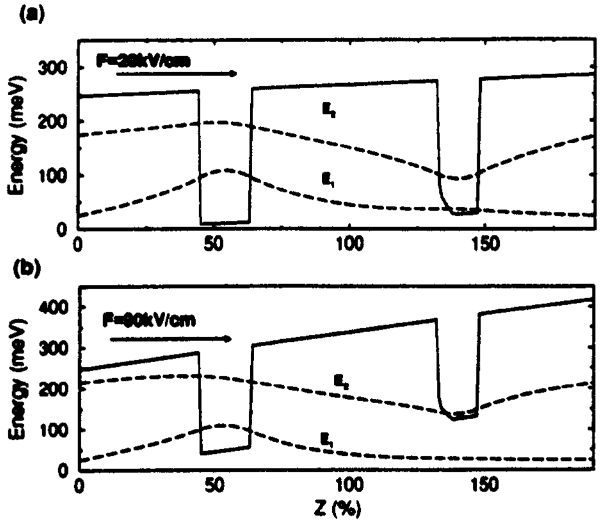

Figure 5.5: Potential profile and n=1, n=2 envelope wavefunctions for an OQW structure (same composition as in Fig (5.4), with (a) a 20kV/cm electric field applied, (b) a 90kV/cm electric field applied.

blue shift. The values of the subband energy difference ΔE_{21} between the two subbands as a function of the applied electric field, are shown in Fig (5.7).

It can be seen that the OQW for the field range under consideration exhibits a stark shift of 53.1 meV which is significantly larger than the 33.8 meV shift of the original structure, considered by Huang et al [13]. It is also grater than the 49 meV stark shift of the structure which was optimised for an electric field of 90kV/cm only. This illustrates clearly that in order to obtain a truly optimised energy range, for two given fields, requires the use of the combined optimisation technique described in Appendix (B).

Another consideration, of perhaps equal importance for the device engineer, is the change in oscillator strength for varying electric fields. As described earlier, this means evaluating the entity $|M_{12}|^2$ for a range of electric fields. Fig (5.8) shows the change in $|M_{12}|^2$ for various electric fields for the simple RQW system. It can be seen that (in arbitrary units) there is an increase in $|M_{12}|^2$ from 42.5 to 44.3 as the electric field is increased. This shows that for the RQW there is little variation with the field in the oscillator strength. As opposed to this, we calculate that for the ACQW structure of Huang et al. $|M_{12}|^2$ varies from 18.5 to 39.5 where as for the HLCQW structure it varies from 20.8 to 46.1. For the OQW structure as can be seen in Fig (5.9), $|M_{12}|^2$ varies (in the same arbitrary units as before) from 5 to 9.5. Clearly the magnitude of $|M_{12}|^2$ is much smaller for the OQW than e.g., for the RQW. This reduction in the magnitude of $|M_{12}|^2$ for the OQW occurs because the optimisation process was directed at maximising the range of tunability of the energy and took no account of the magnitude of the oscillator strength. It is interesting to note in passing that optimisation of the tunable energy range leads to a reduction in the magnitude of the oscillator strength, whereas for the RQW the oscillator strength is large but the tunability of the energy range is negligible. This indicates clearly that intermediate structures must be possible in which the energy range is reduced but the oscillator strength increased significantly. One such (undoped) structure is the one corresponding to a maximisation of the blue shift at 90kV/cm, (see Fig (5.3)). This structure is similar to that of the OQW and comprises a 28Å GaAs QW, a 63Å $Al_{0.33}Ga_{0.67}As$ inner barrier, followed by a 7Å graded interface on the left (x=9% to x=0%) after which there is 5Å layer of GaAs, together with $Al_{0.33}Ga_{0.67}As$ outer barriers (again giving an equivalent internal width of 103Å between the two outer barriers). As noted earlier, application of an electric field in the 20kV/cm to 90kV/cm range leads to an energy separation change of 49 meV, equivalent to a tuning range from 8.6μm to

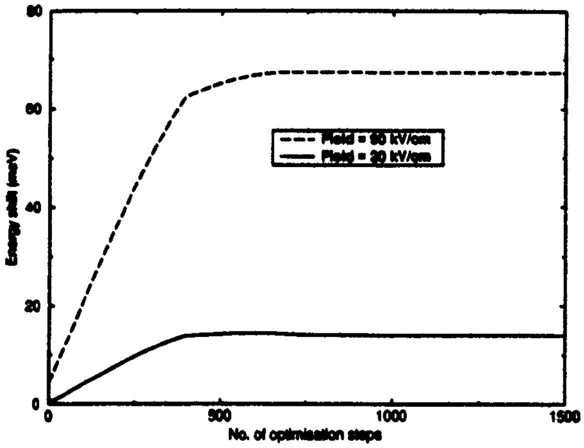

Figure 5.6: The stark shift of the n=1 to n=2 electronic transition at both 20kV/cm and 90kV/cm while optimisation is occurring.

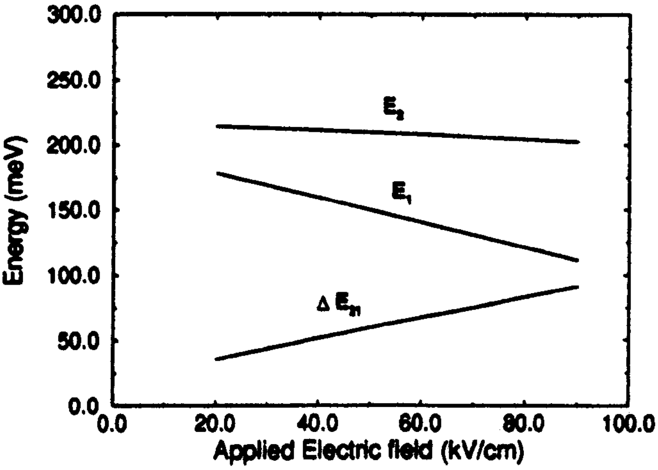

Figure 5.7: Relation of the subband energies and the difference of these subband energies as a function of the applied field for the OQW.

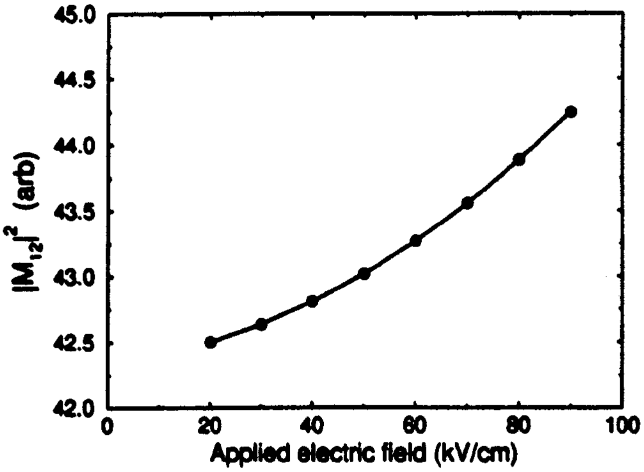

Figure 5.8: Square of the dipole matrix element M_{12} for various applied electric fields, for a RQW.

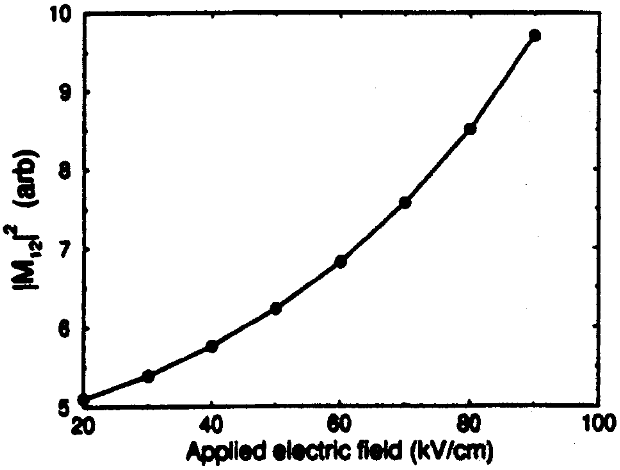

Figure 5.9: Square of the dipole matrix element M_{12} for various applied electric fields, for the OQW.

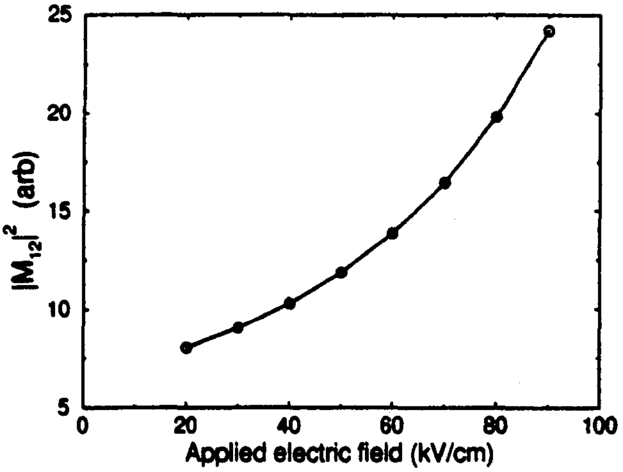

Figure 5.10: Square of the dipole matrix element M_{12} for various applied electric fields, for the intermediate structure.

13μm. Although the energy range is not the maximum possible, it is significantly close to it. Furthermore the oscillator strength is much larger for this system. As shown in Fig (5.10), $|M_{12}|^2$ for the intermediate structure, varies from 8 to 24 for fields ranging from 20kV/cm to 90kV/cm. This is a large increase in both the contrast ratio and the magnitude of the oscillator strength compared with the OQW.

From these discussions it is clear that one can choose an optimisation procedure for the QCSE, appropriate to two particular electric fields, thus producing a structure for which the range of tunability of a photodetector is maximised. However it has been shown also that by adopting a compromise structure, e.g a structure which has been optimised at one field, say 90kV/cm only, we can have a system which has both a larger oscillator strength, a much higher contrast ratio and a tunability energy range which is close to the maximum possible.

5.3.1 Doping effects

We will consider next the effect of doping. The only difference for this situation is that we need to include the potential from the ionized donors together with the coulomb and exchange terms arising from the electrons. Methods of dealing with this are straightforward in principle and are described in the literature [1]. They differ only in the way they treat the exchange term see e.g, [13, 24]. We have utilized both of the techniques referred to in [13, 24] and find, for the structures, of interest, that the energy shifts in the field given by either method differ by at most 2 or 3 meV. These same calculations show also that there is a partial cancellation of the coulombic term of the donors with that of the electrons. Basically the effect of doping the structure is marginal, as far as energy shifts in the field are concerned. Because of the uncertainties in the theory, as regards self-consistently evaluating the exchange term, our calculations suggest that the energy shift given by calculations based on the undoped structure are correct to within typically 2 or 3 meV. As a result the discussion and conclusions given above remain essentially unchanged when the structure is doped.

---

[1] A more detailed description of the self-consistent solutions relating to the effects of doping are described in chapter 1.

5.4 Conclusion

We have utilized an optimisation procedure which maximises the tunability of the energy range for the n=1 to n=2 electron transition in a given external electric field range. In order to illustrate the procedure, we have considered the structures described by Huang et al [13]. The results of the optimisation routine for this particular case produce a QW structure which is ACQW like and gives rise to an energy range of 53.1 meV, which is to be compared with the maximum energy range of 33.8 meV obtained by Huang et al [13]. We have shown that an intermediate structure can also be chosen, which gives a significantly larger value for the oscillator strength, has a much higher contrast ratio and maintains almost the same tunability in the energy range. The results serve to indicate that implementation of these optimised structures in photodetectors can result in excellent tunability, high oscillator strengths and large contrast ratios. Such features are clearly of value to the device engineer and suggest that the corresponding optimised structures could be usefully incorporated into infra-red photodetectors.

Bibliography

[1] H.Q. Le, J.J. Zayhowski and W.D. Goodhue, Appl.Phys.Lett.**50**,1518 (1987).

[2] T. Hiroshima and K. Nishi, J.Appl.Phys,**62**,3360 (1987).

[3] K.Nishi and T. Hiroshima, Appl.Phys.Lett.**51**,320 (1987).

[4] T. Ishikawa and K. Tada, Jpn.J.Appl.Phys.bf 28,L1982 (1989).

[5] D.A.B. Miller, D.S. Chemla, T.C. Damen, A.C. Gossard, W. Wiegmann, T.H. Wood and C.A. Burns, Phys.Rev.B, **32**,1043 (1985).

[6] M. Morita, K. Goto and T. Suzuki, Jpn.J.Appl.Phys.**29**,L1663 (1990).

[7] W. Chen and T.G. Andersson, Semicond.Sci.Technol.**7**,828 (1992).

[8] H. Iwamura, T. Saku and H. Okamoto, Jpn.J.Appl.Phys.**24**,1 04 (1985).

[9] K. Wakita, Y. Kawamura, Y. Yoshikuni and H. Asahi, Electron.Let t.**21**,338 (1985).

[10] D.A.B. Miller, D.S Chemla, T.C. Damen, A.C. Gossard, W. Weigma nn, T.H. Wood and C.A. Burrus, Appl.Phys.Lett. **45**,13 (1984).

[11] T.H. Wood, C.A. Burrus, A.H. Guanck, J.M. Wiesenfeld, D.A.B. Miller, D.S. Chemla and T.C. Damen, Appl.Phys.Lett. **47**,190 (1985).

[12] L.C. West and S.J. Eglash, Appl.Phys.Lett. **46**,1156 (1985).

[13] Y. Huang, C. Lien and T. Lei, J.Appl.Phys. **74**,2598 (1993).

[14] Y. Huang and C. Lien, J.Appl.Phys. **76**,3181 (1994).

[15] Y. Huang and C. Lien, J.Appl.Phys. **77**,3433 (1994).

[16] C. Sirtori, J. Faist, F. Capasso, D.L. Sivco and A.Y. Cho, Appl.Phys.Lett. **62**,1931 (1993).

[17] K.W. Goossen, J.E. Cunningham and W.Y.Jan, Appl.Phys.Lett. **64**,1071 (1994).

[18] F. Capasso, C. Sirtori, and A.Y. Cho, IEEE.J.Quantum.Electron. **QE-30**,1313 (1994).

[19] C. Sirtori, F. Capasso, D.L. Sivco, A.L. Hutchinson and A.Y. Cho, Appl.Phys.Lett. **60**,151 (1992).

[20] A. Harwit and J.S. Harris, Jr., Appl.Phys.Lett. **50**, 685 (1987).

[21] Y.H. Wang and S.S. Li, Appl.Phys.Lett. **62**,621 (1993).

[22] J.P. Killingbeck, "Microcomputer Algorithms", (Hilger,Bristol,1992).

[23] G.Bastard, "Wave mechanics applied to semiconductor heterostructures", (Halsted Press,New York,1988).

[24] P. Ruden and H. Dohler, Phys.Rev.B, **27**,3538 (1983).

Chapter 6

Optimisation of blue shifts in δ doped *nipi* structures

6.1 Introduction

Doped superlattices were first proposed by Esaki and Tsu [1] in 1970. In these proposals the idea of producing periodic potentials by means of ionised impurities was discussed. The doping superlattice consists of alternating, homogeneously doped n- and p-type regions within a host semiconductor. The fundamental idea behind such structures was the enhancement of non linear optical effects thus providing opportunities for novel semiconductor devices. These devices would be based on properties unique to doped superlattices, e.g, reduced energy gap of the superlattice compared with the (undoped) host semiconductor; enhanced carrier lifetime for radiative recombination and the tunability of the energy gap via an external excitation [2]. Although, in principle, doping superlattices can give rise to many new effects, it was found that growing such *npn* or *nipi* structures suffered serious limitations, e.g such structures did not lead to the observation of quantum confined interband transitions. With the development of technology and the introduction of molecular beam epitaxy (MBE), it has become possible to grow more precise semiconductors structures. In particular, it has been possible to grow δ doped superlattices. A δ doped superlattice is similar to the original proposal made by Esaki and Tsu for the doped superlattices. The difference lies in the fact that the entire dopant region is confined to a single or few monolayers of the semiconductor lattice [1]. This leads to several important advantages over the homogeneously doped structures, e.g large superlattice modulation, feasibility of shorter periods and minimisation of potential fluctuations [3].

The δ doped structure consists of alternating n and p type δ doped sheets separated by intrinsic (undoped) layers. This leads to periodic *nipi* structures which have linear internal fields between the n and p doped layers (i.e, in the intrinsic regions), as opposed to a parabolic band structure found in the homogeneously doped structures. This is illustrated in Fig (6.1), which shows the band structure for both the original *npn* semiconductor superlattices and the newly developed δ doped *nipi* structures [2].

Since in δ doped structures the dopants are confined within regions of space which are small compared with the spatial extent of the ground state wavefunction of the electrons, the dopants can be dealt with as sheets of charge. For such structures, it is found that carriers are confined in the 'V' shaped potentials induced in the intrinsic region, rather than in the parabolic potential in the region of the dopants themselves (as in the original *npn*

---

[1] Since the dopants are only distributed over a few monolayers, they are said to resemble a Dirac delta function, hence the name δ doped.

[2] Also referred to as 'sawtooth' superlattices.

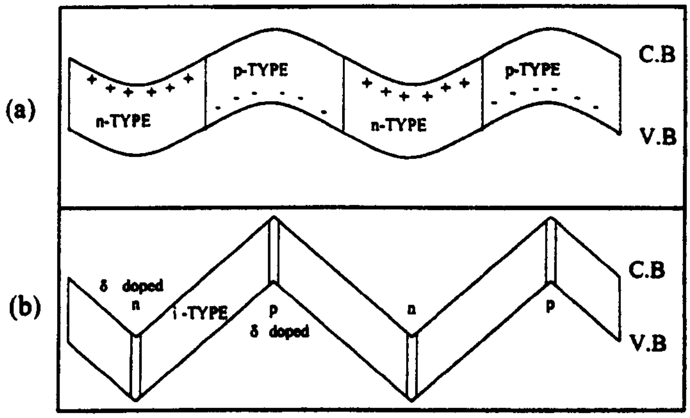

Figure 6.1: Band diagram for (a) homogeneously doped *npn* superlattice, and (b) δ doped superlattice.

structures) [4]. It was found that δ doped superlattices showed a significant improvement in their optical properties [5, 6, 7].

Since the periodicity in doping superlattices is exclusively space charge induced, they differ from compositional superlattices. In particular the 'sawtooth' type band structure of a doped superlattice has the valence and conduction band modulated in parallel, as shown in Fig (6.2a). As opposed to this a graded gap change in a compositional superlattice would have the valence and conduction band modulated in opposite directions. Consequently indirect band gap transitions occur in the doped structure (type II) as opposed to direct band gap transitions in the compositional structure (type I).

The features outlined earlier give rise to interesting, new physics as well as being useful fron the device point of view. In the present chapter the main area of interest is the large stark shifts that occur in the transition energies, when δ doped *nipi* structures are optically pumped [8, 9].

In particular, the problem to be addressed is the following. For a given excitation source, what is the best spacing and doping level of the n and p regions in order that the stark shift in the interband transition energy is maximised.

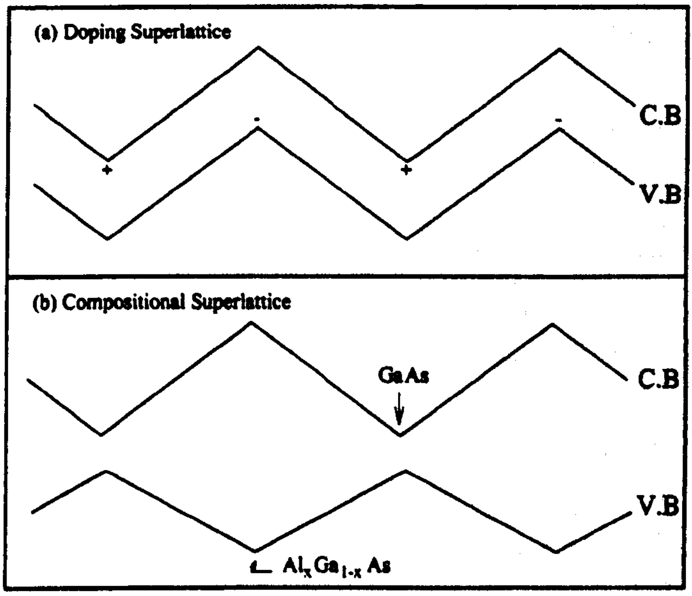

Figure 6.2: Band diagram for (a) δ doped 'sawtooth' superlattice, and (b) a compositional 'sawtooth' superlattice.

6.2 Theory

The system consists of a compensated δ doped *nipi* structure, which means that all the carriers present are induced via optical excitation [3] . Thus as the electrons and holes recombine the band structure of the lattice is continually changing. For a particular carrier density N the band structure can be determined by the self consistent solution to both the Poisson equation and the one-particle Schrödinger equation (a full analysis is given in Chapter 2). For the excited carrier densities considered below, it is found that many body effects are negligible in comparison with the coulombic interaction. Thus as a first approximation the exchange and correlation term can be neglected (clearly the method can be extended in a straightforward manner to include exchange and correlation terms).

Optimisation of a δ doped *nipi* structure can be attained by using the optimisation routine described in Appendix A. However unlike Appendix A, there is no external electric field applied to the structure. Consequently the optimisation routine invlolves an optically excited *nipi* structure with N free charge carriers and an unperturbed structure with no free charge carriers. In this manner a direct correspondence can be made between the δ doped *nipi* structure with no free carriers, and the QW system without an external field, and between the self consistent δ doped *nipi* structure with N free charge carriers and the QW system with an external field.

To maximise the Stark shift, we must employ an iterative technique, as discussed above. The flow chart (Fig (6.3)), shows the computational steps involved in optimising the Stark shift. Starting from a δ doped *nipi* structure, the 'shape' of the potential can be optimised, so that the maximum Stark shift can be attained for N optically excited charge carriers.

Once an optimised structure is obtained, the one particle Schrödinger equation for this structure is then solved exactly with the inclusion of excitonic effects (see Chapter 1) [10].

Another important consideration for device applications is the recombination time for the N optically excited charge carriers. This can be found by solving numerically the equation:

$$\frac{\partial N}{\partial t} = -\alpha(N)N(t), \tag{6.1}$$

where $\alpha(N)$ the transition probability [4] is dependent on N. To evaluate the emission intensity as a function of time, the transition probability and the density of carriers with respect to time must be known. Once these quantities have been calculated the emission intensity can be found to be,

$$I \propto \alpha(N)N(t). \tag{6.2}$$

It can be seen that by use of these techniques, the evolution of the optical properties of a system can be determined. Thus for any arbitrary potential the recombination, emission intensity and interband transition energies can be determined as functions of time.

---

[3] A non-compensated *nipi* structure could be dealt with readily by the following technique as will become apparent.

[4] In the calculations presented $\alpha(N)$ at any instant in time is assumed to be the same for all carriers and is taken to be proportional to the square of the overlap integral of the electron and hole suitably modified to allow for excitonic effects. Consequently we can write

$$\alpha(N) = \frac{\alpha(N)}{\alpha(0)}.\alpha(0) = \frac{I(N)}{I(0)}.\frac{1}{\tau_0}$$

where τ_0 is the experimentally observed decay time for very weak excitation, $I(N)$ is the square of the overlap integral appropriate to N carriers present, and $I(0)$ that of a single electron-hole pair.

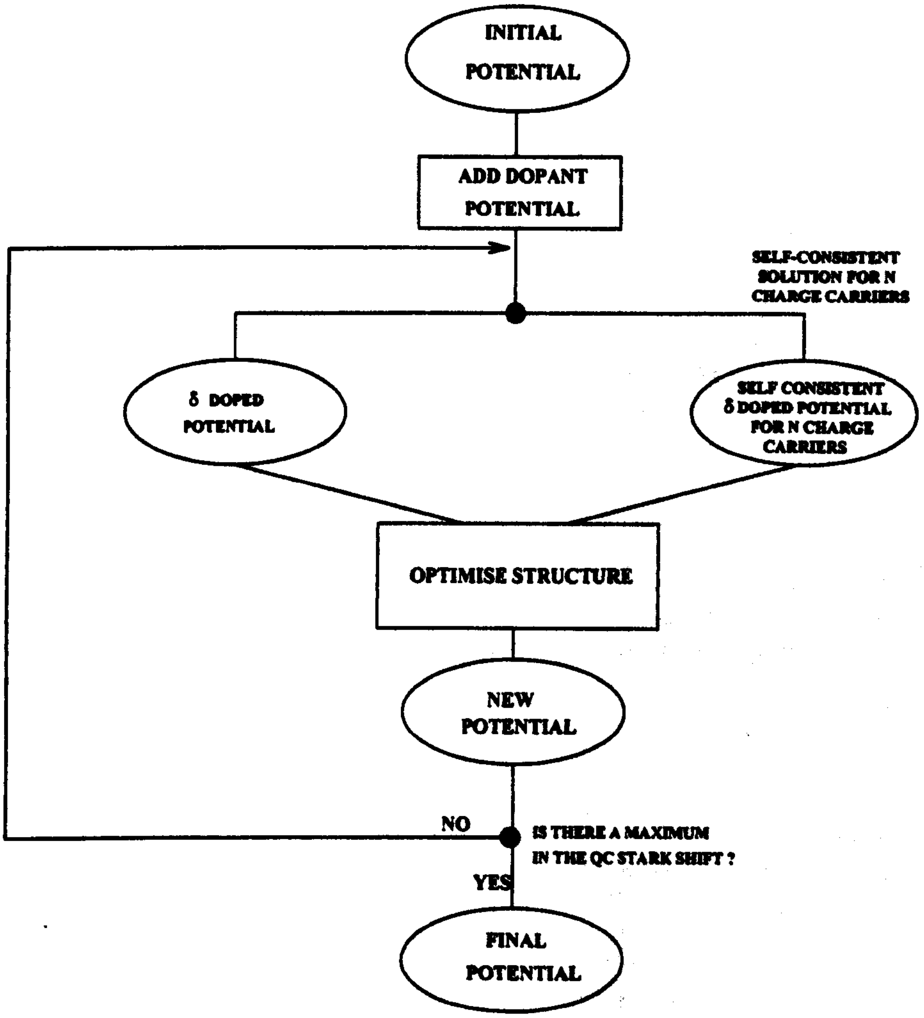

Figure 6.3: Flow chart showing the computational steps involved in optimising the potential 'shape' of a δ doped *nipi* structure, so as to maximise the Stark shift.

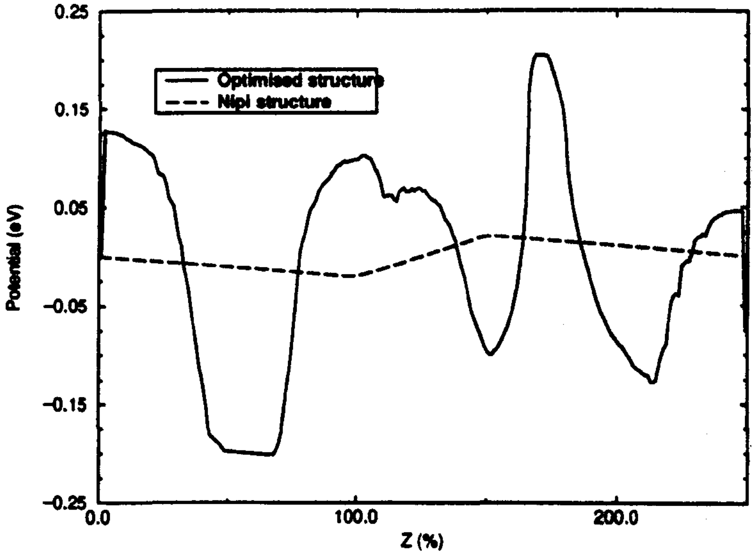

Figure 6.4: Conduction band diagram of optimised structure (solid line); optimised from a δ doped *nipi* structure (dashed line), where the $5\text{x}10^{23}/\text{m}^3$ dopants are placed 50Å apart; optimised to maximise the blue shift for $5\text{x}10^{14}/\text{m}^2$ excited charge carriers.

6.3 Results

The system considered is CdTe. This system has been well researched for use as a compound semiconductor with Mn as the ternary alloy [11, 12]. We consider the CdTe system not as a compound semiconductor, but as a host semiconductor where n and p type δ doped regions can be grown (via MBE) into the crystal lattice. Thus in the following results the system reported is a doped CdTe lattice structure. The choice of semiconductor is arbitrary and purely illustrative of the technique which can be applied to any bulk semiconductor.

A δ doped *nipi* structure was initially considered. The system consisted of a 10Å doped region (dopant density $5\text{x}10^{23}/\text{m}^3$) placed 50Å from a 10Å p doped region of equal density. Starting from this structure the system was optimised for the situation where $5\text{x}10^{14}/\text{m}^2$ optically excited charge carriers were present in it. Such a density of charge carriers blue shifts the energy separation of the elctron and hole by ~17meV on being excited optically in the original *nipi* structure. On optimising the structure the blue shift is enhanced by more than three times it's original value to 55.1meV. The structure corresponding to this enhanced blue shift is shown in Fig (6.4). It is immediately apparent from the figure that the optimised structure has a considerably different potential profile from that of the original *nipi* structure. The profile is 'treble well like' for electrons and 'double well like' for holes. In effect the potential has two deep potential wells, one confining the electron (the left most well) and the other confining the heavy hole (the right well). It is also noticeable that the positions of the potential wells formed by optimisation, are not spatially equivalent to the 'V' shaped potential wells of the original structure. The potential wells formed during optimisation are much deeper than the original potential wells, they are also placed further apart than the original 'V' shaped wells of the *nipi* structure. The purpose of these wells is to confine the electron and hole separately, such that there is little overlap between the envelope wavefunctions before and after optical excitation of the charge carriers. From Fig (6.5) it can be seen that there is no movement of the wavefunctions after excitation, and that the blue shift in the one particle energy separation is due purely to a change in the effective

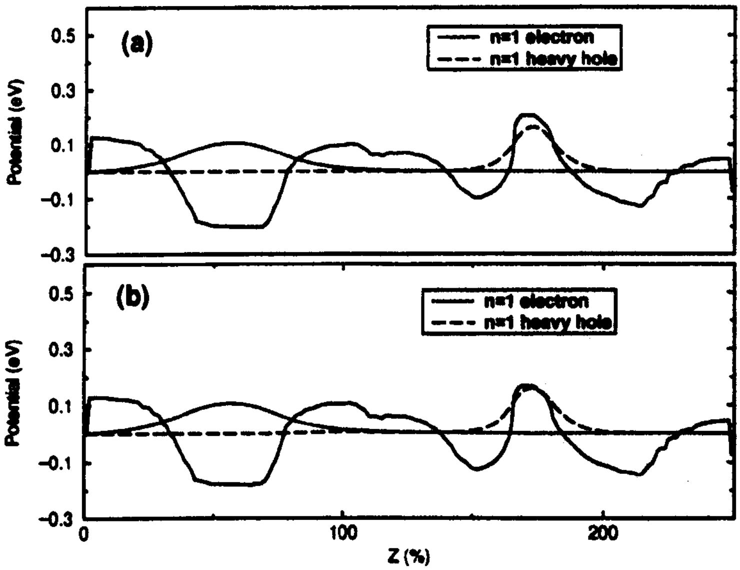

Figure 6.5: Conduction band diagram of optimised structure; optimised from a δ doped *nipi* structure, where the $5x10^{23}/m^3$ dopants are placed 50Å apart; optimised to maximise the blue shift for $5x10^{14}/m^2$ excited charge carriers,(a) no charge carriers, and (b) $5x10^{14}/m^2$ charge carriers.

band gap of the semiconductor[5]. The effective confining potential well for the electron is wider than the one which effectively confines the heavy hole. This can be explained by consideration of the relative effective masses of the two types of carriers. Since the effective mass of the electron is less than of the heavy hole, the resultant envelope wavefunction is more extensive than that of the hole, hence needing a wider well to confine it.

As a check on the optimisation procedure two more structures were optimised. Both of these structures had the same dopant densities as previously defined, and were assumed to have the same number of optically excited charge carriers. However for these structures the dopants were placed at differing distances apart, such that the distance between the n and p regions of the original *nipi* structures were 100Å and 150Å. It was found that in both cases the optimisation procedure led to virtually identical structures to that of the 50Å separation case, with the blue shifts being enhanced in both structures to ~55meV (see Fig (6.6). This shows that the optimised profile is independent of the starting profile and is dependent mainly on the number of optically excited charge carriers. Since, as a first approximation, the exchange and correlation effects have been neglected, the density of charge carriers to be considered must be relatively low. Physical intuition tells that as we increase the density of charge carriers, i.e increase the excitation intensity, the effective band gap of the semiconductor is increased and thus the blue shift enhanced. This has been verified experimentally by Bastola et al [8], who reported a logarithmic dependence between the optical blue shift and the excitation intensity.

The next system to be considered was a δ doped *nipi* structure with the same dopant density as before, i.e $5x10^{23}/m^3$. This structure was optimised at lower excitation intensities, where it was assumed that the number of free charge carriers was $1x10^{14}/m^2$. Fig (6.7) shows the optimised potential profile with no charge carriers present. It can be seen that the potential profile of the optimised structure is similar to that of the previous system. The

---

[5] At present we have dealt with one particle energy separations, however if the effect of the exciton binding energy is also included, it is found that the energy shift is unaffected, this being due to the lack of movement in the electron and hole, before and after excitation.

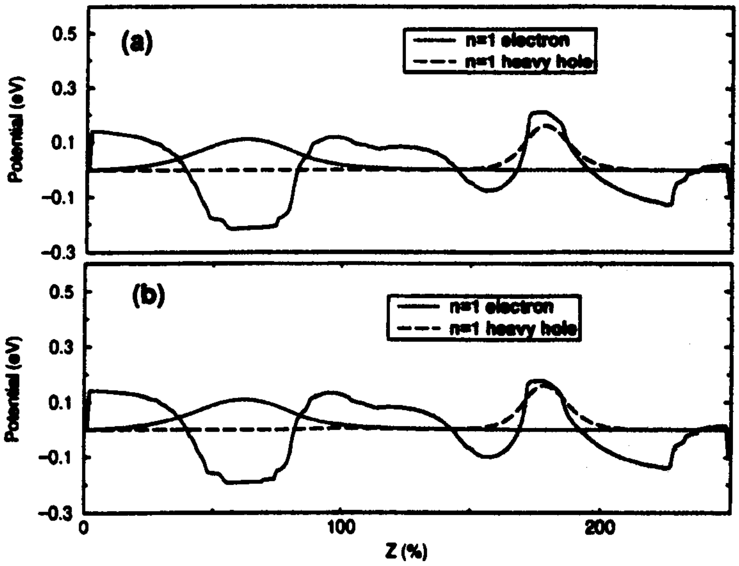

Figure 6.6: Conduction band diagram of optimised structure; optimised from a δ doped *nipi* structure, where the $5\text{x}10^{23}/\text{m}^3$ dopants are placed (a)100Å apart, (b)150Å apart; optimised to maximise the blue shift for $5\text{x}10^{14}/\text{m}^2$ excited charge carriers.

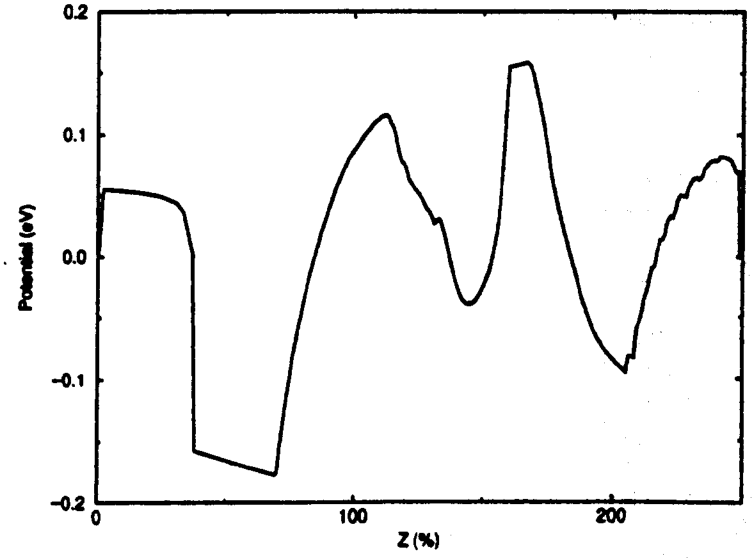

Figure 6.7: Conduction band diagram of optimised structure; optimised from a δ doped *nipi* structure, with doping density $5\text{x}10^{23}/\text{m}^3$. Optimised for $1\text{x}10^{14}/\text{m}^2$ excited charge carriers.

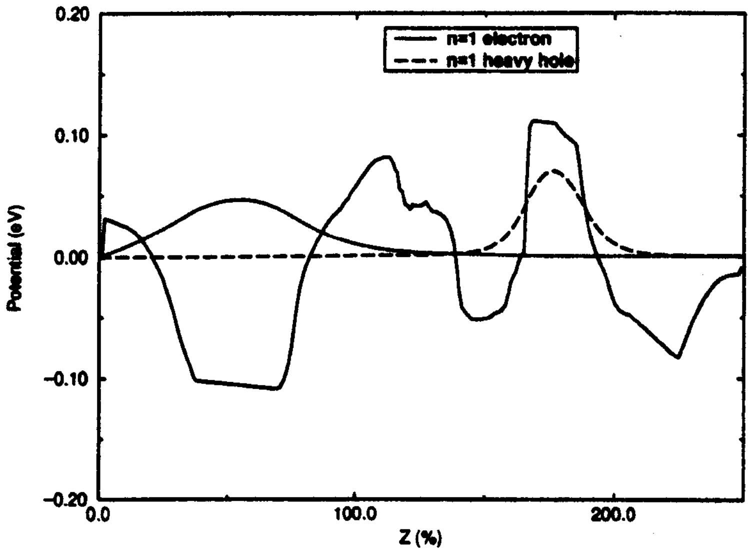

Figure 6.8: Conduction band diagram of optimised structure; optimised from a δ doped *nipi* structure, with doping density $5x10^{23}/m^3$. Optimised for $1x10^{13}/m^2$ excited charge carriers.

structure adjusts itself so as to confine the electron and heavy hole in separate potential wells, having a similar distance of separation as found previously. For this situation the overlap of the envelope functions of the electron and hole is negligible. The one noticeable difference between the present structure, and the earlier one is the depth of the potential wells. The latter for the lower excitation intensity, is less than for the higher intensity. A trend which is true in general. However, the results also suggest that there is an optimum 'shape' of the potential profile, which is independent of the excitation intensity (apart form the well depth) which will maximise the blue shift. The idea of an optimum potential 'shape' which maximises the blue shift can be verified by consideration of different excitation intensities. Fig (6.8) shows the optimised potential profile and carrier wavefunctions, for a carrier density of $1x10^{13}/m^2$. The graph shows that for low densities the optimised potential shape is similar to that of the higher density case. The similarities lie in the formation of two potential wells ~115Å apart, one of which is wider than the other.

The optimised systems described above would be very difficult to grow experimentally. However we note that Merchant [13] has shown that, by using lateral diffusion, any dopant profile can (in theory) be realised. Thus the profiles described are theoretically realisable but would require advanced technology. Unfortunately the technology needed to grow such structures does not exist presently. For this reason it is advantageous to use the information gained through optimisation, to design simple *nipi* structures which can enhance the blue shift (although the latter will always be less than that for the optimised structure). Fig (6.9) shows a *nipi* structure which has been designed to reproduce a similar potential profile to that of the optimised structure. The *nipi* structure shown produces a blue shift of ~48meV when $5x10^{14}/m^2$ charge carriers are excited from the valence band to conduction band. The *nipi* structure consists $3x10^{24}/m^3$ dopants placed at 55Å and 170Å (i.e 115Å apart).

The doping concentration and the separation distance between the p and n layers, has been based upon the optimised structure. Fig (6.10a) shows the blue shift that would be achieved if the separation was varied (within the simple *nipi* structure), but the concentration kept constant. From Fig (6.10a) it can be seen that the maximum blue shift is given when the dopants are placed ~ 115Å apart. Fig (6.10b) shows the blue shift for various

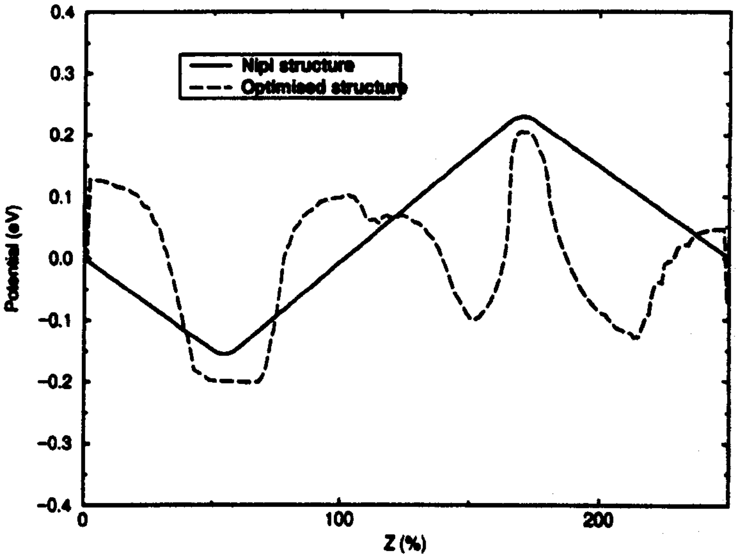

Figure 6.9: Conduction band diagram of optimised structure, optimised for 5x10^{14}/m^2 excited charge carriers, with an equivalent simple δ doped *nipi* structure.

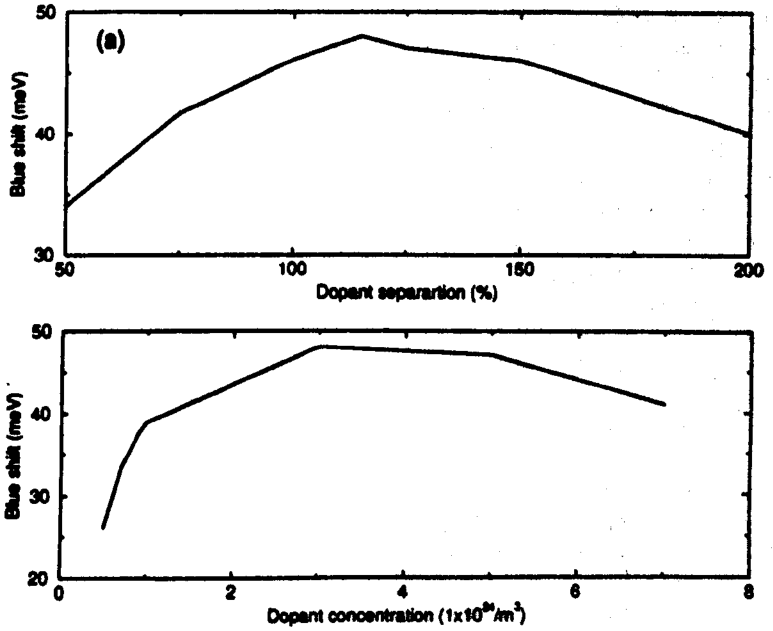

Figure 6.10: (a) Blue shift versus separartion of the dopants layers for a optically excited (5x10^{14}/m^2 charge carriers) *nipi* structure, with dopant concentration 3x10^{24}/m^3;(b) blue shift versus dopant concentration for an optically excited (5x10^{14}/m^2 charge carriers) *nipi* structure, where the dopants are separated by 115Å.

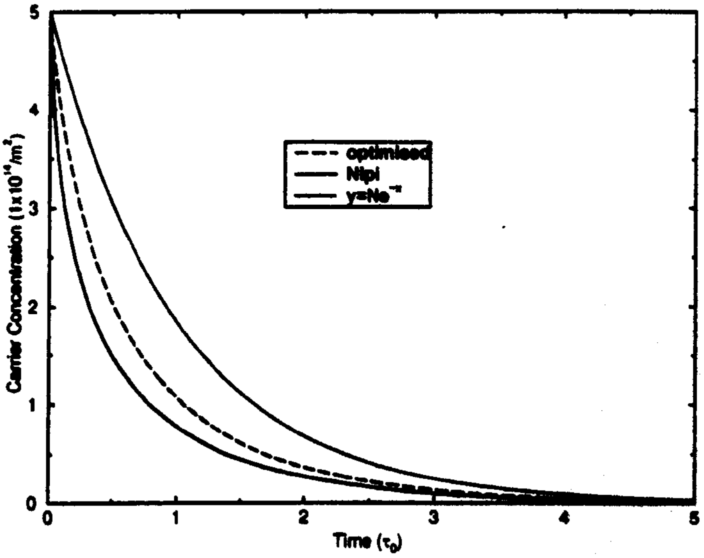

Figure 6.11: Recombination rates for $5\text{x}10^{14}/\text{m}^2$ optically excited charge carriers present in the optimised and nipi structures. The entity τ_0 is the decay time for each structure when excited weakly.

concentartions of dopants (again within the simple *nipi* structure), where the separartion is kept constant; again it can be seen that the maximum blue shift for this structure is given for a concetration of $3\text{x}10^{24}/\text{m}^3$ dopants. Thus through use of the optimised structure a *nipi* structure can be designed which can give information on both the best dopant separation and the best dopant concentration so as to maximise the blue shift.

Another important physical feature, when dealing with δ doped *nipi* structures is the recombination time for the excited charge carriers. This was found by solving equation (6.1). Time is measured in units of τ_0[6]. Fig (6.11) shows the recombination rates for the optimised and *nipi* structures. The curve $y = Ne^{-x}$ is also plotted which represents an exponential decay for a structure whose decay rate is τ_0. It can be seen that in both the optimised structure and the *nipi* structure the decay rate is greater than the exponential decay. Examination of this curve shows that as the electrons recombine with the holes, the self consistent change in the potential produces a non exponential decay. The graph also shows that the *nipi* structure has a lower recombination time than the optimised structure, suggesting that although there is a loss in the value of the blue shift when the *nipi* structure is employed, there is a gain in the recombination rate of such a structure. This increase in recombination rate can be explained by a consideration of the electron and hole transition probability. In the optimised structure the electrons are well separated from the holes, thus leading to a reduced transition probability. In the *nipi* structure, since the electron and hole are less well separated the transition probability is higher.

Fig (6.12) shows the variation of the interband transition energy (i.e the emission paek) as a function of the time. It can be seen that both the optimised and *nipi* structures emission energies change similarly with time. The difference in the magnitude of the enrgy is due simply to the depth of the potential wells. In short, since the optimised structure could not be reproduced precisely using a simple *nipi* structure, the energy of emiision is different for the two strucures. Nonetheless the energy shift, is similar and is very large in both cases.

---

[6] τ_0 is the decay time for a low concentration of excited carriers whose decay can be said to follow an almost exponential rate. This must be determined experimentally for each type of structure.

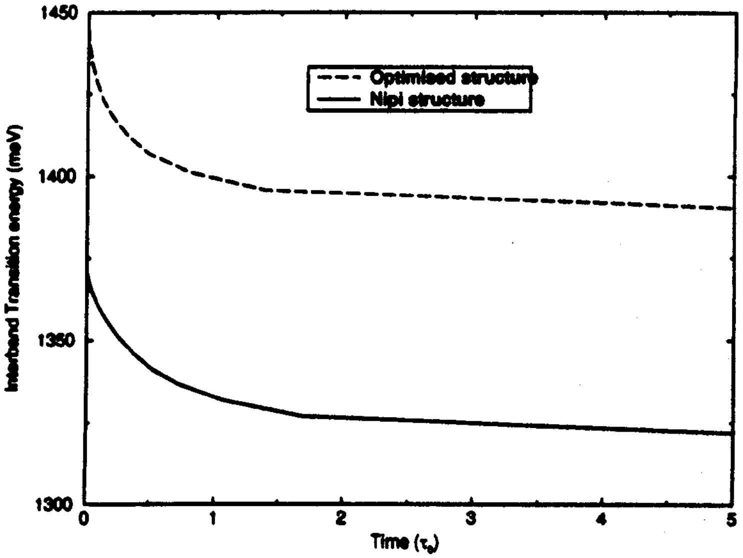

Figure 6.12: Change in interband transition energies as the structure relaxes after $5\text{x}10^{14}/\text{m}^2$ charge carriers are excited into the conduction band.

The emission intensities were also calculated (using equation (6.2)). These are shown in Fig (6.13). As can be seen, both structures have emission intensities which decay rapidly, with the majority of the emitted light being blue shifted. It can also be seen that the emission intensity of the optimised structure is initially greater than that of the *nipi* structure.

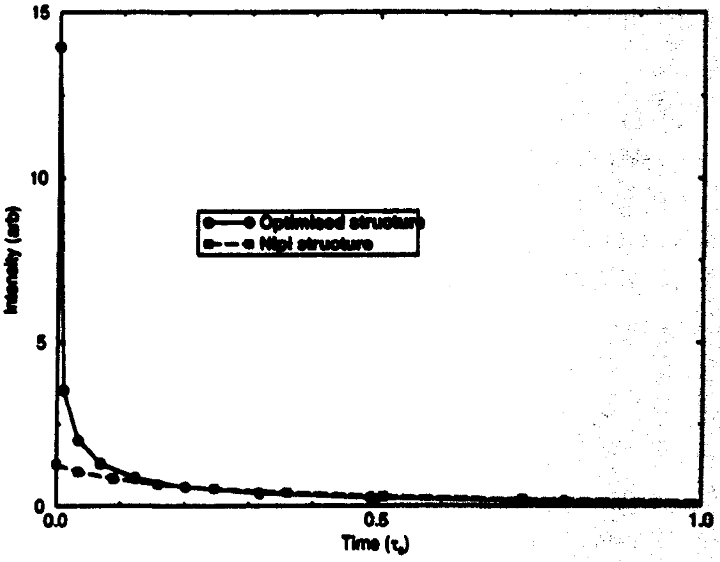

Figure 6.13: Change in intensity as the structure relaxes after 5x10^{14}/m^2 charge carriers are excited into the conduction band.

6.4 Conclusion

The results show that by optimising an arbitrary doped potential profile, it is possible to produce a unique doping induced potential profile which maximises the blue shift of the transition energies for a density N of excited carriers. The optimised structure for a carrier density of $5\text{x}10^{14}/\text{m}^2$ gives blue shifts ~55meV. The results also show that the optimised profile has certain characteristic features some of which are almost independent of the density of excited charge carriers (N). Using such features it is possible to design a simple *nipi* structure which gives large blue shifts close to the optimum. One such structure was presented, whose blue shift was calculated to be ~48meV.

Other features of these structures have also been investigated, and it has been shown that both structures exhibit fast recombination times, essential for device applications. The results show that by use of an optimisation process, it is possible to determine the characteristic features common to all optimised structures. Utilising these same features makes it possible to design simple structures which have blue shifts comparable with those of the optimised ones.

Bibliography

[1] L. Esaki and R. Tsu, IBM J.Res.Dev. **14**,61 (1970).

[2] E. F. Schubert, Opt.Quantum.Electron. **22**,S141 (1990).

[3] E. F. Schubert, T. D. Harris and J. E. Cunningham, Appl.Phys.Lett. **53**,2208 (1988).

[4] E. F. Schubert, J.Vac.Sci.Technol. **A8**,2980 (1990).

[5] E. F. Schubert, Surf.Sci. **288**,240 (1990).

[6] E. F. Schubert, B. Ullrich, T. D. Harris and J. E. Cunningham, ibid. **B38**,8305 (1988).

[7] E. F. Schubert, T. D. Harris, J. E. Cunningham and W. Jan, ibid. **B39**,11011 (1989).

[8] S. Bastola, S. J. Chua and S. J. Xu, J.Appl.Phys. **83**,1476 (1998).

[9] M. B. Johnston, M. Gal, G. Li and C. Jagadish, J.Appl.Phys. **82**, 5748 (1997).

[10] C.P. Hilton, W.E. Hagston and J.E. Nicholls, J.Phys.A. **25**,2395 (1992).

[11] "Semiconductors and Semimetals",edited by R.K.Willardson and A.C.Beer (Academic, Boston, 1988), Vol.25.

[12] J.K. Furdyna, J.Appl.Phys. **64**,R29 (1988).

[13] S. Merchant, IEEE Transactions on Electron Devices. **42**,2226 (1995).

Appendix C

Publications resulting from the work presented in this thesis

Published articles

- R. K. Gug and W. E. Hagston, '*Large blue shifts induced by the quantum confined stark effect in asymmetric quantum wells*', Applied Physics Letters. 73,1547 (1998).
- R. K. Gug and W. E. Hagston, '*Enhancement of the quantum-confined stark effect utilizing asymmetric quantum well structures*', Applied Physics Letters. 74,254 (1999).

Submitted articles

- R. K. Gug and W. E. Hagston, '*Enhanced tunability in infrared photodetectors through optimisation of the quantum-confined stark effect*', Journal of Applied Physics.
- R. K. Gug, R. G. Roberts, T. Stirner, W. E. Hagston, A. A. Davis and P. B. Wells, '*Tuning of surface electric field via a quantum well-like structure for the purpose of controlling catalytic activity*', Journal of Applied Physics.

Future submissions

- R. K. Gug and W. E. Hagston, '*Optimisation of blue shifts in δ doped* nipi *structures*'.
- R. K. Gug, W. E. Hagston, D. Sands and J. D. Hoyland '*Pulsed laser processing of Silicon thin films*'.